

The Calar Alto Legacy Integral Field Area Survey: extended and remastered data release

S.F. Sánchez¹, L. Galbany^{2,3}, C.J. Walcher⁴, R. García-Benito⁵, J.K. Barrera-Ballesteros¹

¹*Instituto de Astronomía, Universidad Nacional Autónoma de México, A. P. 70-264, C.P. 04510, México, D.F., Mexico.*

²*Institute of Space Sciences (ICE, CSIC), Campus UAB, Carrer de Can Magrans, s/n, E-08193 Barcelona, Spain.*

³*Institut d'Estudis Espacials de Catalunya (IEEC), E-08034 Barcelona, Spain.*

⁴*Leibniz-Institut für Astrophysik Potsdam (AIP), An der Sternwarte 16, 14482 Potsdam, Germany.*

⁵*Instituto de Astrofísica de Andalucía (IAA/CSIC), Glorieta de la Astronomía s/n Aptdo. 3004, E-18080 Granada, Spain.*

Accepted XXX. Received YYY; in original form ZZZ

ABSTRACT

This paper describes the extended data release of the Calar Alto Legacy Integral Field Area (CALIFA) survey (eDR). It comprises science-grade quality data for 895 galaxies obtained with the PMAS/PPak instrument at the 3.5 m telescope at the Calar Alto Observatory along the last 12 years, using the V500 setup (3700–7500 Å, 6 Å/FWHM) and the CALIFA observing strategy. It includes galaxies of any morphological type, star-formation stage, a wide range of stellar masses ($\sim 10^7$ – $10^{12} M_{\odot}$), at an average redshift of ~ 0.015 (90% within $0.005 < z < 0.05$). Primarily selected based on the projected size and apparent magnitude, we demonstrate that it can be volume corrected resulting in a statistically limited but representative sample of the population of galaxies in the nearby Universe. All the data were homogeneous re-reduced, introducing a set of modifications to the previous reduction. The most relevant is the development and implementation of a new cube-reconstruction algorithm that provides with an (almost) seeing-limited spatial resolution ($\text{FWHM}_{\text{PSF}} \sim 1.0''$). To illustrate the usability and quality of the data, we extracted two aperture spectra for each galaxy (central $1.5''$ and fully integrated), and analyze them using `pyFIT3D`. We obtain a set of observational and physical properties of both the stellar populations and the ionized gas, that have been compared for the two apertures, exploring their distributions as a function of the stellar masses and morphologies of the galaxies, comparing with recent results in the literature.

Key words: galaxies: evolution – galaxies: ISM – techniques: spectroscopic

1 INTRODUCTION

The exploration of galaxy properties and the understanding of their evolution along cosmological times has been significantly improved in the last few decades by the combination of large cosmological surveys (e.g. York et al. 2000a; Driver et al. 2009), detailed N-body and hydrodynamical simulations (e.g., IllustrisTNG Springel et al. 2018), and in particular by the massive exploitation of novel techniques like integral field spectroscopy (IFS, e.g. Cappellari 2016; Sánchez 2020). Recent IFS galaxy surveys (IFS-GS) in the nearby universe ($z \sim 0.01$ – 0.03), like CALIFA (Sánchez et al. 2012), MaNGA (Bundy et al. 2015) or SAMI (Croom et al. 2012), have uncovered new spatial resolved relations that rules the star-formation and chemical enrichment in galaxies (e.g. Rosales-Ortega et al. 2012; Sánchez et al. 2014; Cano-Díaz et al. 2016; Lin et al. 2019; Sánchez et al. 2021a), defined which is their dynamical stage (e.g. Cappellari 2016; Zhu et al. 2018), and uncovered the patterns that define their mass assembly and metal enrichment (e.g. Pérez et al. 2013; González Delgado et al. 2016; Ibarra-Medel et al. 2016; Camps-Fariña et al. 2021), among many other results. Those explorations were possible thanks to the unique combination of (i) the use of statistically representative and significantly large samples of galaxies (from ~ 1000 to $\sim 10,000$ objects), (ii) a wide spectroscopic

coverage (from ~ 3600 Å up to $\sim 10,000$ Å) with intermediate resolutions ($R \sim 1000$ – 2000), (iii) the spatial coverage of a substantial fraction of their optical extension (between 1.5 to 2.5 effective radius, R_e), and (iv) a spatial resolution of ~ 1 kpc.

More recently, the advent of new IFS instruments (e.g., MUSE Bacon et al. 2010) and techniques (e.g., SITELLE Grandmont et al. 2012), that allow us to obtain natural seeing-limited spatial-resolved spectroscopic information covering a wide field-of-view (FoV, above ~ 1 arcmin²), has allowed to perform systematic explorations at a sub-kiloparsec scale. This has led to a new wave of IFS surveys and compilations, like GASP (Poggianti et al. 2017), AMUSING++ (López-Cobá et al. 2020) and in particular PHANGS-MUSE (Emsellem et al. 2022), that have improved our understanding of different processes, in particular those related with the details of star-formation and quenching mechanisms and the nature of diffuse ionized gas (e.g. Rousseau-Nepton et al. 2018; George et al. 2019; Vulcani et al. 2019; Belfiore et al. 2022; Pan et al. 2022; Pessa et al. 2022). These explorations highlight the importance of a improved spatial resolution when exploring galaxy properties using IFS. However, despite of their outstanding results, the explorations performed using MUSE or SITELLE present intrinsic problems due to the limitations in the spectral coverage compared to those of previous IFS galaxy surveys: for instance, the spectral range covered by

MUSE does not allow to sample important stellar spectral features like the 4000-break or emission lines like $[\text{O II}]\lambda 3727$. Therefore, it is important to determine if it is possible to improve the spatial resolution of already existing IFS GS data.

The seek for a improved spatial resolution and a complete sampling of the covered FoV using IFS data lead to the development of innovative observational techniques and cube reconstruction techniques in parallel with the development of the IFS-GS. Most of the surveys listed before (CALIFA, SAMI and MaNGA) adopted Integral Field Units (IFUs) that integrate fiber bundles as the basic systems to sample the observed objects in different discrete apertures (e.g., PPAK mode of the PMAS spectrograph Kelz et al. 2006; Roth et al. 2005). By construction the spatial resolution provided by those IFUs is limited by the fiber-size (convolved by the natural seeing). Furthermore, they present an incomplete coverage of the FoV (hexagonal or circular in general), sampling ~60-65% of it, depending of the fiber packing. To overcome those two limitations it was proposed an observational scheme that includes a minimum of three dithered exposures (Sánchez 2006; Mármol-Queraltó et al. 2011), to cover the entire FoV, and a flux-conservative variation of the Shepard’s interpolation method (Shepard 1968) to re-sample the discrete observations into a regular sampled datacube (Sánchez et al. 2012).

This scheme, with little variations, was adapted and adopted by the main IFS-GS described before, establishing a more or less standard procedure. One of the main requisites of this procedure is to reconstruct the image preserving the flux, minimizing the co-variance between adjacent data, and generating a PSF with the minimum possible structure. Due to that it was preferred to other schemes, like drizzling (e.g., García-Benito et al. 2015). However, this procedure does not guarantee that it is recovered the best possible spatial resolution of the data, that in general is more limited by the average distance between sampled points (Shannon 1948), and the natural-seeing, rather by the size of the original fiber (what defines and limits the minimum co-variance between adjacent spaxels). For this reason, the spatial resolution achieved was just slightly better than the original fiber size convolved by the natural-seeing PSF, ranging between 1.8'' (SAMI) and 2.4'' (CALIFA, MaNGA), despite the fact that the average distance between adjacent fibers is of the order of two times smaller in the case of SAMI than in the case of CALIFA.

In this article we present a remastered version of the extended CALIFA dataset (Lacerda et al. 2020; Espinosa-Ponce et al. 2020), in which we applied a new image reconstruction algorithm. We re-reduce just the data corresponding to the low-resolution setup (V500) and not those observed using the high-resolution one (V1200), as those ones have not suffered any significant increase in the number of objects since the last data-release (Sánchez et al. 2016b). The new data present a clear improved spatial resolution, achieving a PSF size near to the limit imposed by the natural seeing, preserving the photometry and the image quality. Similar improvements in the spatial resolution have been achieved by recent studies by adopting an *a posteriori* deconvolution scheme, wavelength-by-wavelength, to the reconstructed datacubes for the MaNGA survey (Chung et al. 2021). Despite of the clear improvements of that procedure, it essentially inheritate all the issues of the original observing procedure and adopted interpolation scheme, as already noticed and explored by Liu et al. (2020). In particular, those introduced by (i) the large size and aperture of the interpolation kernel, (ii) the possible mismatch of the foreseen dithering scheme and the actually adopted along the observations, and (iii) the inevitable problems in deriving and correcting for the differential atmospheric refraction (DAR) for different dithered pointings (e.g. Sánchez 2006; García-Benito et al. 2015; Law et al. 2015; Sánchez et al. 2016b). Our pro-

cedure involves a new interpolation scheme in which the spatial resolution is improved and the covariance minimized by implementing a narrower interpolation kernel, taking into account the observational adopted dither and the DAR at the moment of the image reconstruction, and correcting by the irregular shape of the PSF (introduced by the dithering and discrete sampling of the fiber bundle). Furthermore we introduce additional modifications to the existing data reduction pipeline (Sánchez et al. 2022b) that homogenize the dataset in terms of spectrophotometric calibration, mask and clean the foreground stars and improves the treatment of the vignetted and low-transmission/broken fibers.

Finally, we perform an *a posteriori* selection considering the quality of the data. In addition to the prior selection based mostly on the spatial coverage of the observed galaxies and their apparent magnitude, the selection function defines a sample of galaxies which main properties are described. We illustrate the quality and usability of the new reduced dataset for this final galaxy sample by exploring the main properties of the stellar populations and ionized gas at two different apertures: (i) the central region and (ii) a fully integrated aperture covering the entire FoV of the instrument. We present the main distributions of those properties as a function of the stellar masses and morphologies of the galaxies, comparing them with recent results in the literature.

The structure of this articles is as follows: (i) Sec. 2 describes the data adopted in this study; (ii) the modifications introduced in the reduction are described in Sec. 2.2, making a particular emphasis in new image reconstruction algorithm (Sec. 2.2.5) and its implementation in the cube reconstruction (Sec. 2.2.6); (iii) the identification of the galaxies and the derivation of their structural parameters is described in Sec. 2.3; (iv) the analysis of the quality of the data is introduced in 2.4, which leads to the selection of the final sample of galaxies described in Sec. 3; (v) the demonstration that this sample behaves primarily as diameter and magnitude limited sample, and the estimation of the volume correction is introduced in Sec. 3.1; (vi) the analysis performed on the new dataset is explained in Sec. 4, summarizing the adopted spectral fitting procedure (Sec. 4.1), and describing the main properties obtained for the stellar populations (Sec. 4.2) and the ionized gas (Sec. 4.4, 4.5 and 4.6); (vii) the results from this analysis are included in Sec. 5, describing the distribution of the stellar population (Sec. 5.1) and ionized gas (Sec. 5.2) as a function of the stellar masses and morphologies; (viii) the analysis is also used to characterize the spectrophotometric calibration, explore the behaviour of the residuals from the spectral fitting (Sec 5.3), how they compare with the errors estimated by the reduction and how the covariance affects their propagation (Sec. 5.4); (ix) a summary of the main results is included in Sec. 5.4. How to access to the delivered dataset and the results from the analysis is described in the CALIFA webpage¹.

Throughout this article we assume the standard Λ Cold Dark Matter cosmology with the parameters: $H_0=71$ km/s/Mpc, $\Omega_M=0.27$, $\Omega_\Lambda=0.73$.

2 DATA

2.1 Dataset

We collect all the data acquired by the 3.5m telescope at the Calar Alto observatory using the PMAS (Roth et al. 2005) IFS spectro-

¹ official: <http://califa.caha.es/>, mirror:http://ifs.astroscu.unam.mx/CALIFA_WEB/public_html/

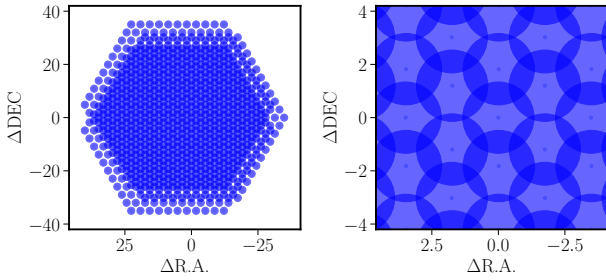


Figure 1. Example of the three dithering scheme adopted by the CALIFA survey. Left panel shows the distribution of the 993 fibers using the nominal offsets between the three individual pointings, that comprises 331 fibers each one. Right panel shows a zoom of the central region for the same distribution. In both panels the center of each fiber is represented by a blue point, and its corresponding aperture with a light-blue solid-circle. The typical distance between adjacent fibers ($\sim 1.5''$), the area covered by only one fiber (~ 2 arcsec²), and the overlapping region between adjacent fibers is evident in this figure.

graph in the PPAK mode (Kelz et al. 2006), using the same observing strategy as the one adopted by the CALIFA survey. This is, using the V500 grating, configured at the same goniometer angle, with the same integrating time (900s per pointing²), and the same dithering scheme as the one adopted by the CALIFA observations (see details in Sánchez et al. 2012, 2016b). This configuration corresponds to a low-resolution setup ($R \sim 850$, instrumental FWHM $\sim 6.5 \text{ \AA}$), that samples a wavelength range between 3745 and 7500 \AA , covering an hexagonal FoV of $74'' \times 64''$.

The science fiber-bundle of the PPAK IFU comprises 331 fibers with a $2.7''$ /diameter. Thus, the adopted dithering scheme provides with 993 individual sampling points of the FoV, with an average distance between adjacent fibers of $\sim 1.5''$. This involves an overlapping between the apertures of adjacent fibers, and therefore an inevitable co-variance between the information when applying any image reconstruction scheme using spaxels smaller than the original apertures. This reconstruction is required to fully correct some observational features, such as the DAR, as we will explain below. An additional consequence of this observing strategy is the differential depth achieved across the FoV, even for a target with a uniform light distribution, as there are regions sampled by three, two or one fiber, respectively. Figure 1 illustrates the final distribution of the PPAK science fibers adopting the nominal offsets defined by the CALIFA observing strategy, highlighting the overlaps between adjacent apertures. This is relevant for the modifications introduced in the data reduction.

We should recall that the original CALIFA survey observed a subsample of the objects using a V1200 setup, that provides with a higher spectral resolution covering only the blue regime of the optical spectral range. So far we have restricted the current analysis to the V500 setup only, comprising a total of 1088 individual observed galaxies. The final galaxy sample would be extracted from this compilation based on (i) the quality of the data and (ii) the properties of the galaxies themselves, as we will describe later-on.

2.2 Data Reduction

Data reduction (DR) was performed using a modified version of the CALIFA DR pipeline, formerly used in the third public data release (i.e., version 2.2 Sánchez et al. 2016b). This new DR-pipeline, version 2.3, comprises exactly the same reduction steps and procedures of the former version up to the very last steps that involve the cube reconstruction procedures. It follows the prescriptions described in (Sánchez 2006), using a modified version py3D (PI: B. Husemann) adapted to python3 as the basic reduction package.

The procedures in common with version 2.2 of the DR pipeline involve (i) pre-processing the raw data to unify the data read by the different CCD amplifiers (gluing in an homogeneous orientation, removing the bias and normalizing by the GAIN), and cleaning cosmic-rays, (ii) tracing the location across the CCD of the science and calibration spectra corresponding to each fiber, deriving simultaneously the FWHMs of the projected light-distribution in both the cross-dispersion and dispersion axis, (iii) an optimal extraction of the spectra using the tracing and FWHM derived in the previous step, correcting the data for the presence of stray-light, (iv) a wavelength calibration and regularization of the data following a linear wavelength solution (with 2 \AA per spectral pixel), (v) an homogenization of the spectral resolution along the wavelength range to its nominal value of FWHM = 6.5 \AA , (vi) a wavelength-dependence fiber-to-fiber transmission correction, (vii) a flux calibration using the standard transmission curve derived for the considered instrumental along the survey, (viii) a separation of the science, calibration and sky fibers, previous to the estimation and subtraction of the night-sky spectrum for each dither pointing, and finally (ix) an integration of the three dithering exposures into a single raw-stacked spectra (RSS) file, with each spectra/fiber associated to a particular (relative) location in the sky via a position-table (PT). As the variance and the masked regions (broken fibers, cosmic-rays, CCD defects and vignetted regimes) are propagated through the reduction, the final product of this set of procedures is a set of three RSS frames (flux, error and mask), each one comprising 993 spectra. All those procedures been extensively explained in detail in previous articles (Sánchez 2006; Sánchez et al. 2012; Husemann et al. 2013; García-Benito et al. 2015; Sánchez et al. 2016b).

We describe in more detail the modifications and new procedures introduced in version 2.3 of the DR pipeline, aimed to address different issues present on the data.

2.2.1 Preliminary astrometry

All eCALIFA observations were first reduced using version 2.2 of the pipeline. This provides with a reconstructed datacube that adopts a Shepard's interpolation scheme, with a sampling spaxel of $0.5''$ (Sánchez et al. 2016b). We synthesize the g - and r -band images from these datacubes, by convolving them with the corresponding filter responses. Then, adopting the nominal coordinates of the targets, we download two images of $2'$ and $10'$ size for the same bands from the PanStarrs (PS; Chambers et al. 2016; Flewelling et al. 2020) data archive corresponding to the PS1 public data release³. Using this dataset we perform a coordinates matching of the eCALIFA and PS r -band images, selecting by hand the center of each object and performing a baricenter estimation in a $10'' \times 10''$ box. Then, we perform a refined image registration by (1) matching the spatial resolu-

² for a handful targets the exposure time was slightly larger, ~ 1000 - 1200 s

³ <https://outerspace.stsci.edu/display/PANSTARRS/>

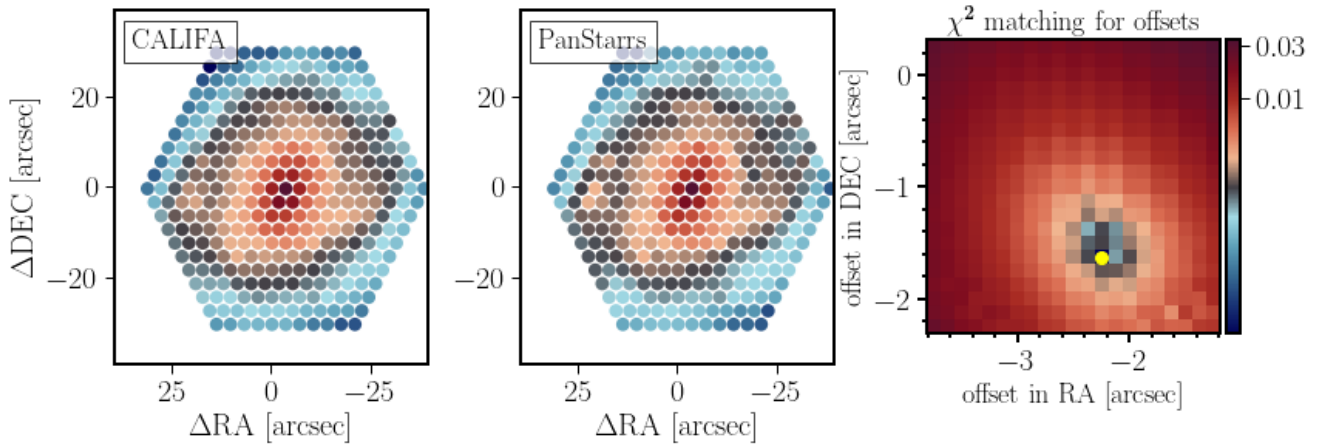


Figure 2. Illustration of the registration procedure for each individual dithering. *Left-Panel:* Distribution of flux intensities in the r -band synthesized from the 331 spectra obtained for the galaxy NGC 5947, corresponding to the 1st pointing of the three dithered exposures. *Middle-Panel:* Similar distribution derived by coadding the flux intensities in the corresponding PanStarrs r -band image for each aperture of each fiber, with the absolute location of the whole fiber-bundle shifted to match the flux intensities with those shown in the left-panel (i.e., the shift that minimizes the χ^2 value between both distributions). *Right-Panel:* χ^2 -map derived from the exploration of different offsets, with the location of the minimum value highlighted with a yellow solid-circle

tion of the PS images ($\sim 1.5''$) to that of the eCALIFA v2.2 cubes ($\sim 2.5''$), (2) reproject and resample the PS images to that of the eCALIFA ones, using the `REPROJECT_INTERP` routine implemented in the `REPROJECT` python module⁴, and finally (3) register the eCALIFA images to the PS one, by running the `CHI2_SHIFT` routine implemented in the `IMAGE-REGISTRATION PYTHON` package⁵. This procedure is repeated for both the g - and r -band images, and the average WCS recovered is adopted as the preliminary astrometry of the eCALIFA datacubes.

2.2.2 Dither Registration

The previous procedure was adopted assuming that the offset between each dithering pointing follows the nominal/foreseen one. However, it was already noticed along the CALIFA observations that this is not always the case (e.g. [García-Benito et al. 2015](#)). For this reason in previous versions of the pipeline it was adopted a procedure to (i) obtain an astrometric solution for each individual dither pointing, (ii) determine the real offsets between the three dithering exposures, and (iii) correct for the possible changes in the transparency of the atmosphere between them. This procedure uses a broad-band image as a reference. In previous versions of the reduction, it was adopted the SDSS r -band image ([García-Benito et al. 2015](#)). This choice was valid for the galaxies in the original CALIFA sample, since they were all extracted from the SDSS catalog. However, our extended sample comprises galaxies that have not been necessarily observed by SDSS survey. For this reason we adopted the r -band images provided by the PS survey, already described before.

The procedure is indeed very similar to the `CHI2_SHIFT` algorithm indicated before, but implemented for discrete dataset (i.e., not regular grided images). First, the integrated flux is synthesized through the r -band filter using the RSS data of each pointing, obtaining 331 photometric measurements (one for each science fiber). Then, it is estimated the same flux intensities from the reference image using the fiber apertures at the expected location on the sky based on the

preliminary astrometry described before. Afterwards, we compare the two photometric datasets, obtaining the corresponding χ^2 distribution. The procedure was repeated by shifting the assumed coordinates of the target within a box of $20''$ width in both RA and DEC, following a regular grid with a step of $1.5''$ (in both directions). This generates a χ^2 map, which minimum value is considered as the first guess of the ΔRA and ΔDEC required to match the coordinates of the target to that of the reference image. Finally the whole procedure is repeated one more time by limiting the search around this new coordinate using a smaller box $2.5''$ width and a step of $0.125''$. Once the offsets that minimize the χ^2 are found, the photometric values are re-evaluated deriving the average ratio between the flux intensities measured through the fibers and those derived from the reference image.

Figure 2 illustrates this procedure, showing the r -band photometric values extracted from one dither exposure on the galaxy NGC 5947, the corresponding values extracted from the PS image at the location that minimizes the χ^2 , and finally the χ^2 map derived from the second iteration described before. This procedure provide with (1) the best absolute astrometric solution for each pointing, (2) the real offset between each dithering, and (3) a flux re-calibration of each dither-pointing that anchors the photometry to that of the reference image, limiting any possible relative photometric fluctuation between each individual pointing (due to variations in the atmospheric conditions along the observing process).

2.2.3 Broken fibers

Along the full decade in which the data was taken the PPAK fiber-bundle has suffered an inevitable aging process. Due to that a set of broken fibers has appeared. For the first observations, covering the first four years, no fiber present a degradation of the transmission. Afterwards, three fibers present a continuous degradation. This number increased to five fibers in the last two years of the collected period, with a negligible transmission in the last observations. In previous versions of the DR these fibers were identified by hand and masked. In this new version we introduce a procedure that automatically detects those fibers and replaces the spectra by an inverse-

⁴ <https://reproject.readthedocs.io/en/stable/index.html>

⁵ <https://pypi.org/project/image-registration/>

distance weighted average-spectra of the 5th nearest (non broken) fibers.

2.2.4 Vignetted regions

As extensively described in different articles (e.g. [Sánchez et al. 2012, 2016b](#)), a 30% of the fibers are affected by different degrees of vignetting. This effect degrades the transmission down to a 30-50% in the extremes of the wavelength range, with a fully unvignetted regime between 4240-7140Å, in the worst cases. Due to the particular correspondence between the location of fibers in the science bundle and the entrance of the spectrograph (and final location in the CCD), those spectra correspond to fibers located on an annular ring at $\sim 15''$ from the center of the FoV. However, not all spectra in this location are affected by vignetting. Thus, there are fully unvignetted spectra spatially adjacent to any set of vignetted ones. Using this property we apply a procedure similar to the one adopted to correct the effects of broken-fibers, replacing the vignetted regime of the spectra of those fibers affected by this effect by a flux-scaled version of the inverse-distance weighted average-spectra of the 5th nearest (fully unvignetted) fibers. We selected as vignetted those regions in which the transmission is a 70% of the average transmission within a considered fiber. Despite of the benefits of both procedures, we keep a record of those modified regions in the propagated mask frame.

2.2.5 Image reconstruction

One of the main goals in the new reduction is to increase the spatial resolution of the delivered datacubes. As indicated in the introduction, the intrinsic spatial resolution is limited more by the distance between sampling elements ($1.5''$, defined by the dithering pattern) than by the size of those elements ($2.7''$, defined by the aperture of the fibers). However, in practice, the spatial resolution is strongly affected by the method adopted to reconstruct the cubes/images and the parameters adopted in the interpolation kernel. For instance, the main goal of the method adopted in previous versions of the CALIFA pipeline to reconstruct the cubes was to provide with a final smooth PSF, without evident sub-structures from the dither pattern, preserving the spectrophotometry ([Sánchez et al. 2012](#)). To provide with the best possible spatial resolution was not among its main priorities. Indeed, other reconstructions procedures that produce better spatial resolutions has been explored before. For instance, [García-Benito et al. \(2015\)](#) experimented with the use of the drizzle method ([Fruchter & Hook 2002](#)) in the CALIFA data, which produces a sharper PSF, but with a considerable amount of sub-structures (i.e., a PSF with secondary peaks). More recently, [Liu et al. \(2020\)](#) adopted a covariance-regularized reconstruction procedure to reconstruct the cubes from the MaNGA dataset. This method slightly improves the spatial resolution and limit considerably the covariance between adjacent spaxels. Finally, [Chung et al. \(2021\)](#) performed a spatial deconvolution of the original MaNGA cubes, without introducing a new image reconstruction procedure, by adopting the SDSS images a guidance for the deconvolution process. The method we describe in this section introduces a modification in the image reconstruction algorithm, following [García-Benito et al. \(2015\)](#) and [Liu et al. \(2020\)](#), with the ultimate goal of improving the spatial resolution. We finally implement a deconvolution process just to mitigate the effects of a complex PSF. This deconvolution improves slightly the spatial resolution, but it is not the main reason of the achieved/improved spatial resolution. In this regard our method departs considerably from the one introduced in [Chung et al. \(2021\)](#).

As indicated before, the image reconstruction in previous version of the pipeline adopted a modified version of the Shepard's interpolation method, being broadly adopted in the reduction of fiber-based IFS datasets that adopts a dither scheme (with certain variations [Law et al. 2015](#); [Green et al. 2018](#)). This method assign to a certain spaxel⁶ a flux that results from the weighted-sum of all fluxes from all fibers within a certain distance:

$$f_{i,j} = N_{i,j} \sum_k f_A w_{k,i,j} F_k \text{ where } d_{k(i,j)} < d_{lim} \quad (1)$$

where k is the index of the fibers contributing to the flux in the spaxel (i,j) , denoted as $f_{i,j}$. Only those fibers within a certain distance to the considered spaxel, d_{lim} , are considered to contribute to its flux. f_A is a scaling parameter corresponding to the ratio between the area covered by each original fiber and the one covered by the final spaxel. In previous versions of the pipeline this factor was 5.64, as the PPAK fibers have a diameter of $2.7''$ and the final spaxel a size of $1'' \times 1''$. F_k is the flux within a certain fiber, and $w_{k,i,j}$ is the weight (or interpolation kernel):

$$w_{i,j,k} = \exp -0.5 \left(\frac{d_{k(i,j)}}{\sigma} \right)^\alpha \quad (2)$$

where $d_{k(i,j)}$ is the distance between the fiber k and the considered spaxel, σ is a parameter controlling the width of the kernel, and α is a parameter controlling its shape. $N_{i,j}$ is just the normalization factor, i.e., the inverse of sum of all $w_{i,j,k}$ contributing to the flux in the spaxel (i,j) .

The adopted parameters for the image reconstruction changed along the different implementations of the data reduction. In early versions of the DR, we adopted the following values: $\sigma = 1.0''$, $\alpha=1.0$ and $d_{lim} = 5''$ (ver. 1.2 and 1.3 [Sánchez et al. 2012](#); [Husemann et al. 2013](#)). Different explorations lead to a tuning of those parameters, that produce an sharper image and a lower co-variance between adjacent spaxels: $\sigma = 0.75''$, $\alpha=1.0$ and $d_{lim} = 3.5''$ (ver. 1.5 and 2.2 [García-Benito et al. 2015](#); [Sánchez et al. 2016b](#)). The FWHM of the reconstructed cubes was estimated using the same algorithm described above, when describing the preliminar astrometry: the r -band image extracted from the IFS data was compared, by a χ^2 , with a reference r -band image, convolved with a sequence of Gaussian functions of different width. The best-matched image provides with an estimation of the FWHM of the PSF. In average it was found a value of $\sim 2.4''$ /FWHM for the DR3 CALIFA dataset ([Sánchez et al. 2016b](#)).

To optimize the procedure it is required to explore which are the set of parameters that reproduce better the original image (i.e., the one provided by the natural seeing). Since we do not have a direct image in a wavelength covered by the spectroscopic data taken simultaneously to the observations, once again, we adopted as a guiding images the PS g - and r -band images. On these images we simulate the observations performed using the CALIFA setup, following the same procedure described before i.e., we extracted the flux corresponding to each fiber, following the nominal dither pattern). Then, we use this simulated observation to explore different image reconstruction schemes. The procedure is illustrated using NGC 5947 as an archetype CALIFA galaxy. Figure 3 shows how the original image of this galaxy (a panel) compared with both the flux distribution through the three dithered exposures (b panel) and the reconstructed image using the parameters adopted in the previous version

⁶ understood as the final sampling element of the outcome datacube

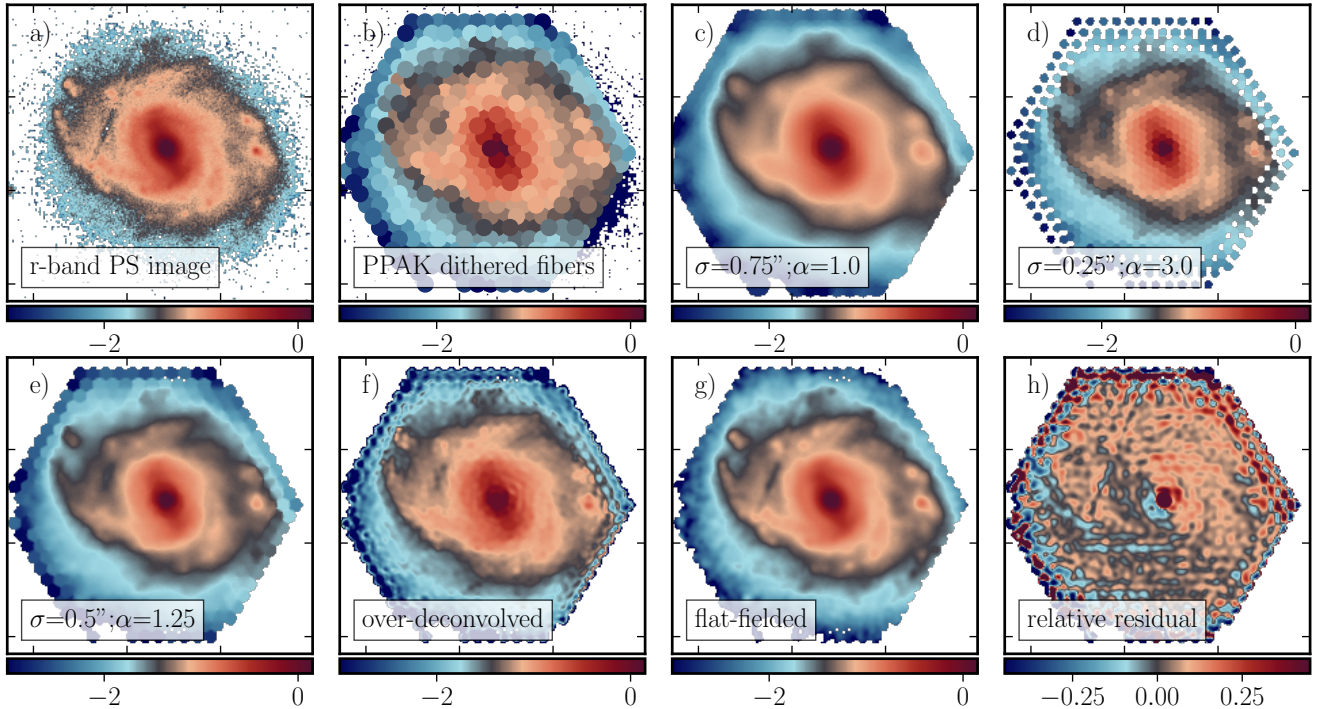


Figure 3. Illustration of the new image reconstruction procedure. Each panel shows: (a) PS r -band image of the archetype galaxy NGC 5947; (b) discrete distribution of the r -band flux intensities extracted for the 993 individual spectra corresponding to the three dithering pointings observed with the 331 PPAK science fibers (color solid-circles). Note the overlapping between adjacent fibers due to the adopted dithering scheme; (c) r -band reconstructed image using the distribution of flux intensities shown in panel *b* using the interpolation scheme and parameters adopted in the previous version of the data-reduction (i.e., Eq. 1, with $\sigma=0.75''$ and $\alpha=1.0$); (d) similar reconstructed image using a sharper interpolation kernel (i.e., Eq. 1, with $\sigma=0.25''$ and $\alpha=3.0$); (e) similar reconstructed image using the parameters finally adopted in current version of the data reduction (i.e., Eq. 1, with $\sigma=0.5''$ and $\alpha=1.25$); (f) image obtained by deconvolving the image shown in panel *e* using a large number of iterations in the deconvolution algorithm as indicated in the text. Note the patchy distribution with unreal sub-structures generated by the deconvolution algorithm; (g) final image generated by the full reduction algorithm, including the final flat-fielding procedure introduced in (García-Benito et al. 2015); (h) residual image obtained by subtracting the final reconstructed image shown in panel *g* to the PS r -band image shown in panel *a* (matching the spatial resolutions), relative to this later image. The difference between both images is below a $\sim 10\%$ for most of the FoV, with larger differences found in the very central and very outer regions ($\sim 30\%$).

of the DR (*c* panel). The resolution degradation is clearly appreciated when using the same parameters for the interpolation Kernel (eq. 2) adopted in the previous reductions of the CALIFA dataset.

We explore a wide range of values for the considered parameters ($0.15 < \sigma < 1.5$; $\Delta_\sigma = 0.15$, $0.75 < \alpha < 4.0$; $\Delta_\alpha = 0.25$), finding that the FWHM of the reconstructed image increases with σ (i.e., the kernel width), and decreases with α (i.e., the kernel sharpness). Thus, in principal the smaller σ and the largest α may produce the best reconstructed image in terms of its PSF FWHM (i.e., a better resolution). Indeed, for certain combination of parameters the recovered FWHM is well below the one obtained using the nominal parameters adopted in the previous reductions of the CALIFA dataset (i.e., $\text{FWHM} < 2.5''$). However, resolution is not the only parameter to take in place when weighting the quality of the reconstructed image. A narrow and sharp interpolation kernel produces a reconstructed image with a lot of non-realistic substructures, as illustrated in Fig. 3 *d* panel ($\sigma = 0.25''$ and $\alpha = 3.0$). Those artifacts can be characterized by the standard deviation of the residual image derived from subtracting the best-matched image (i.e., the reference image convolved with a Gaussian kernel to match the resolutions) to the reconstructed image. As indicated before, this standard deviation increases as sharper is the interpolation kernel. Thus, the optimal parameters for the image reconstruction procedure result from a com-

promise between minimizing both the FWHM and the standard deviation of the residuals. This is achieved when $\sigma = 0.5''$ and $\alpha = 1.25$. Fig 3, panel *e*, shows the reconstructed image when adopting both values for the interpolation kernel. The improvement in the resolution with respect to the image obtained when using the parameters adopted in the previous version of the reduction (panel *c*) is evident ($\text{FWHM}_c \sim 2.5''$ vs. $\text{FWHM}_e \sim 1.8''$). However, the resolution is still worse than that of the original image (panel *a*, $\text{FWHM}_a \sim 1.0''$), and lower than the ultimate goal based on the sampling of the dithering scheme ($\sim 1.5''$). Furthermore the PSF present a complex structure, due to the adopted reconstruction scheme.

In order to improve furthermore the resolution and mitigate the presence of secondary peaks/substructures in the reconstructed PSF when using a sharp interpolation kernel (Fig. 3, panels (d) and (e)) we followed an approach somehow similar to the one adopted by (Chung et al. 2021), i.e., we perform a deconvolution of the reconstructed image with a PSF. The choose of a realistic PSF is very important when applying a deconvolution procedure. Therefore, a particular care was taken during this process. First, we assume that the natural seeing PSF in the focal plane of the 3.5m telescope at Calar Alto is well represented by a Gaussian function, following Sánchez et al. (2008). Introducing more complex shapes, like a Mof-fat function, does not increases significantly the characterization of

the shape of the PSF (e.g. [García-Benito et al. 2015](#)). Considering the average seeing in the observatory ($\sim 0.9''$ [Sánchez et al. 2007](#)), and the turbulence introduced by the dome ($\sim 10\%$ in the best case [Sánchez et al. 2008](#)), a Gaussian function with a width of $\sigma = 0.5''$ (FWHM $\sim 1.3''$) is indeed a good representation of the typical PSF at the entrance of the IFU. However, this is not by far a good representation of the PSF for the reconstructed images, which shape and structure are vastly dominated by the fiber-size, fiber-bundle pattern, dithering scheme and adopted image reconstruction procedure (e.g. [Sánchez 2006](#)). Thus, to generate a realistic PSF we followed the same procedure adopted to generate the reconstructed image, i.e., we extract the flux through the dithered-fiber apertures and we adopted the same image reconstruction procedure and same parameters. Then we deconvolve the image using the Richardson-Lucy algorithm ([Richardson 1972](#))⁷ implemented in the `RESTORATION` module of the `SCIPY` python module. We should note that this procedure involves a further optimization, as this algorithm requires two parameters. One defines a threshold below which the values are set to zero to reduce the noise (and ghost generation) in the deconvolved image. The other is the number of iterations for which the algorithm is performed. A larger number of iterations generates sharper images. However it produces, again, a PSF with unreal substructures and ghosts due to noise aggregation. This is appreciated in Fig 3, panel *f*, where it is shown the result of a deconvolution adopting a very low threshold level corresponding to 1% of the 1σ noise level, and a large number of 50 iterations of the deconvolution algorithm. This is an example of an over-deconvolution of the data, that introduces unreal sub-structures in the PSF, degrading the image quality.

We followed a procedure similar to the one adopted to define the optimal parameters of the image reconstruction kernel to estimate the optimal parameters to adopt in the deconvolution procedure. Thus, we run the algorithm covering an ample range of thresholds (from 10 to 0.01σ) and number of iterations (from 1 to 100), evaluating final FWHM of the reconstructed image and the standard deviation of the residual (σ_{res}) when comparing with the original image. To evaluate both the FWHM and σ_{res} we convolve the original image with a set of Gaussian functions of variable width and compare them with the reconstructed images using a χ^2 criterion. The image that minimize this χ^2 provides with the FWHM of the final PSF (i.e., the quadratic propagation of the FWHM of the PSF of the original image and the width of the convolved Gaussian function), and the σ_{res} (the standard deviation of the residual of the difference between the reconstructed and the convolved images). We find that a threshold corresponding to $\sim 2\sigma$ the noise level, and just 5 iterations of the deconvolution algorithm provides the best compromise between minimizing both the FWHM and σ_{res} . As described before larger (lower) number of iterations decreases (increases) the FWHM, but σ_{res} increases (decreases). The final FWHM estimated for panel (f), is $1.65''$, which is significant improvement with respect to the value prior to deconvolving the image ($\sim 8\%$ FWHM reduction). However, we remind the reader that most of the improvement in the resolution was a result of the selection of a new set of parameters for the interpolation kernel, as indicated before ($\sim 28\%$ FWHM reduction)

As a final refinement, following [García-Benito et al. \(2015\)](#), we generate a flat-field as the ratio between the convolved PS image (i.e., PSF-matched) and the reconstructed image from the deconvolved spectral data, what removes any final defect. The application of this flat-field solve some minor photometric differences between

Table 1. Description of the DRSCUBE file.

HDU	EXTENSION	Dimensions ¹	Format
0	PRIMARY	(159, 151, 1877)	float64
1	ERROR	(159, 151, 1877)	float32
2	ERRWEIGHT	(159, 151, 1877)	float32
3	BADPIX	(159, 151, 1877)	uint8
4	FLAT	(159, 151)	float64
5	GAIA_MASK	(159, 151)	int64

(1) The actual spatial dimensions may change galaxy by galaxy, depending on the real dither scheme adopted during the observations.

the three dithering pointings and anchor the absolute photometry to the reference one (i.e. PS), being already discussed in detail in [García-Benito et al. \(2015\)](#) and [Sánchez et al. \(2016b\)](#). Fig. 3 includes the final reconstructed image once applied the full procedure (panel *g*) and the residual with respect to the original image (panel *h*). The comparison between the reconstructed images corresponding to the procedure adopted in the previous data-reduction (Fig. 3, panel *c*), and the new procedure (Fig. 3, panel *g*), illustrates the clear improvement of the new procedure. Quantitatively, the reconstructed PSF has a FWHM of $\sim 1.65''$, for the archetype image that illustrates the procedure, that has an original (natural seeing) PSF FWHM of $\sim 1.4''$. We should note that this FWHM is not affected by the flat-fielding process in any way. This is a significant improvement compared to the FWHM of the PSF provided by the previous version of the image reconstruction procedure ($\sim 2.4''$). The major drawback of the adopted procedure, as indicated before, is that it relies on the quality of the reference image. Therefore, any defect of problem on that image is propagated to the final reconstructed one due to the flat-fielding procedure.

2.2.6 Cube reconstruction

The new image reconstruction procedure described before is fully implemented in the data reduction in the following way: (1) for each wavelength along the sampled range it is generated a reconstructed image using the corresponding monochromatic flux intensities sampled by dithered fibers, taking into account the offsets introduced by the DAR, and using the interpolation kernel defined in Eq. 2 and the optimal values for the σ and α parameters obtained from the experiment described before; (2) the resulting image is deconvolved using a PSF generated using the same reconstruction algorithm; (3) along this process and error propagation is performed adopting a Monte-Carlo iteration with 100 loops, perturbing the flux intensities measured through the fibers and repeating steps (1) and (2). The mean image from this MC iteration and the corresponding standard deviation are stored, being adopted as the reconstructed image and error at the considered wavelength; (4) once this procedure is iterated over all the wavelength range a datacube is obtained. From this datacube we generate the *g*- and *r*-band images, by convolving the corresponding filter curves with the spectra at each spaxel. Those images are used to derive the final flat-field and FWHM, following the procedure described in the previous subsections (i.e., they are compared based on a χ^2 with a set of Gaussian convolved PS *g*- and *r*-band images). The procedure to estimate the FWHM was introduced and described in detail in [García-Benito et al. \(2015\)](#), and adopted in further IFS studies (e.g. [Law et al. 2015](#); [Yan et al. 2016](#); [Sánchez et al. 2016b](#)). This methodology is robust, as it was demonstrated in [García-Benito et al. \(2015\)](#) and [Sánchez et al. \(2016b\)](#) by

⁷ https://en.wikipedia.org/wiki/Richardson-Lucy_deconvolution

comparing its results with those obtained by measuring the FWHM directly on cube-reconstructed images corresponding to calibration stars. We adopted the r -band derived flat-field for all the wavelengths, as we find not significant difference in using this one, the g -band one or a combination of both. We should highlight that the flat-field is purely monochromatic, and it is not fine tuned for each different wavelength. We note again that this flat-field was already introduced as part of the reduction of the CALIFA data in [García-Benito et al. \(2015\)](#), being applied in the previous version of the data-reduction ([Sánchez et al. 2016b](#)).

2.2.7 Foreground stars masking

Following the procedure described in [Sánchez et al. \(2022b\)](#), we search for the possible foreground field stars in the FoV of the analyzed datacubes. We use the Gaia DR3 catalog⁸ ([Gaia Collaboration et al. 2016, 2021](#)), that comprises the most complete and accurate survey of stars covering the full sky, at least regarding its astrometric solution. We selected only those sources with a measured parallax at least five times higher the reported uncertainty, to ensure that they are Galactic stars. Then, we generate a mask covering a circular aperture of $2.5''$ around each star with the spatial size format and astrometric solution of the reduced datacube. This mask will be used later on when analyzing the data. We found a foreground star in $\sim 25\%$ of the datacubes.

2.2.8 Format of the reduced data

For a more simple distribution, the final outcome of the reduction is stored in a single file for each observed object. We adopted a format similar to the one implemented in the CALIFA DR3 ([Sánchez et al. 2016b](#)), and other IFS Galaxy Survey released (e.g., MaNGA format [Abdurro'uf et al. 2021](#)). It consists on a multi-extension FITS-FILE, in which each extension comprises a particular outcome of the reduction. Table 1 lists each of the extensions in the file, their format and dimensions. The first four extensions consists of a set of datacubes. The first one (PRIMARY) comprise the flux intensity spectra corresponding to each spaxel, with the corresponding error stored in the second extension (ERROR). The required weights to include in error propagation due the different coverage of the dither pattern (i.e., due to the fact that each spaxel is covered by a different number of fibers), as described in Sec. 2, is included in the third extension (ERRWEIGHT). The fourth extension (BADPIX) store the bad-pixel mask. The two final extensions store two images, the flat-fielding described in Sec. 2.2.6, and the mask of the foreground stars described in Sec. 2.2.7.

These files are named after the original object name included in the PMAS software during the observations, adopting the nomenclature CUBENAME.V500.DRSCUBE.FITS.GZ, where CUBENAME corresponds to the OBJECT header in the original FITSFILE. We distribute these datacubes in the following web page: <http://ifs.astroscu.unam.mx/CALIFA/V500/v2.3/reduced/>, comprising a total of 1116 datacubes.

2.3 Galaxies segmentation and structural properties

In some cases more than one galaxy is observed within the FoV of the instrument. As one of the goals of this exploration is to provide with a final galaxy sample, including its individual observational

Table 2. Description of the QC file.

column	value	meaning
Name	cubename	Prefix of the reduced datacube
QC_flag	0	OK: Everything seems to be ok in the data.
	1	BAD: The data are bad for a reason indicated below. They should not be used.
	2	WARNING: The data present some problems, but they can be used for most science cases.
Reason	0	No QC issue found.
	1	The targets galaxy is considerably larger than the FoV of the instrument.
	2	Severe problems with the spectra, very low-S/N, problems with the sky-subtraction.
	3	Non severe problems with the spectra, affecting just a small region within the FoV.
	4	The galaxy is too small compared to the FoV, it is essentially unresolved.
	5	Repeated observation of the same galaxy.
	6	FoV crowded with field stars affecting a significant fraction of the FoV.
	7	A single very bright field star is affecting a significant fraction of the FoV.
	8	Evident problem in the absolute spectrophotometric calibration.
	9	Problem with the image reconstruction procedure or defects in the PS g -band image.
	10	Spectroscopic and photometric derived stellar masses do not match.
11	The stellar population analysis does not provide a reliable result.	
Multiple	0	Only one galaxy detected in the FoV.
	1	Multiple galaxies detected in the FoV.

(and physical) properties, we have performed an identification of the objects in the field, segregating them, to treat them separately in further analysis. For doing so, we make use of the routines included in the PHOTUTILS python package. We obtain from the PS survey a square $10'$ size g -band image centred in location of each observed cube. On this image we detect all the objects detected about 2σ the noise level, and based on an analysis of the ellipticity and the size, we select all the stars in the field. This allow us to: (i) estimate the FWHM of the g -band image, a required input of the reduction as indicated before; (ii) detect small objects or faint stars not included in the Gaia survey, that should be masked from the data too; (iii) estimate the local background and noise level around the science target in this image. Then, we select a central square image of $1.5'$ size, mask the field stars, remove the background and perform an isophotal analysis of each galaxy detected within the FoV of the original IFS data. This isophotal analysis comprises the derivation of the surface-brightness, ellipticity and position angle profiles, together with the estimation of the baricenter and effective radius. We selected as representative position angle and ellipticity the one corresponding to a g surface brightness of $22 \text{ mag arcsec}^{-2}$. Then, the effective radius is found by deriving the cumulative flux in successive radial apertures along the semi-major in elliptical apertures following the previous estimated position angle and ellipticity. Finally a new segmentation map is generated with the same spatial size and astrometric solution of the reduced datacube.

When more than one galaxy is detected in the FoV of a single

⁸ <https://www.cosmos.esa.int/web/gaia/dr3>

datacube the mask generated by the previous procedure is used to segregate them. This way, a set of copies of the reduced datacube is created, each one corresponding to each of the different detected galaxies, masking the rest of them. The new files adopt as prefix the parent CUBENAME (Sec. 2.2.8), with a running index corresponding to each galaxy (i.e., CUBENAME.I, where I runs from 0 to the number of galaxies). An index corresponding to the ID in the original segregation mask is stored in the header in the LABEL keyword. Finally, the baricenter of each object and the coordinates in the sky are stored in the XC, YC, RA and DEC header keywords. On the other hand, if only one galaxy is detected in the FoV, it is created just a copy of the data cubes including the corresponding header keywords.

Finally, the stars detected within the field-of-view by this analysis and those included in the GAIA.MASK extension of the reduced data are masked from the datacubes, interpolating the flux intensities within each of those masks. This interpolation is just adopted for future explorations of extensive quantities (e.g., the total stellar mass). For spatial resolved analysis we recommend to mask those regions and exclude them.

We found 22 datacubes with multiple galaxies detected within the FoV, in most of the cases two galaxies (only in 4 cases we found 3 galaxies). For completeness we distribute those (i) galaxy-segmented and (ii) field-stars mask interpolated FITSFILES, using the same format described in the previous section (Sec. 2.2.8), through the webpage http://ifs.astroscu.unam.mx/CALIFA/V500/v2.3/reduced_masked/.

2.4 Data Quality

A quality control procedure is implemented to determine which data are fully useful, flagging out the poor quality ones and indicating with a warning those data that are still useful for most of the science cases but may be taken with care for particular explorations. The quality of data is weighted based on a set of simple visual, qualitative and quantitative analysis: (i) first, we flag as bad those datacubes that do not sample the center of the galaxies, covering just a small portion of its optical extension (i.e., $\text{FoV} \ll \text{Re}$), and datacubes corresponding to galaxies too small compared to the original fiber size ($\text{Re} \lesssim 5.0''$), i.e., unresolved targets; (ii) a visual inspection of the central aperture ($1.5''/\text{diameter}$) and the FoV-integrated spectra and the synthesized u -, g - and r -band images allows to identify evident bad quality data, that usually corresponds to very low-S/N data and/or problems with the observations that are also evident in the QC-flags included in version 2.2 of the data reduction (strong stray-light, electric background, problems with the tracing and extraction of the spectra, problems with the sky subtraction, as described in Sánchez et al. 2016b). When those problems are observed, but they affect just a few locations within the FoV or a limited spectral range, and the central and integrated spectra does not show evident defects, then the datacubes are flagged with a warning; (iii) repeated observations on the same field are compared, the best quality one is selected and the worst one is flagged as bad, to avoid duplication in the final galaxy sample; (iv) the presence of a large number of field-stars or a single bright star, contaminating a substantial fraction of the FoV, is considered a reason to flag a datacube as either bad or with a warning (depending on the relative importance of the contamination); (v) when there is a clear absolute or relative (blue-to-red) photometric mismatch between the datacubes and the PS observations is used to flag the quality of the data; (vi) a visual inspection of the reconstructed g -band image and its comparison the corresponding PS image (e.g., Fig. 3, panels g and h), is used to identify clear

problems (e.g., errors in the estimated dithering pattern, image reconstruction algorithm, astrometric issues); finally we perform two additional tests following (Sánchez et al. 2022b), (vii) we compare the stellar masses derived using the photometric and spectrophotometric information, and (viii) we fit the central and integrated spectra using `pyFIT3D` to identify possible issues/problems not evident based on a pure visual inspection. We will provide more details on these two particular analysis in the forthcoming sections.

It is possible that one cube is affected by more than one quality issues. In this case the table reflects that issue with the strongest/worst impact in the quality of the data.

Of the total number of 1116 datacubes, 895 has been classified as good quality. Of them, 392 present some warning (i.e., a minor issue as described before), and 490 passed all the explored quality criteria. A total of 234 cubes were rejected. This may be considered as considerable large fraction ($\sim 20\%$ of the observed cubes). However, the vast majority are rejected not due to its intrinsic bad quality, but due to the fact that they correspond to observations covering just a small fraction of the targeted object, or because the target object is too small for a proper spatial resolved analysis. We provide with some characteristic of the good quality dataset.

2.4.1 Spectrophotometric accuracy and precision

We gauge the accuracy and precision of our spectrophotometric calibration by comparing the r -band magnitudes and $g-r$ colors derived from the datacubes with those extracted from the PS images. For this calculation we use the segmentation maps described in Sec. 2.3, co-adding the fluxes within each segmentation corresponding to each detected galaxy in the PS images corresponding to the g - and r -band, and the same image bands synthesized from the reduced datacubes. Figure 4 shows the comparison between r -band magnitudes and $g-r$ colors for both datasets. There is a remarkable good agreement, with a distribution almost following the one-to-one relation, and with an average offset of -0.06 mag for the magnitude and -0.07 mag for the color. These offsets corresponds to just a 2-3% mismatch in the absolute spectrophotometric and blue-to-red calibration between our reduced datacubes and the PS photometry. The difference between the r -band magnitudes present a standard deviation of 0.22 mag, that corresponds to a precision in the absolute photometric calibration of $\sim 9\%$. On the other hand, we estimated the blue-to-red spectrophotometric precision, based on the dispersion in the difference between the $g-r$ colors (~ 0.09 mag), in $\sim 4\%$. Those numbers are similar to the ones reported in previous DR of the CALIFA survey (e.g. Sánchez et al. 2016b) and of the same order and those found by other IFS surveys (e.g. Abdurro'uf et al. 2021). As discussed on those articles there are multiple reasons for these differences, but the dominant one is the slight differences in the nominal transmission curve of the filters adopted to estimate the photometric values from the datacubes (Gunn et al. 1998) and the real transmission curves of the PanStarrs observations (Stubbs et al. 2010). Those curves result from the convolution of the nominal curves with the optical system conformed by the telescope and instrument, that are difficult to reproduce.

2.4.2 Depth and signal-to-noise

The depth of the datacubes is gauged by estimating (i) the V -band surface brightness magnitude (and flux intensity) at the 3σ level for those datacubes fulfilling our good quality criteria in which this limit is reached, and (ii) the typical S/N at the effective radius. Figure 5

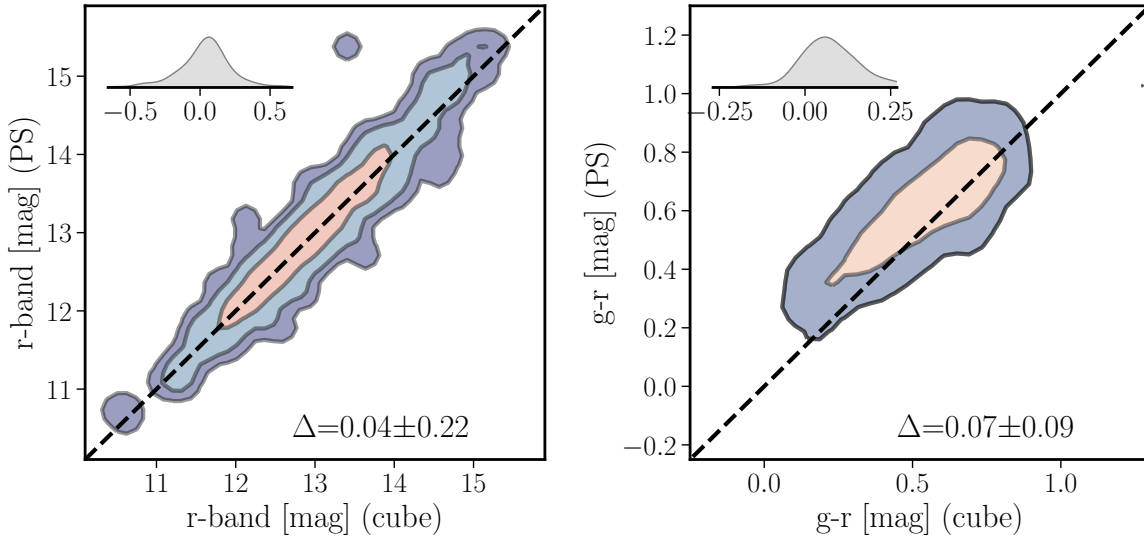


Figure 4. Comparison between the r -band magnitudes (left panel) and $g-r$ colors (right panel) derived for the final sample of good quality datacubes using the segmentation maps described in Sec. 2.3 for the PS images and the images synthesized from the IFS datacubes. Each successive contour corresponds to a density distribution containing a 99%, 95% and 65% of the total sample. The inset shows the kernel density distribution of the difference between both quantities, with the average (and standard deviation) value indicated as a legend.

shows the distribution of both quantities, showing a wide range of values, from S/N from 10 to 40, and with μ_V from 21.7 to 24.5 mag arcsec⁻², with a typical value of S/N \sim 20 and $\mu_V \sim$ 23.6 mag arcsec⁻². This later value corresponds to a flux surface intensity of $\sim 1 \cdot 10^{-18}$ erg s⁻¹ cm⁻² Å⁻¹ arcsec⁻². There is a clear trend between both quantities, with datacubes reaching a lower surface-brightness magnitude as higher is the S/N at Re, following a non-linear relation reaching a somehow asymptotic value at high-S/N. These distributions, trends, and typical values are indeed very similar to the values already reported in previous CALIFA data-releases (e.g. Sánchez et al. 2016b).

2.4.3 Seeing and spatial resolution

One of the main goals of the current re-reduction of the data is to achieve a better spatial resolution. Along the reduction the FWHM of the PSF is estimated (Sec. 2.2.5). This estimation is not very precise, due to the nature of the computation. Indeed in many cases the FWHM estimated by the reduction procedure is poorly constrained (i.e., a wide range of values provide similar likelihoods)⁹. However, for most of the galaxies is the only estimation we have. This value can be compared with the natural seeing FWHM provided by the Calar Alto seeing monitor (RoboDIMM). For doing so we downloaded all the available values provided by this monitor and cross-match the observing date/time for the three different pointings of each datacube with the date/time included in the seeing monitor catalog. We allow for a range of 20 minutes difference between both times, considering the exposure time and overheads of each observation. We finally obtain the average seeing FWHM reported by the monitor within in this range. The RoboDIMM is not always active when observations are taking place, being active of about 2/3 of the

⁹ Note that this does not affect the reduction itself significantly, as the estimated FWHM is applied to derivethe last flat-fielding described in Sec. 2.2.5, that introduces minor changes

observing periods. We end-up with a subset of 372 estimations of the FWHM for both the datacube PSF and the seeing monitor. Figure 6 shows the comparison between both quantities, showing a clear correspondence between both of them, nearly following a one-to-one relation. This is very encouraging as it shows that our estimation of the FWHM PSF is not off by a significant quantity. However, the trend present an offset at low values, with the FWHM PSF showing lower values than the natural seeing one below 1.0". We consider that this is not realistic and most probably our procedure to estimate the FWHM of the PSF in the datacubes is not reliable for values near to the spaxel size (0.5") due to the limitations of sampling in the estimation of the FWHM. An additional problem is that it is not feasible to estimate the FWHM in the cubes below the PSF size of the reference PS image that we use to compare with (i.e., $\sim 1.1''$ in average). To estimate the accuracy of our estimations of the FWHMs based on the PSF-matching described in Sec. 2.2.5, we followed García-Benito et al. (2015) and Sánchez et al. (2016b), and explored the FWHM in the field-stars. For doing so we selected the foreground stars included in the Gaia DR3 adopted for the masking described in Sec. 2.2.7. We applied an additional cut, selecting only those stars brighter than $g < 18$ mag, and at a distance larger than 15" from the center of the galaxies to minimize the possible contamination from this source. We end up with 91 field stars. We extracted a post-stamp image of $\sim 10'' \times 10''$ size from the new g -band image reconstructed from the new (v2.3) and old (v2.2) datacubes, deriving their FWHM by fitting a Gaussian function. The average FWHM derived from field-stars is $1.43 \pm 0.40''$ ($2.62'' \pm 0.58''$) that agrees with the value derived based on the PSF-matching procedure, $1.51'' \pm 0.32''$ ($2.64'' \pm 0.56''$) for the v2.3 (v2.2) reduced data. Once determined the accuracy of our procedure it is evident that Fig. 6, illustrates clearly the improvement in the spatial resolution of the data introduced by the new reduction. Even considering that we may be underestimating the FWHM of the PSF at low values, we can claim that the new datacubes have a typical spatial resolution of ~ 1.0 - $1.5''$ in most of the cases.

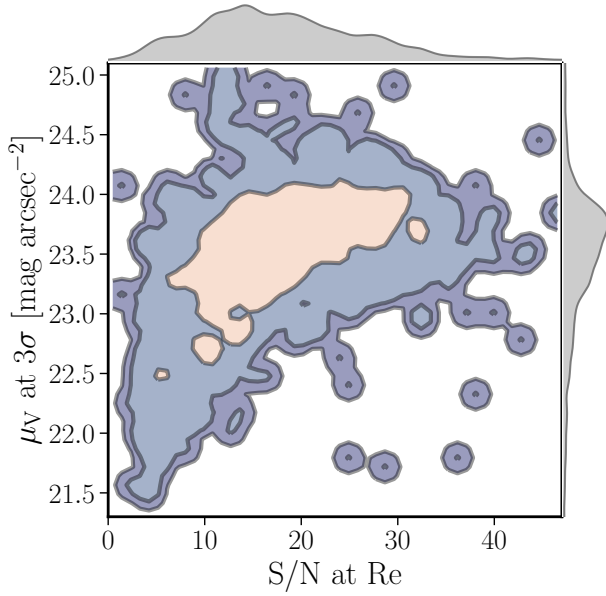


Figure 5. Surface-brightness at 3σ detection limit as a function of the S/N at the effective radius in the final good quality datacubes. Each successive contour corresponds to a density distribution containing a 99%, 95% and 65% of the total sample. The kernel density distribution of both quantities is included in the top and right subpanels.

A more qualitative method to gauge the improvement in the image quality and in particular in the resolution achieved by the new reduction is to compare the images obtained by photometric observations with those synthesized from datacubes provided by the new and the previous data reductions. Figure 7 shows this comparison for three selected datacubes, corresponding to galaxies NGC 5947, NGC 5936 and ARP 118. It comprises the true color images created using the u -, g - and r -band images retrieved from the SDSS survey and synthesized from the datacubes of the current and the previous reduction. A simple visual inspection of the three images demonstrates that the resolution achieved by the new reduction is of the same order of the one achieved by a photometric observation (i.e., natural seeing), with an evident improvement with respect to the previous version. We should note that, as shown in Fig. 6, the final resolution depends on the seeing during the observation, and therefore not all datacubes present the same image quality. Beside the improvement in the resolution, other improvements introduced by the new reduction, including the re-evaluation of the real location of the dithered pointings and the masking and interpolation of the broken fibers, are also appreciated in Fig. 7 (e.g., in the case of images corresponding to NGC 5936).

3 GALAXY SAMPLE

We describe in this section the main properties of the compiled sample, illustrating that indeed it can be used as representative sample of the galaxies in its redshift footprint, despite of its heterogeneous nature. The original CALIFA sample was primarily selected based on the diameter of the galaxies in the sky (Walcher et al. 2014). This selection was adopted to match their optical extension to the FoV of the PPAK science bundle ($\sim 70''$). Additional restrictions were introduced in that selection to focus the sample in the nearby Universe ($z \sim 0.015$), but far enough to be out of the local cosmological bubble dominated by the cosmic variance (>20 Mpc). Finally a cut in

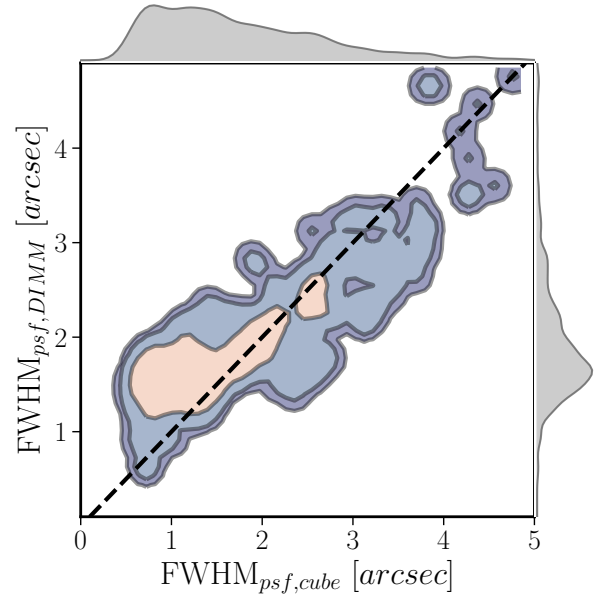


Figure 6. Comparison between the FWHM of the natural seeing measured by the Calar Alto DIMM within a one hour range the observation and the FWHM of the PSF estimated on each cube as part of the new reduction scheme, as described in the text. Each successive contour corresponds to a density distribution containing a 99%, 95% and 65% of the total sample. The kernel density distribution of both quantities is included in the top and right subpanels.

the apparent magnitude of the targets was introduced to explicitly exclude dwarf galaxies that would in other case dominate the number statistics. This essentially defined the CALIFA mother sample (MS Sánchez et al. 2012; Walcher et al. 2014). These criteria were relaxed to introduce galaxy types underrepresented in the MS, such as cluster members, large ellipticals, dwarf galaxies, companions of galaxies in interacting systems covered by the survey, and supernova host galaxies (compiled by the PISCO, PMAS/PPak Integral-field Supernova Hosts Compilation survey Galbany et al. 2018). All those galaxies comprise the CALIFA extended sample (ES), described in 3rd data release (Sánchez et al. 2016b). In this previous data release it was distributed 646 datacubes corresponding to individual galaxies observed using the V500 configuration, 529 of them extracted from the MS and 117 to the ES. The current eCALIFA compilation comprises 895 individual galaxies, 519 corresponding to the original CALIFA MS and 376 more to the ES.

Figure 8 shows the distribution of galaxies from the eCALIFA sample in the sky compared to that of the SDSS galaxies extracted from the NASA Sloan Atlas (SDSS-NSA Blanton et al. 2017). The SDSS-NSA is one of the largest and more complete catalog of galaxy parameters in the local universe, comprising $\sim 150,000$ objects. Being a volume/apparent magnitude selected sample it can be volume corrected and it is frequently used to explore the general properties of galaxy population at low- z (e.g. Sánchez et al. 2019a). Indeed, the full redshift range covered by the eCALIFA sample ($0.0005 < z < 0.08$) match pretty well with the one covered by the SDSS-NSA catalog (99.8% of the galaxies included in this redshift range). We should note that the redshift distribution of the eCALIFA sample is not homogeneous, with a better coverage below $z < 0.03$, where 94% of the objects is found. Fig 8 shows that the imprint of the eCALIFA sample in the sky is slightly wider than that of the SDSS-NSA, being both restricted essentially to the north hemisphere. For the region in common it is evident that the final sample cover a wide

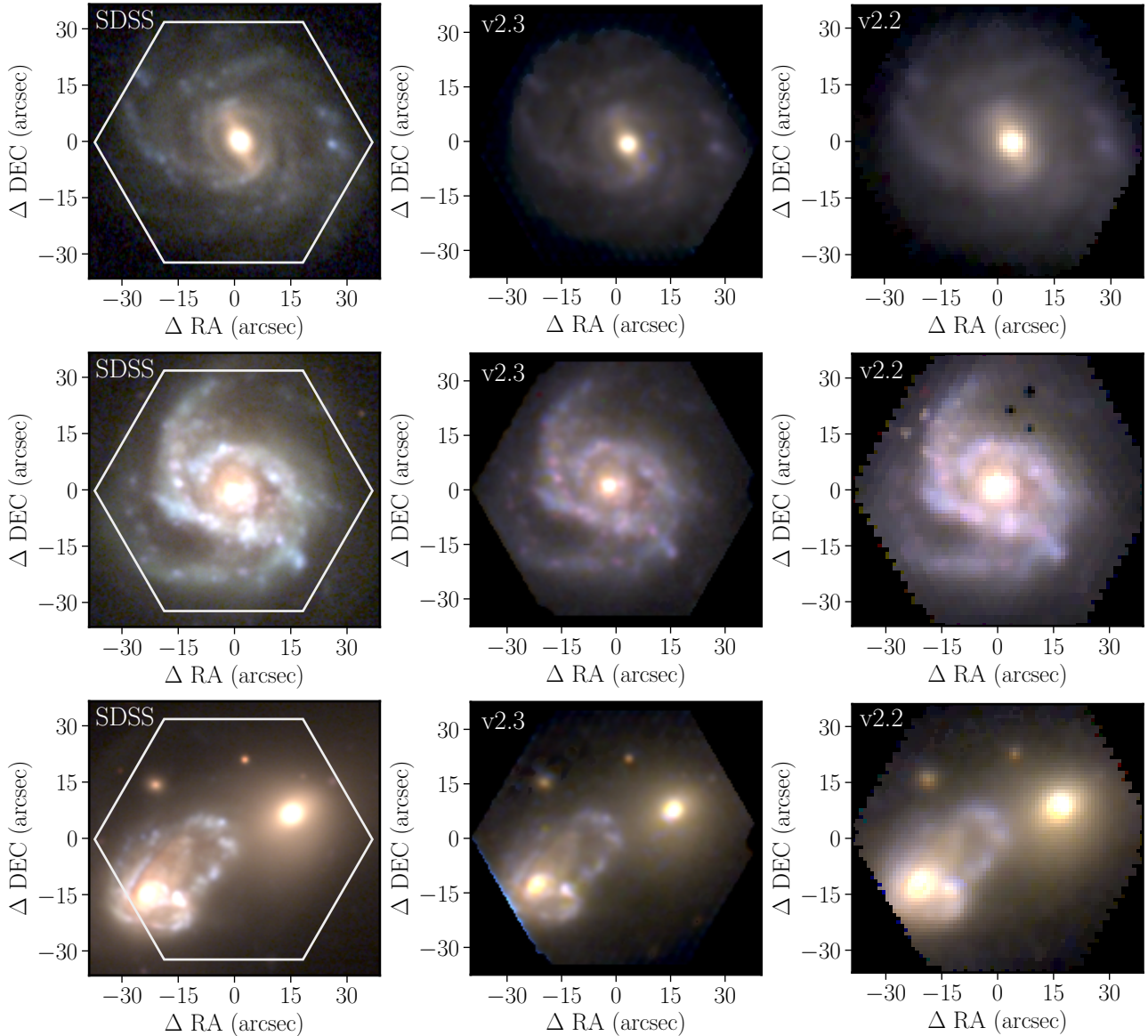


Figure 7. Selected examples to illustrate the improvements in the image quality introduced by the new reduction procedure for three different galaxies: (i) the archetype galaxy shown along this study, NGC 5947 (top panels); (ii) a face-on spiral image with clear issues in the cube reconstruction in the previous reduction of the data, NGC 5936 (middle panels); and (iii) a merging system, ARP 118, observed during a period of extremely good seeing, $\sim 0.5''$ (bottom panels). From left to right each panel shows the true color image generated using the u -, g - and r -band images extracted from the SDSS survey (left panel), synthesized from the datacubes corresponding to the new reduction (central panel) and produced by the previous version of the data reduction (right panel). Note that there are some color differences due to the truncation of the u - (and r -band) synthesized image introduced by the wavelength range covered by the IFS data. Despite of them the improvement in the image quality is clearly appreciated in the central panels. Similar plots for the full dataset are included in the distribution webpage: <http://ifs.astroscu.unam.mx/CALIFA/V500/v2.3/>

range of galaxy densities in the sky, traced by the darkest regions in the SDSS-NSA distribution.

Like in the case of the MS sample, the eCALIFA sample was primarily selected by diameter, traced by the effective radius. We selected objects which most of its optical extension is covered by the FoV of the IFS data and they are well resolved by the observations. Indeed, 90% of the sample is restricted to an Re between $4''$ ($Re > \text{fiber-size}$) and $24''$ ($\text{FoV} > 2 Re$). In addition, we do not cover very faint objects. There is no galaxy fainter than $r > 18.5$ mag in the sample, and $\sim 95\%$ of the objects are restricted to a r -band magnitude range between 11 and 15 mag. If this compilation is representative of the population in the nearby universe it must have similar

properties of that of a sample selected using similar cuts in diameter and magnitude. To explore this we select a sub-sample of the SDSS-NSA catalog imposing an effective radius ($4'' < Re < 24''$) and r -band magnitude cut ($r < 18$ mag), comprising $\sim 45,000$ galaxies (NSA| Re_{lim} sample hereafter).

Figure 9 shows the distribution of $g - r$ color as a function of the r -band absolute magnitude (i.e., the color-magnitude diagram, CMD) for the eCALIFA sample compared to the same distribution for the NSA| Re_{lim} sub-sample. Like in the case of the CALIFA sample the new compilation has a pretty good coverage of the CMD, with a reasonable sampling of galaxies in the red-sequence (mostly early-type and massive), the blue cloud (mostly late-type and less

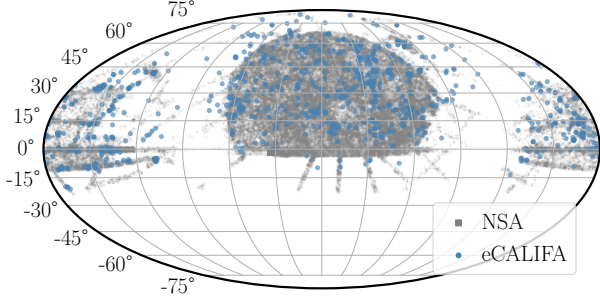


Figure 8. Distribution of the eCALIFA galaxies in the sky (blue-solid circles) together with the distribution for the SDSS-NSA galaxies (grey-solid squares) at a similar redshift range. The galaxies from the current IFS compilation are essentially distributed in the north hemisphere, with a large fraction in them in the same sky foot-print as the SDSS galaxies. Comparing both distributions we appreciate that the eCALIFA galaxies sample objects in different densities.

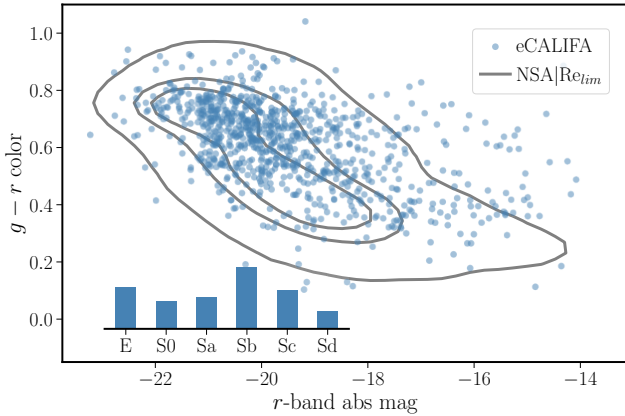


Figure 9. Distribution in the $g-r$ vs. r -band absolute magnitude diagram of the eCALIFA galaxies (blue-solid circles), compared to the same distribution for sub-sample of SDSS-NSA galaxies selected using the same diameter, magnitude and redshift range as the eCALIFA compilation (grey contours). Each successive contour encircles a 95%, 65% and 40% of the SDSS-NSA galaxies. The bottom-left inset shows the morphological distribution of the eCALIFA galaxies.

massive), and the green-valley (intermediate morphological type and mass ones). There is a rough agreement between the distributions traced by both samples, despite the fact that a KS-test suggest that there is significant difference between them. Actually, a 92% of the eCALIFA galaxies are indeed encircled by the lowest density contour tracing the distribution of the NSA| Re_{lim} sub-sample (comprising to 95% of these objects). Some evident differences are (i) the tail towards redder galaxies in the fainter regime of the distribution, all out of the 95% contour. These galaxies belongs to a low-luminosity sub-set of SNIa hosts included in the PISCO sample; and (ii) the less defined green-valley appreciated in the eCALIFA sample. This later difference may indicate an excess of intermediate type galaxies, something that has been already noticed for the CALIFA sample (e.g. Lacerda et al. 2020). Indeed, the morphological distribution, shown in the inset of Fig. 9 illustrate both the wide coverage of morphological types of the sample, and the clear peak in Sb (early spiral) galaxies.

Figure 10, left panels, shows similar comparisons between both samples for the r -band absolute magnitude and Re (in physical

units) as function of the redshift. Like in the case of the CMD, there is a fair agreement between the distributions described by both samples, in particular in the redshift regime better covered by the eCALIFA sample ($z < 0.03$, as indicated before). At redshift $z > 0.03$ the eCALIFA sample is clearly incomplete, as illustrated by the comparison with the NSA| Re_{lim} distributions. It is worth noticing that this was the limiting redshift of the original CALIFA MS. Despite of these differences in the coverage of the absolute magnitude and effective radius with redshift, the distribution of one parameter as a function of the other is pretty similar for both samples (left panel of Fig. 10). Indeed, $\sim 90\%$ of the eCALIFA galaxies are encircled by the lowest density contour of the NSA| Re_{lim} sample shown in this figure, comprising 95% of these objects.

3.1 Volumen correction

All these comparisons indicate that indeed the eCALIFA behaves, at a first order, as a diameter-selected sample at the same redshift range extracted from a luminosity limited sample (i.e., the NSA| Re_{lim} sub-sample). If this is the case, this sample could be representative of the nearby universe when applying the proper volume correction. Following Walcher et al. (2014), we derive the available volume per galaxy using the V_{max} method described by Schmidt (1968). de Jong & van der Kruit (1994) adopted this method, deriving the equation of the accessible volume for a galaxy selected within a range of isophotal sizes (projected diameters). Considering Re as a tracer of the diameter of a galaxy, the same equation can be adopted to derive the accessible volume for a given limiting effective radius:

$$V_{lim}(z, Re) = 4\pi \frac{D_L(z)}{(1+z)^2} \left(\frac{Re}{Re_{lim}} \right)^3 \quad (3)$$

where $D_L(z)$ is the luminosity distance at redshift z and Re_{lim} is the largest limiting effective radius adopted in the selection criteria (defined by the FoV of the IFU, in our case). To estimate the luminosity distance at a given redshift we assume a pure Hubble flow distance and the cosmology assumed along this exploration. This is a good approximation for the average redshift of the considered samples ($z \sim 0.015$). However, it may introduce considerable errors for the lowest redshift objects, where the average galaxy velocity with respect to the cosmic web is of the same order of the bulk velocity due to the cosmic expansion ($z < 0.001$). Fortunately we have just 2 objects below this limit (NGC 6789 and NGC 0784).

The inverse of V_{lim} is the weight of each galaxy in any estimated global property (e.g. the star-formation or mass density in the considered volume) or distribution (e.g., the luminosity or the mass function). When selecting galaxies within a range of effective radius, from Re_{min} to Re_{max} , the corresponding weight (ω) is derived as the difference between the inverse of the corresponding V_{min} and V_{max} , and estimated using Eq. 3. This indeed defines an equivalent accessible volume that is estimated by the equation:

$$\frac{1}{V_{cor}} = \omega = \frac{1}{V_{max}} - \frac{1}{V_{min}} \quad (4)$$

Note that V_{cor} , the equivalent volume correction depends not only on the redshift and Re of the object, but also on the minimum and maximum Re adopted in the selection of the sample. Finally, a correction must be applied if the accessible solid angle for the sample is smaller than the full sky, which involves a global scaling factor. Further corrections can be applied to take into account other limiting factors, just as the flux-limit introduced by a limiting magnitude.

We acknowledge that this derivation relies on multiple simplifications and assumptions that have been broadly discussed in previous studies, in particular in Walcher et al. (2014). However, despite of

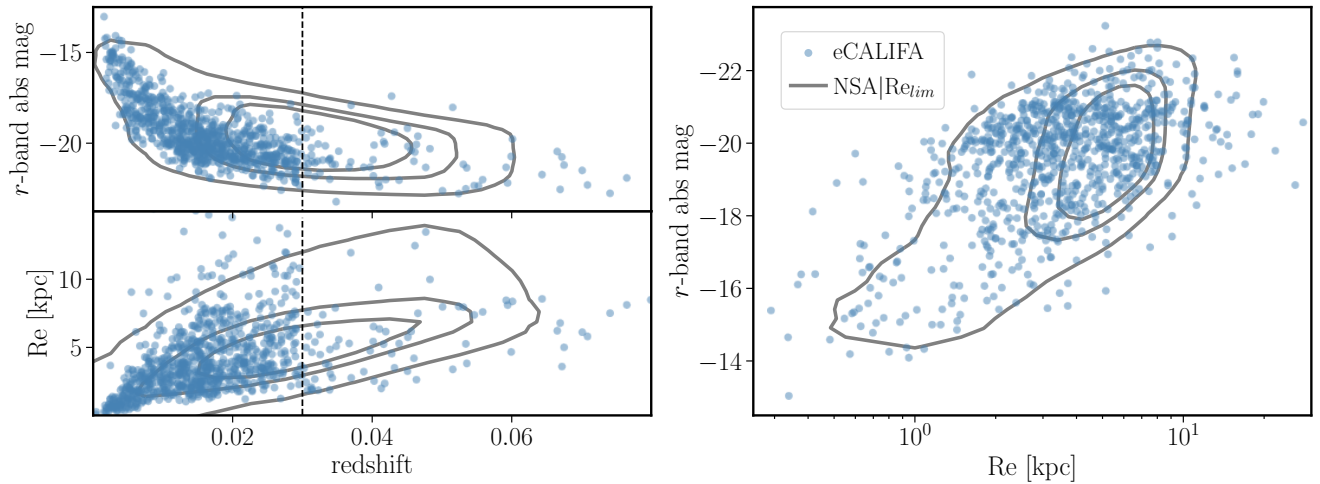


Figure 10. Distribution of r -band absolute magnitude (top-left panel) and effective radius in kpc (bottom-left panel) as a function of the redshift, and one as a function of the other (right panel), for the galaxies in the eCALIFA compilation (solid-blue circles). For comparison purposes grey-contours show, in each diagram, the distribution of the SDSS-NSA galaxies using the same diameter, magnitude and redshift range as the eCALIFA galaxies. Each successive contour encircles a 95%, 65% and 40% of the SDSS-NSA galaxies. Dashed line in the left panels indicate the $z = 0.03$ limit above which we consider that the eCALIFA sample lose completeness.

Table 3. Observational properties of the galaxy sample*

ID	cubename	galaxy	RA deg	DEC deg	z	type	$M_{abs,r}$ mag	$g-r$ mag	Re "	PA deg	ϵ	V_{cor} Mpc^3
1	IC5376	IC5376	0.3325	34.5265	0.01645	Sb	-19.81	0.73	9.95	-86.1	0.97	3250155.2
2	UGC00005	UGC00005	0.7733	-1.9129	0.02405	Sbc	-20.68	0.56	14.61	-43.9	0.86	2008811.2
3	NGC7819	NGC7819	1.1018	31.4725	0.01634	Sc	-19.42	0.47	19.3	4.3	0.85	1352577.3
4	UGC00029	UGC00029	1.1403	28.3022	0.0293	E1	-20.98	0.7	5.57	85.1	0.53	41513.4
5	IC1528	IC1528	1.2724	-7.0925	0.01261	Sbc	-18.41	0.52	23.34	-16.1	0.91	2563246.9
6	NGC7824	NGC7824	1.2754	6.9209	0.02024	Sab	-21.06	0.62	7.29	65.4	0.74	66001.7
7	UGC00036	UGC00036	1.3078	6.7728	0.02075	Sab	-20.88	0.67	7.03	-71.8	0.87	165870.3
8	NGC0001	NGC0001	1.816	27.7085	0.01473	Sbc	-20.38	0.66	8.08	5.1	0.74	34274.9
9	NGC0023	NGC0023	2.4726	25.9244	0.01482	Sb	-20.98	0.6	29.66	63.2	0.77	2017008.3
10	NGC0036	NGC0036	2.8426	6.3899	0.01978	Sb	-21.09	0.66	18.18	-69.0	0.82	1565578.4

Subset of the properties of the galaxy sample: (1) CALIFA ID (Sánchez et al. 2016b); (2) IFS cube name; (3) galaxy name, (4) right ascension; (5) declination; (6) redshift; (7) Hubble type; (8) r -band absolute magnitude; (9) $g-r$ color; (10) effective radius; (11) position angle; (12) eccentricity; and (13) equivalent volume accessible for the considered target.

*We present just ten galaxies, the remaining ones are presented electronically.

them, the approach is valid. To demonstrate it so, we have first applied it to the NSA|Re_{lim} sub-sample, a sample selected imposing a well defined range of redshifts, magnitudes and in particular effective radius over a large and well defined catalog of galaxies. Based on this volume corrections we estimate the mass-function, using the stellar masses provided by the SDSS-NSA catalog (Blanton et al. 2017), shifted by a constant to correct for the difference cosmology and to match the Salpeter (1955) initial mass function (IMF). Figure 11 shows the resulting mass-function compared to the one derived for the full SDSS-NSA catalog (Fig. 17 of Sánchez et al. 2022b). There is a good agreement between the two mass-functions in the regime of masses in common, validating the adopted volume correction. Based on this result we estimate the volume correction using this approach for the eCALIFA sample and repeat the estimation of the mass-function. For doing so we estimate the stellar mass from the g - and r -band photometric data obtained from the segmented PS images described during the isophotal analysis (Sec. 2.3), implementing the relation between the mass-to-light (Y_*) and the $g-r$

colors published by (Bell & de Jong 2000) for the same IMF. We refer to this stellar mass as $M_{*,phot}$ hereafter. The result of this analysis is included in Fig. 11. Like in the case of the NSA|Re_{lim} sub-sample, the mass function estimated for the eCALIFA sample follows pretty well the know distribution described by the full NSA-SDSS catalog, for the range of stellar masses in common. The strongest deviations are found at (i) $\sim 10^{10}M_{\odot}$, where the eCALIFA sample seems to present a slight excess of galaxies, and (ii) at $>10^{11.5}M_{\odot}$, where the eCALIFA sample (and maybe the NSA|Re_{lim} sub-sample), present a slight defect of galaxies. The excess of galaxies at $\sim 10^{10}M_{\odot}$ could be due to the local fluctuations in the galaxy density in this mass regime, already noticed in Walcher et al. (2014). In addition we note that for the stellar masses below $10^{8.5}M_{\odot}$, not sampled by the published NSA-SDSS mass function, the agreement between the two mass functions derived using the described volume correction is reasonable good.

Based on all the results described along this section we can fairly claim that the eCALIFA sample, once corrected by the proper vol-

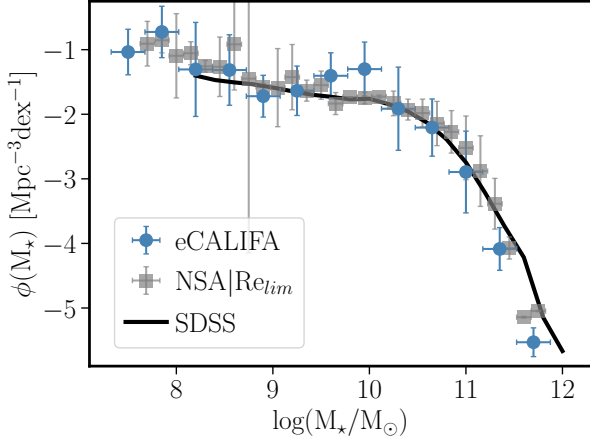


Figure 11. Mass function estimated for the eCALIFA compilation (blue solid circles) assuming that it behaves as a diameter selected sample. Error bars illustrate the width of the mass bins (x-axis) and the error propagation based on a Monte-Carlo iteration for all parameters involved in the derivation of Volume correction (see the text). For comparison purposes we include (i) the same estimation for the NSA-SDSS sub-sample selected adopting the same diameter, magnitude and redshift range as the eCALIFA galaxies (grey solid squares) and (ii) the mass-function derived using the full SDSS-NSA catalog (Blanton et al. 2017), already published in Sánchez et al. (2022b). There is a considerably good agreement between the three mass functions, despite the differences between the three samples.

ume coverage, can be adopted as a representative sample of galaxies in the covered redshift range (i.e., the nearby Universe). Table 3 presents the main observational properties of the galaxies discussed along this section.

4 ANALYSIS

We perform a set of analyses in order to extract the main spectroscopic properties of the studied galaxies and to evaluate quality and usability of the new reduced dataset. In particular we explore the spectra extracted in two different apertures for each galaxy: (i) a circular aperture of $1.5''$ /diameter located at the center; and (ii) the integrated spectra, obtained by co-adding all the spectra within the IFS datacube corresponding to the spaxels with a $S/N > 3$ at 5500\AA . The first of those spectra would allow us to characterize the spectroscopic properties of both the stellar populations and the ionized gas in the inner regions of the galaxies, at scales of ~ 500 pc, making use of the improvement in the spatial resolution introduced by the new reduction. The inner regions are particularly interesting as they are the locations where AGN activity, galactic winds, and the effect of star-formation quenching are more frequently observed. On the other hand, the integrated spectra would allow to characterize extensive quantities (such as the integrated stellar mass and integrated star-formation rate), the dominant ionizing source and/or the star-formation stage.

4.1 Spectral fitting

We analyze each individual spectrum using `PYFIT3D` (Sánchez et al. 2016a; Lacerda et al. 2022) to derive the main properties of stellar populations and ionized gas components. For doing so, the code generates a model of the stellar population spectrum based on the linear

combination of a set of single stellar populations (SSP) included in a given library. This model is convolved by a Gaussian function to take into account the velocity dispersion (σ_*) and shifted according to the systemic velocity (v_*). In addition, the multi-SSP model is attenuated adopting a given extinction curve (Cardelli et al. 1989a, , in this particular implementation), and a certain dust attenuation value in the V -band ($A_{V,*}$). These three non-linear parameters are derived by `PYFIT3D` based on a brute exploration of the space of parameters, adopting a limited version of the SSP-library, prior to the fit with the full library, that we describe later on.

The treatment of the emission lines is done by a two steps procedure. First, the wavelength location of the emission lines is masked out and a preliminar model of the stellar population is created. This model is then subtracted to the original spectrum. The resulting residual spectrum comprises just the emission lines (plus noise and imperfections associated to the modelling of the stellar population). Then, each emission line of a defined set ($[\text{O II}]3727$, $\text{H}\delta$, $\text{H}\gamma$, $\text{H}\beta$, $[\text{O III}]4959,5007$, $\text{H}\alpha$, $[\text{N II}]6548,84$ and $[\text{S II}]6717,31$, in this particular case) is modelled using a single Gaussian function, deriving the flux intensity, velocity and velocity dispersion. The combined model for all the emission lines is subtracted to the original spectrum. This final spectrum, comprising just the stellar population component (plus noise and imperfections associated to the modelling of the emission lines), is fitted using the full SSP library (shifted, convolved and dust attenuated). Finally, a Monte-Carlo iteration is adopted to estimate the errors for each derived parameter. The procedure has demonstrated to produce reliable results, being contrasted against ad-hoc created simulations and mock galaxy spectra generated from hydrodynamical simulations (e.g., Sánchez et al. 2016a; Lacerda et al. 2022; Ibarra-Medel et al. 2019; Sarmiento et al. 2022). Indeed, it has been adopted by previous several studies, in particular focused on the analysis of IFS data (e.g. Cano-Díaz et al. 2016; Sánchez et al. 2018, 2022b).

Figure 12 shows an example of the fitting procedure, corresponding to the analysis of the integrated spectrum of the archetype galaxy NGC 5947. It illustrates how well the observed spectrum is reproduced by the best-fitted model for both the stellar population and emission line models. The typical level and shape of the residuals is appreciated, with the location of the strong night-sky emission lines easily identified (e.g., at 5577\AA or beyond 7200\AA , Sánchez et al. 2007). The distribution by age and metallicity of the individual weight ($w_{ssp,*L}$) of each SSP in the final model (i.e., the fraction of light in the V -band), is also included in the figure. In the current analysis we adopt the `MASTAR_SLOG` SSP library, generated by an updated version the Bruzual & Charlot (2003) stellar population synthesis code (described in Appendix A of Sánchez et al. 2022b), using the MaStar stellar library Yan et al. (2019). The `MASTAR_SLOG` library comprises 273 SSP templates, covering 39 ages (from 1 Myr to 13.5 Gyr), in a pseudo-logarithmic sampling, and 7 metallicities ($Z/Z_\odot = 0.006, 0.029, 0.118, 0.471, 1, 1.764, 2.353$). A solar α -enhancement is considered for all SSPs in the adopted library (i.e., $[\alpha/\text{Fe}] = 0$). This library was recently adopted to analyze the last data-release of the MaNGA (Bundy et al. 2015) IFS galaxy survey (Sánchez et al. 2022b), and therefore, by adopting it the results can be more easily compared with.

4.2 Stellar parameters derived by the spectral fitting

As discussed in detail in previous studies (e.g. Sánchez et al. 2021a, 2022b), the weights or coefficients of the decomposition can be used (i) to derive the luminosity- and mass-weighted parameters of the

Table 4. Stellar population properties derived by `pyFIT3D` for both the central and integrated spectra of each galaxy.

cubename	aperture	$\mathcal{A}_{*,L}$ Gyr	$\mathcal{Z}_{*,L}$ f_{mass}	$\mathcal{A}_{*,M}$ Gyr	$\mathcal{Z}_{*,M}$ f_{mass}	$A_{V,*}$ mag	σ_* km s ⁻¹	$\log(\Upsilon_*)$ M _⊙ /L _⊙	$\log(M_*)$ M _⊙
IC5376	int	3.2659 ± 0.4899	0.0138 ± 0.0021	5.1993 ± 0.7799	0.0088 ± 0.0013	0.4 ± 0.1	128.4 ± 19.3	0.76	10.07
"	cen	6.8726 ± 1.0309	0.0172 ± 0.0026	7.6401 ± 1.146	0.0168 ± 0.0025	0.5 ± 0.1	130.0 ± 19.5	1.05	9.32
UGC00005	int	0.8419 ± 0.1263	0.0161 ± 0.0024	3.0662 ± 0.4599	0.019 ± 0.0028	0.4 ± 0.1	287.8 ± 43.2	0.53	10.47
"	cen	2.7528 ± 0.4129	0.0169 ± 0.0025	5.2094 ± 0.7814	0.0167 ± 0.0025	0.7 ± 0.1	62.6 ± 9.4	0.83	8.99
NGC7819	int	0.695 ± 0.1042	0.0093 ± 0.0014	4.9267 ± 0.739	0.0043 ± 0.0006	0.3 ± 0.0	29.9 ± 4.5	0.47	9.81
"	cen	0.3353 ± 0.0503	0.0037 ± 0.0006	4.2694 ± 0.6404	0.0125 ± 0.0019	0.6 ± 0.1	398.5 ± 59.8	0.57	8.56
UGC00029	int	7.7201 ± 1.158	0.0191 ± 0.0029	8.7365 ± 1.3105	0.0205 ± 0.0031	0.0 ± 0.0	183.1 ± 27.5	1.12	11.01
"	cen	5.2782 ± 0.7917	0.029 ± 0.0044	6.146 ± 0.9219	0.0292 ± 0.0044	0.6 ± 0.1	207.4 ± 31.1	1.02	9.52
IC1528	int	0.9597 ± 0.144	0.0043 ± 0.0006	3.3443 ± 0.5016	0.0112 ± 0.0017	0.2 ± 0.0	242.9 ± 36.4	0.48	9.68
"	cen	0.8211 ± 0.1232	0.016 ± 0.0024	5.0834 ± 0.7625	0.0139 ± 0.0021	0.6 ± 0.1	102.8 ± 15.4	0.65	8.05
NGC7824	int	2.7376 ± 0.4106	0.0235 ± 0.0035	2.9638 ± 0.4446	0.029 ± 0.0044	0.0 ± 0.0	157.5 ± 23.6	0.74	10.66
"	cen	2.4005 ± 0.3601	0.0258 ± 0.0039	2.8525 ± 0.4279	0.0262 ± 0.0039	0.0 ± 0.0	110.0 ± 16.5	0.68	8.72
UGC00036	int	2.5892 ± 0.3884	0.0254 ± 0.0038	7.646 ± 1.1469	0.0283 ± 0.0042	0.3 ± 0.0	288.8 ± 43.3	0.94	10.59
"	cen	5.6372 ± 0.8456	0.0293 ± 0.0044	6.5388 ± 0.9808	0.035 ± 0.0052	0.6 ± 0.1	307.2 ± 46.1	1.09	9.49
NGC0001	int	1.2922 ± 0.1938	0.0159 ± 0.0024	3.4601 ± 0.519	0.0149 ± 0.0022	0.5 ± 0.1	180.4 ± 27.1	0.63	10.16
"	cen	2.1775 ± 0.3266	0.0288 ± 0.0043	3.6797 ± 0.552	0.0275 ± 0.0041	0.4 ± 0.1	141.6 ± 21.2	0.75	9.08
NGC0023	int	0.7246 ± 0.1087	0.01 ± 0.0015	4.4113 ± 0.6617	0.0288 ± 0.0043	0.5 ± 0.1	151.1 ± 22.7	0.67	10.57
"	cen	0.9247 ± 0.1387	0.0202 ± 0.003	4.5153 ± 0.6773	0.0325 ± 0.0049	0.6 ± 0.1	360.0 ± 54.0	0.72	9.36
NGC0036	int	3.2041 ± 0.4806	0.019 ± 0.0028	10.26 ± 1.539	0.0282 ± 0.0042	0.2 ± 0.0	96.9 ± 14.5	1.02	11.05
"	cen	3.2059 ± 0.4809	0.0395 ± 0.0059	3.7183 ± 0.5577	0.0394 ± 0.0059	0.3 ± 0.0	178.4 ± 26.8	0.86	9.32
UGC00139	int	0.1775 ± 0.0266	0.0031 ± 0.0005	4.4885 ± 0.6733	0.0065 ± 0.001	0.6 ± 0.1	37.4 ± 5.6	0.35	9.32
"	cen	1.5945 ± 0.2392	0.0171 ± 0.0026	2.9027 ± 0.4354	0.0181 ± 0.0027	0.2 ± 0.0	159.5 ± 23.9	0.6	7.88
MCG-02-02-030	int	3.1502 ± 0.4725	0.0065 ± 0.001	8.8252 ± 1.3238	0.0044 ± 0.0007	0.1 ± 0.0	161.5 ± 24.2	0.85	10.13
"	cen	0.5685 ± 0.0853	0.0112 ± 0.0017	9.3588 ± 1.4038	0.0158 ± 0.0024	1.3 ± 0.2	309.3 ± 46.4	0.96	8.48

We present the values for just ten galaxies. The information for the remaining one is distributed electronically.

errors estimated for the emission lines. However, for the reasons outlined before this error is most probably just a lower-limit to the real one, that, including systematic effects would be at least ~ 0.15 mag in the best case (according to the typical uncertain in the measurement of emission lines with the adopted technique [Lacerda et al. 2022](#)). We consider that all values of $A_{V,gas}$ below this error limit, corresponding to $H\alpha/H\beta < 3$ or derived from $H\alpha$ or $H\beta$ fluxes below with a $S/N < 2$, are ill defined. All of them corresponds to weak emission lines and low values of the dust attenuation. We have substituted them by a value of 0.15 mag and set the corresponding errors to zero to indicate that they are just upper limits.

4.4 Star-formation rate

The star-formation rate (SFR) for both apertures is derived from the dust-corrected $H\alpha$ luminosity using the formulae: $L_{H\alpha} = 4\pi D_L(z)^2 f_{H\alpha} 10^{0.4A_{V,gas}}$, where $f_{H\alpha}$ is the $H\alpha$ flux intensity derived from the spectral fitting procedure described before (Sec. 4.1), $A_{V,gas}$ is the dust attenuation described in the previous section, and $D_L(z)$ is the luminosity distance corresponding to the redshift (z) of the object. Finally, we use the calibrator derived by [Kennicutt et al. \(1989\)](#), $SFR = 8 \cdot 10^{42} L_{H\alpha}$, valid for a ([Salpeter 1955](#)) IMF. Errors of the quantities involved in this calculation are propagated through the different equations to estimate the corresponding SFR error.

We have estimated the SFR from $H\alpha$ irrespectively of the dominant ionizing source (that we will discuss later on, Sec. 5.2.1), following previous studies [Cano-Díaz et al. \(2016\)](#); [Sánchez et al. \(2018, 2022b\)](#). In purity, only in the case that the gas is ionized by young massive OB-stars is valid this approximation. However, as noted in those articles, when other ionizing sources contribute to the

$H\alpha$ luminosity the estimated SFR is just an upper-limit to the real one, and this is how it should be interpreted.

4.5 Molecular gas mass

The molecular gas mass is estimated for the two aperture spectra based on a dust-to-gas calibrator, following the approach proposed by ([Brinchmann et al. 2013](#)). The particular calibrator adopted in here is based on the comparison of the molecular gas mass density obtained from CO observations ([Bolatto et al. 2017](#)) and the ionized-gas dust attenuation for the EDGE-CALIFA sample presented in [Barrera-Ballesteros et al. \(2020\)](#), recently improved by [Barrera-Ballesteros et al. \(2021a\)](#). The estimations based on this approach have been proved to provide reliable estimations of the molecular gas densities (and integrated molecular gas) within ~ 0.15 dex when comparing with both spatial resolved and single aperture derivations based on CO observations ([Colombo et al. 2020](#); [Barrera-Ballesteros et al. 2021b](#); [Sánchez et al. 2021a,b](#)). The calibrator provides the molecular gas density (Σ_{gas}) from the dust attenuation ($A_{V,gas}$, Sec. 4.3), for each aperture of each galaxy. From this surface density we estimate the integrated molecular gas (M_{gas}) by multiply by equivalent area, following [Sánchez et al. \(2021a,b\)](#), i.e., $4\pi R_e^2$, where R_e is the effective radius (Sec. 2.3). When an upper-limit was adopted for the dust attenuation, the estimated molecular gas should be considered as an upper-limit as well. In those cases the estimated error resulting from the propagation of the $A_{V,gas}$ value is set to zero.

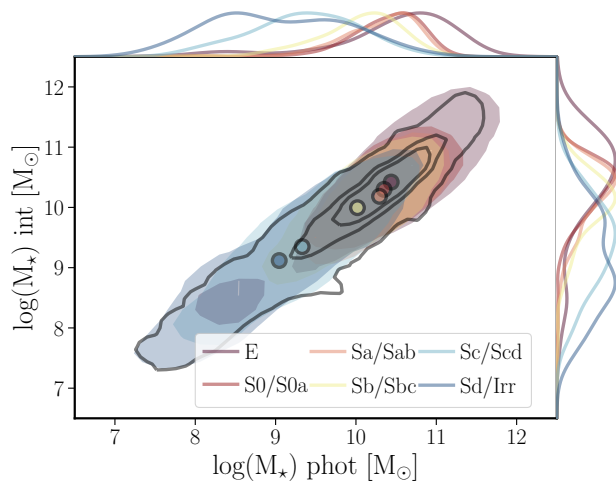


Figure 13. Comparison between the stellar masses derived using the PS photometry (*phot*), described in Sec. 3.1, and those obtained using `PFIT3D` for the integrated spectra (*int*). Black-solid contours show the density distribution, with each successive one encircling a 95%, 65% and 40% of the galaxies, respectively. Each shaded region corresponds to the area encircling a 85% of the galaxies of a particular morphological type, represented by a different color (inset legend). The normalized density distributions of both parameters, also segregated by morphology, are shown in the upper- and right-side panels, with the mean values represented as solid circles, both using the same color code.

4.6 Oxygen abundance

The analyzed spectra have not the required spectral resolution and depth to derive the oxygen abundance (O/H) using the direct method, even less to estimate the abundances using recombination lines (see Peimbert & Peimbert 2006; Bresolin 2017, to gauge the characteristics of the data required to apply those methods). In the case of CALIFA data, the direct method was applicable for a small fraction of the galaxies and at particular star-forming regions (Marino et al. 2013). Thus, we make use of strong emission line calibrators that provides with an estimation to the oxygen valid to explore the global and local trends in galaxies to the spatial resolution of our data (Sánchez 2020). As we do not intend to make a detailed study of the systematic differences between different calibrators depending on their nature (López-Sánchez et al. 2012), we focus on two calibrators instead of estimating the oxygen abundance using a set of them (e.g., like in the case of Sánchez et al. 2022b; Alvarez-Hurtado et al. 2022). We estimate O/H using the calibrators proposed by Marino et al. (2013), that have derived empirically as a linear relation between the oxygen abundances estimated using the direct method for a compiled sample of H II regions and the logarithm of $[\text{N II}]/\text{H}\alpha$ and $([\text{O III}]/\text{H}\beta)/([\text{N II}]/\text{H}\alpha)$ line ratios, N2 and O3N2 respectively. Due to their nature these calibrators should be applied when the dominant ionizing source is due to young/massive OB stars. Therefore, we derive O/H for those spectra compatible with this kind of ionization (as selection discussed later one, in Sec. 5.2.1). We acknowledge that any contamination by other ionizing sources may introduce systematic effects in the derivation of the oxygen abundance that are (somehow) mitigated when using the spatial resolved information included in our delivered data (e.g. Mast et al. 2014; Davies et al. 2016; Lacerda et al. 2018; Vale Asari et al. 2019).

5 RESULTS

We present in this section the main results of the analysis described in the previous section, describing the main spectroscopic properties of the eCALIFA sample of galaxies for both the central regions and integrated galaxy wide.

5.1 Stellar population properties

Table 4 list the main properties of the stellar populations obtained for the central and integrated spectra (*cen* and *int* hereafter), including (i) the LW and MW ages and metallicities ($\mathcal{A}_{*,L}$, $\mathcal{A}_{*,M}$, $\mathcal{Z}_{*,L}$ and $\mathcal{Z}_{*,M}$), (ii) the stellar velocity dispersion (σ_*), (iii) the dust attenuation (A_V^*), (iv) the mass-to-light ratio Υ_* in the *g*-band, and (v) the stellar mass. The properties derived using the integrated spectra provides with characteristic properties of the galaxies. On the other hand, those derived from the central aperture provides information of the most inner regions. Although the sampled physical region change galaxy by galaxy, in average corresponds to ~ 500 pc. Finally, the comparison between the parameters derived for these central spectra and those derived using the integrated ones, provides with a rough estimation of any gradient in the explored property. A possible caveat is that the central aperture is (obviously) inscribed in the integrated one. However its typical contribution to the total flux is $\sim 7\%$. Thus, based on Eq. 5, the parameters derived for the integrated spectra are contaminated by the value derived for the central spectra in a similar percentage. In general, this pollution is not significant in most of the cases.

5.1.1 Stellar Masses

Deriving the mass in galaxies, and in particular, the stellar mass is a topic of the greatest interest (e.g. Courteau et al. 2014, and references therein). As described before our approach consists of decomposing the stellar spectrum in a set of SSPs included in a particular library and from the mass-to-light ratio each of them ($\Upsilon_{*,SSP}$), their contribution of light to the total flux, and correcting by the dust attenuation and cosmological distance, it is derived the stellar mass. However, in previous sections we already estimated the stellar mass using the photometric information. Figure 13 shows a comparison between the stellar masses derived for the integrated spectra based on the stellar population analysis ($M_{*,int}$), and those derived using the PS photometry ($M_{*,phot}$, Sec. 3.1). This is an usual sanity check aimed to detect possible problems in the fitting procedure, or the quality of the data, that are not obvious to a visual inspection of the spectra themselves (e.g. Sánchez et al. 2018, 2022b). Despite of the evident differences in the two approaches adopted to estimate both stellar masses, we find a good agreement, with a clear one-to-one correspondence ($\Delta \log(M_*) = 0.02 \pm 0.22$ dex). As a result of this comparison, a few galaxies were flagged from warning to bad-quality, as indicated in Sec. 2.4. In addition it is included the distributions segregated by morphology, showing the average values too. The loose relation already reported in the literature (e.g. García-Benito et al. 2017) between morphology and stellar mass is clearly shown, more evident in the average values, with late-type (early-type) being less (more) massive and covering a wider (narrower) range of masses.

5.1.2 Mass-to-light ratios

Figure 14, left panel, shows the distribution of Υ_* (*g*-band), derived for the central aperture spectra, as a function of the stellar masses,

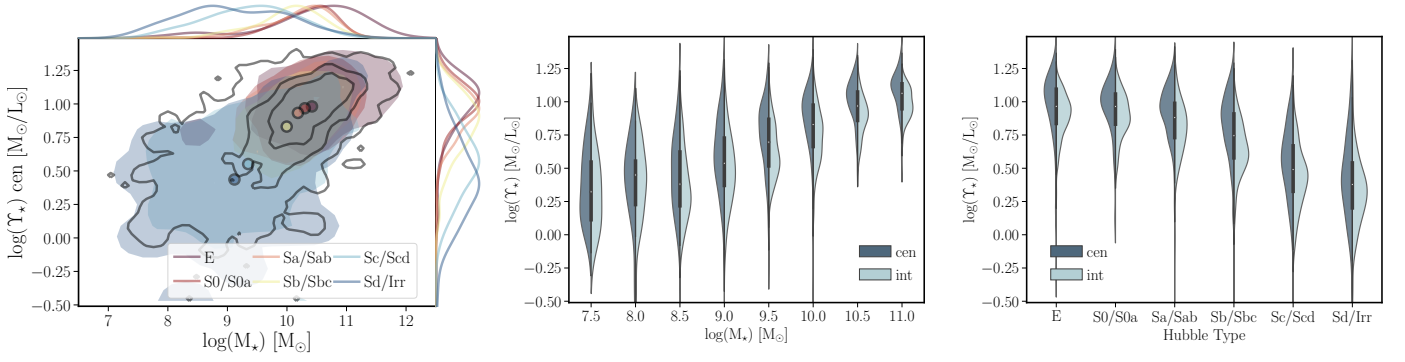


Figure 14. *Left panel:* Distribution of the g -band mass-to-light ratio (Υ_{\star}) derived for the central aperture spectra as a function of the stellar mass. Black-solid contours show the density distribution, with each successive contour encircling a 95%, 65% and 40% of the galaxies, respectively. Each shaded region corresponds to the area encircling a 85% of the galaxies of a particular morphological type, represented by a different color (inset legend). The normalized density distributions of both parameters, segregated by morphology too, are shown in the upper- and right-side panels, with the mean values represented as solid circles, both using the same color code. The violin plots of the Υ_{\star} parameter derived for the central (cen) and integrated (int) spectra as a function of the stellar mass and the morphology of the galaxies are shown in central and right panels, respectively.

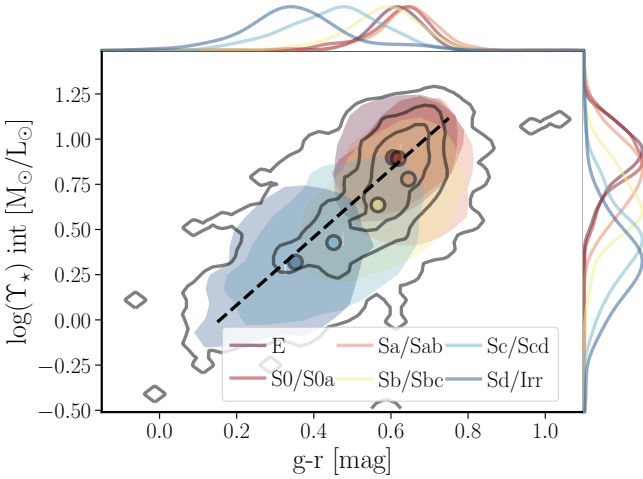


Figure 15. Distribution of Υ_{\star} in the g -band as a function of the $g-r$ colors both derived for the integrated spectra. All contours, symbols, and colors are similar to the ones adopted in Fig. 13. Dashed-line shows the Υ_{\star} vs. $g-r$ linear relation reported by [García-Benito et al. \(2019\)](#) (Table 1 of that article), shifted to match the IMFs and the photometric systems. The relation match pretty-well with our reported distribution.

for all galaxies and segregated by morphology. There is a clear trend between both parameters, with Υ_{\star} increasing from $\sim 2 M_{\odot}/L_{\odot}$ at low-mass (late-type) galaxies to $\sim 8 M_{\odot}/L_{\odot}$ at high-mass (early-type) ones. This trend it is expected as the Υ_{\star} traces the stellar composition in galaxies, having higher values as older are the stars (being a consequence of young stars having a much lower Υ than older ones). As more massive/earlier type galaxies have older stellar populations ([Kauffmann et al. 2003a](#); [Blanton & Moustakas 2009](#), and references therein), they have larger Υ_{\star} too. Since the pioneering studies using broad-band photometry (e.g. [Faber 1977](#); [Peletier et al. 1990](#)), to the more recent explorations using IFS data (e.g. [González Delgado et al. 2014a](#); [Sánchez 2020](#); [Sánchez et al. 2021a](#)), it is well known that galaxies present a radial gradients in the age of their stellar populations, leading to variations in the Υ_{\star} from the inside-out (e.g. [Zibetti et al. 2009](#); [García-Benito et al. 2019](#)), in particular in more massive and early-type galaxies. Fig. 14 shows the violin plot of the Υ_{\star} derived for the central and integrated apertures as a function of the stellar mass (middle panel) and the morphology (right

panel). As expected Υ_{\star} has higher values in the central regions of galaxies than integrated galaxy wide, reflecting the gradient in the stellar composition. This trend is more clear when galaxies are segregated by morphology, seeing

The dependence of Υ_{\star} with galaxy properties, variations from the inside out, and in particular, the analysis of the correlations with photometric colors, is a topic that has been addressed by many previous explorations (e.g. [Bell & de Jong 2000](#); [Bell et al. 2003](#); [Zibetti et al. 2009](#); [Gallazzi & Bell 2009](#); [Taylor et al. 2011](#); [Into & Portinari 2013](#); [Roediger & Courteau 2015](#); [García-Benito et al. 2019](#)). It is beyond the scope of the current study to make a detailed comparison with all of them. We will focus on [García-Benito et al. \(2019\)](#), as it is using a similar technique (spectral synthesis) for a roughly similar dataset (the DR3 CALIFA sample), although they performed a fully spatial resolved analysis, using a different fitting code and a different SSP library. The main differences between the results are (1) the adopted IMF, that implies an offset of ~ 0.29 dex in Υ_{\star} , constant for all stellar-masses, morphologies, and colors, and (2) the adopted photometric system for the galaxy colors, $g-r$, Vega in our case and AB in [García-Benito et al. \(2019\)](#). This requires an additional offset, that we took from [Fukugita et al. \(2007\)](#).

Once applied those offsets we find a very good qualitative and quantitative agreement between our results. For instance, the comparison of the results shown in Fig. 14 with those presented in Fig. 2 of [García-Benito et al. \(2019\)](#) (upper-panel), indicates that (i) the trend between Υ_{\star} and morphology, (ii) the values reported for the central regions, and (iii) the average values galaxy wide for each morphological type agree within a few percentage between both studies. A more quantitative comparison is included in Figure 15, where it is shown the distribution of Υ_{\star} as a function of the $g-r$ color, for the total sample and segregated by morphology. We include in this figure the relation reported by [García-Benito et al. \(2019\)](#) for both parameters, once considered the offsets required to take into account the differences in the IMF and photometric systems described before. There is a remarkable agreement between the published relation and the distribution traced by our measurements.

5.1.3 Age and metallicity

The decomposition of a stellar population in a set of SSPs naturally provides with an age and metallicity distribution function (ADF and MDF) in both light and mass, as is illustrated in the bottom panel

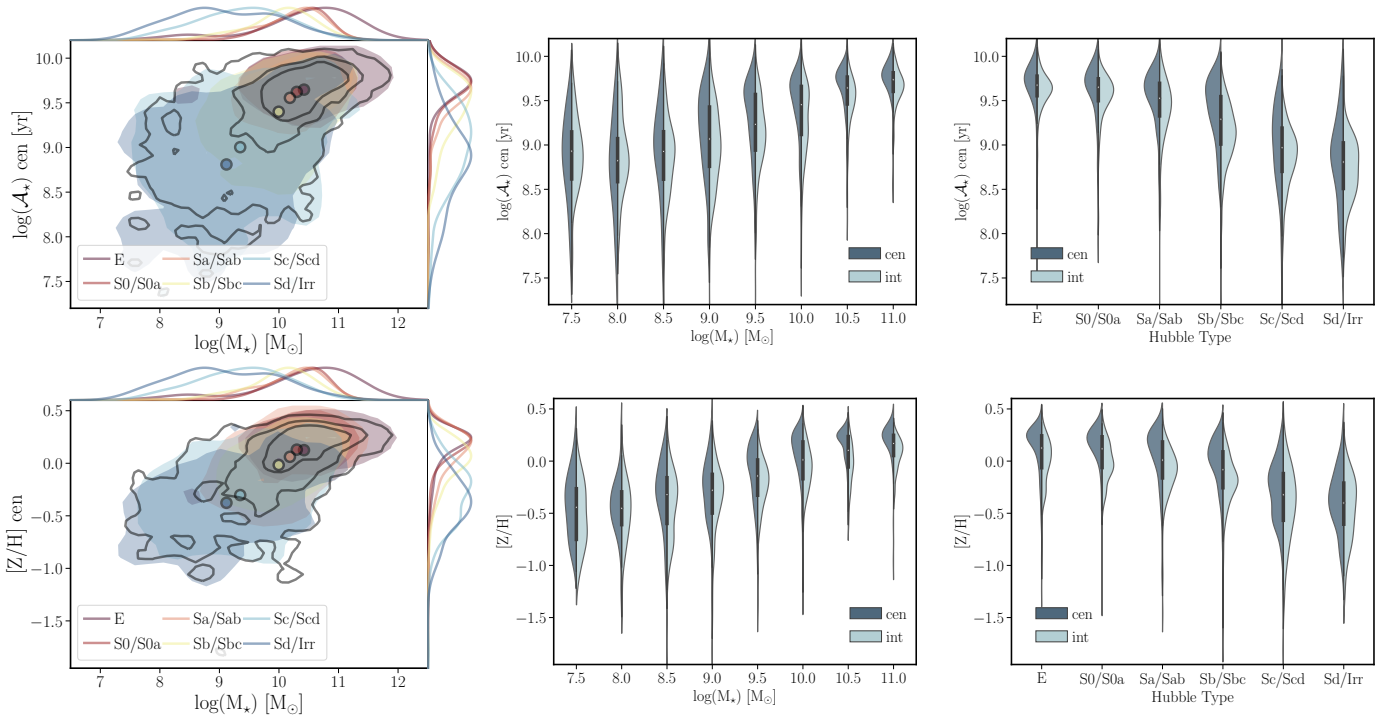


Figure 16. Distribution of the $\mathcal{A}_{*,L}$ (top panels) and $\mathcal{Z}_{*,L}$ (bottom panels), derived for the central aperture spectra as a function of the stellar mass (*left panels*), together with the violin plots comparing these parameter derived for the central (cen) and integrated (int) spectra as a function of the stellar mass (*middle panels*) and the morphology (*right panels*). We use the same nomenclature adopted in Fig. 14 for each panel.

of Fig. 12. Since the early studies by Panter et al. (2003), these distributions are used to trace the mass-assembly, chemical enrichment and star-formation histories of galaxies and regions within them (e.g. Asari et al. 2007; Pérez et al. 2013; Ibarra-Medel et al. 2016; Camps-Fariña et al. 2021, 2022), as recently reviewed by Sánchez (2020). Those distributions can be studied to compare them with results provided by resolved stellar population, in particular the MDF (e.g. Mejía-Narváez et al. 2020). In some cases, instead of analyzing the full distributions, it is more convenient to collapse them into characteristics value such as the luminosity- or mass-weighted values (i.e., those listed in Table 4). This is particular useful when exploring radial gradients in those properties or dependencies on global properties (e.g. Gallazzi et al. 2005, 2006; González Delgado et al. 2014a, 2015; Goddard et al. 2017; Sánchez 2020; Sánchez et al. 2021a). We should keep in mind that they only provide with a limited information of the real distribution of those quantities, and that the information is different depending on (1) how the average is performed (in a linear or logarithm space), (2) at which wavelength is normalized the LW, and/or (3) if it is weighted by mass or by light. In general, LW ages and metallicities, when normalized at $\sim 5000\text{\AA}$ highlights the contribution of young stars with respect to an underlying content of old stars. This way, $\mathcal{A}_{*,L}$ correlates pretty well with blue-to-red colors, stellar indices as D4000, the Υ_{*} (e.g. Kauffmann et al. 2003a; Blanton & Moustakas 2009), and $\mathcal{Z}_{*,L}$ present some trends with the gas-phase oxygen abundance (e.g. González Delgado et al. 2014b; Espinosa-Ponce et al. 2022). On the other hand, MW ages and metallicities are more representative of the bulk stellar population, and in general they present higher values (e.g. Sánchez et al. 2021a), being less suitable to explore changes in the stellar populations sensitive to the presence of young stars.

Figure 16, left-panels, shows the distribution of $\mathcal{A}_{*,L}$ (top panels) and $\mathcal{Z}_{*,L}$ (bottom panels) derived for the central aperture as a

function of the stellar masses for the full sample of galaxies, and segregated by morphology. We find a clear trend between both parameters and both the mass and morphology, with low-mass/late-type galaxies having a younger/metal-poor stellar population and high-mass/early-type galaxies having an older/metal-rich one. In this regards we reproduce well known trends, already described using aperture limited spectroscopic surveys (e.g. Blanton & Moustakas 2009; Gallazzi et al. 2006) or integral field-spectroscopy (e.g. González Delgado et al. 2014b, 2015). These trends are the consequence of global downsizing: more massive/early-type galaxies form the bulk of their stars more early in the cosmological time, having a sharper, more peaky and shorter SFH than less massive/late-type ones (e.g. Pérez-González et al. 2008). These different SFHs (and mass assembly history, MAH) produce a different chemical enrichment history (ChEH) and a final accumulated metallicity for galaxies of different mass and morphology (Panter et al. 2003). Recent results have shown that beyond these average trends, less-massive/late-type galaxies present a wider range of SFHs (MAHs) and ChEHs than more-massive/earlier-types (Ibarra-Medel et al. 2016; García-Benito et al. 2017). As a consequence, the former present a wider distribution of $\mathcal{A}_{*,L}$ and $\mathcal{Z}_{*,L}$, as indeed it is observed in Fig. 16, and previous results (e.g. González Delgado et al. 2014b). Furthermore, the shape of the ChEH seem to be equally to the morphology and to the stellar mass (Camps-Fariña et al. 2021, 2022).

Beside the different patterns in the average evolution of the stellar populations galaxy-wide for galaxies of different stellar mass and morphology, there are differences observed at different regions within galaxies: bulge-dominated/inner-regions, those with higher stellar mass density (Σ_{*}), present a sharper evolution than disk-dominated/outer-regions, i.e., those with lower Σ_{*} . This local downsizing (Pérez et al. 2013), observed as a change in the local SFHs

(MAHs) and ChEHs from the inside-out, induce a gradient in the radial distributions of the stellar properties. Fig. 16, shows the violin plots of the distribution of $\mathcal{A}_{*,L}$ (top panels) and $\mathcal{Z}_{*,L}$ (bottom panels) for both the central and integrated apertures, as a function of the stellar masses (central panels) and morphologies (bottom panels). In the case of the $\mathcal{A}_{*,L}$, for all morphologies and for $M_* > 10^{8.0} M_\odot$, the inner stellar populations are always older than the outer ones. A somehow similar pattern is observed in $\mathcal{Z}_{*,L}$, although in this case low-mass ($< 10^{8.5} M_\odot$) and later-type galaxies (Sd/Irr), present similar distributions in both apertures. These patterns can be interpreted as an inside-out growth of galaxies earlier than Sd and more massive than $M_* > 10^{8.0-8.5} M_\odot$.

The inside-out growth is thought to be connected on how disks acquired their angular momentum when formed (Peebles 1969; Larson 1976). However, the differences in the stellar-populations may be also connected with an inside-out quenching/aging of the stellar populations too (e.g. González Delgado et al. 2016; Sánchez et al. 2018; Sánchez 2020), which may be connected to a lack of molecular gas in the inner regions of galaxies, dynamical stability in bulges, the effect of AGNs, or a combined effect of all of them (for instance, see the discussion in Bluck et al. 2019). For less massive/late type galaxies an outside-in or homogeneous growth could explain the observed distribution. In general, it is required to invoke a difference in gas inflow for different galaxy types and different galactocentric distances to explain this kind of gradients (e.g. Carigi et al. 2019, and references therein). As already discussed in the recent review summarizing the results from different IFS galaxy survey (Sánchez 2020), these scenarios refer to how fast the star-formation happens in different radial distances with time, not to the amount of stars. In all galaxies it is found a negative gradient in the stellar-mass density. Thus, in all of them there are more stars formed in the central regions along the time than in the outer ones.

5.1.4 Stellar dust attenuation

Dust is one of the components of the ISM with the lowest contribution to its total mass ($< 1\%$, e.g., Santini et al. 2014). However, it has a strong impact in the shape of the spectral energy distribution and in the redistribution of photons from the UV-optical (that are absorbed and attenuated) to the infrared (due to dust thermal emission). Dust grains are condensation of metals that are formed in the atmospheres of evolved stars and supernovae remnants, and therefore it is a tracer of the evolution of stellar populations too. Being usually aggregated to molecular clouds, it is as a tracer of H_2 column density, and therefore, of the molecular gas content (e.g. Brinchmann et al. 2013; Barrera-Ballesteros et al. 2020). It is known that it affects in a different way the emission from the ionized gas, in which a pure screen model provides good estimations of the dust absorption, than to the integrated stellar populations, where dust is partially embedded and not fully covering the stellar components (e.g. Calzetti 2001; Wild et al. 2011; Salim & Narayanan 2020). As indicated before PYFIT3D provides with an estimation of the dust attenuation ($A_{*,V}$) affecting the stellar spectrum, assuming that all components of the stellar population are affected by the same attenuation and adopting a simple screen model.

Figure 17, left-panel, shows the distribution of these dust attenuation derived for the central aperture spectra as a function of the stellar mass, for all galaxy types and segregated by morphology. On the contrary to the parameters explored in the previous sections there is no simple/clear trend/pattern traced by these distributions. For most galaxy types the distribution is centred in $A_{*,V} \sim 0$ mag, with a narrow range of $A_{*,V}$ values around this central one for more mas-

sive and early-type galaxies (E and S0). For later-type, less massive galaxies, the distribution presents a tail towards larger values. However, the average value is never higher than ~ 0.25 mag, and there is no further trend with the stellar mass or the morphology. The violin plots comparing the central and integrated values as a function of the stellar mass and the morphology (Fig. 17, middle and right panels, respectively), show that, in general, the distribution of values is even more concentrated around zero for the integrated spectra than for the central ones. This trend is modulated by mass and morphology, being less clear for E and S0 galaxies, in which both values of $A_{*,V}$ are rather low.

If we interpret the dust attenuation as proxy of the molecular gas content, these results would indicate that more massive/early-type galaxies, and the outer regions of all galaxies, present a relatively lower gas content than less massive/late-type galaxies, and the inner regions of all galaxies. This is indeed has been confirmed by many previous explorations of the molecular gas content in galaxies (e.g. Saintonge et al. 2016; Calette et al. 2018). However, due to the limitations of our modelling of the dust attenuation affecting the stellar component, we should take this result with a certain precaution. We will come back to that when exploring the dust attenuation derived for the ionized gas.

5.1.5 Velocity dispersion

The analysis provides with the velocity dispersion of the stellar component (σ_*) for the two apertures. The instrumental resolution of the adopted setup (V500 grating, $R \sim 850$), corresponds to $\sim 120 \text{ km s}^{-1}$ at $\sim 5500 \text{ \AA}$. Our simulations indicate that in case of good S/N the code recovers a reliable velocity dispersion above $\sim 1/3$ of this value ($\sim 40 \text{ km s}^{-1}$, for the current data, Lacerda et al. 2022). However, it is unable to recover values below this value.

Figure 18, left panel, shows the distribution of σ_* , in logarithm scale, derived for the central aperture as a function of the stellar mass for all galaxies and segregated by morphology. Despite of the large scatter, in particular for low-mass/late-type galaxies, it is observed a clear monotonic increase of σ_* with both parameters, with a linear trend traced by the average values (solid circles) for galaxies earlier than Sd/Irr. Faber & Jackson (1976) first shown a tight correlation between the central velocity dispersion and the integrated luminosity in early-type galaxies (FJ relation). This relation is supposed to be the correspondent to the relation between the rotational velocity and luminosity found for late-type galaxies (TF relation Tully & Fisher 1977). Both of them can be described as a relation between the corresponding kinematic parameter and the stellar mass (and the baryonic mass in general), and being unified into a single relation valid for all morphological types (e.g. Weiner et al. 2006; Cortese et al. 2014; Aquino-Ortíz et al. 2018). The usual explanation for both relations suggest that (i) the central velocity dispersion (rotational velocity) is a good tracer of the dynamical mass in pressure supported (rotational supported) early-type (late-type) galaxies, and (ii) there is a tight relation between the dynamical mass traced by those parameters and the stellar mass.

When using all morphological types (Fig. 18) the relation between $\sigma_{*,\text{cen}}$ and M_* is broader, less well defined than the FJ-relation, showing a larger dispersion for late-type galaxies (e.g., Fig. 3 of Aquino-Ortíz et al. 2018). However, for early-type galaxies and early-spirals the average values shown in Fig. 18 trace very well the stellar-mass FJ relation reported in the literature.

Like in the case of other stellar properties, σ_* present known radial gradients. This is seen in the violin plots comparing the central and integrated values for this parameter as a function of the stellar

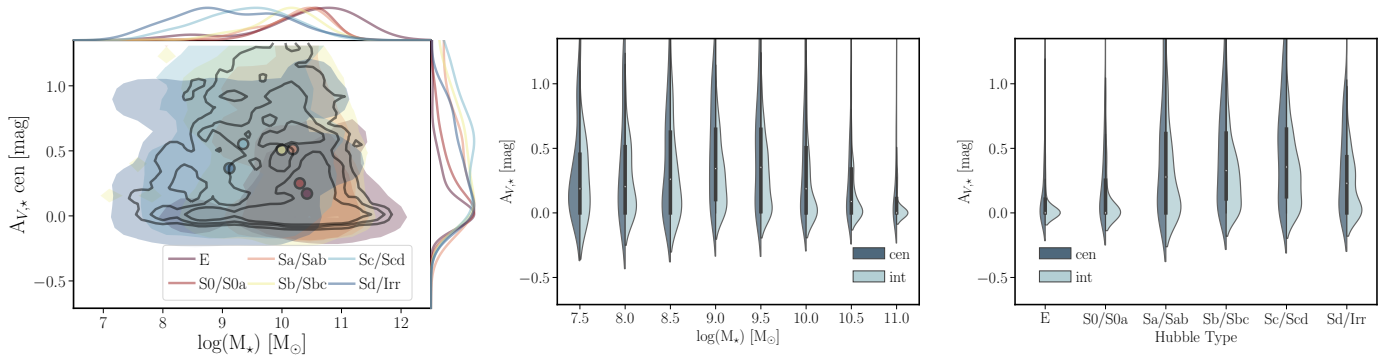


Figure 17. Distribution of $A_{\star,V}$ derived for the central aperture spectra as a function of the stellar mass (*left panel*), together with the violin plots comparing this parameter derived for the central (cen) and integrated (int) spectra as a function of the stellar mass (*middle panel*) and the morphology (*right panel*). We use the same nomenclature adopted in Fig. 14 for each panel.

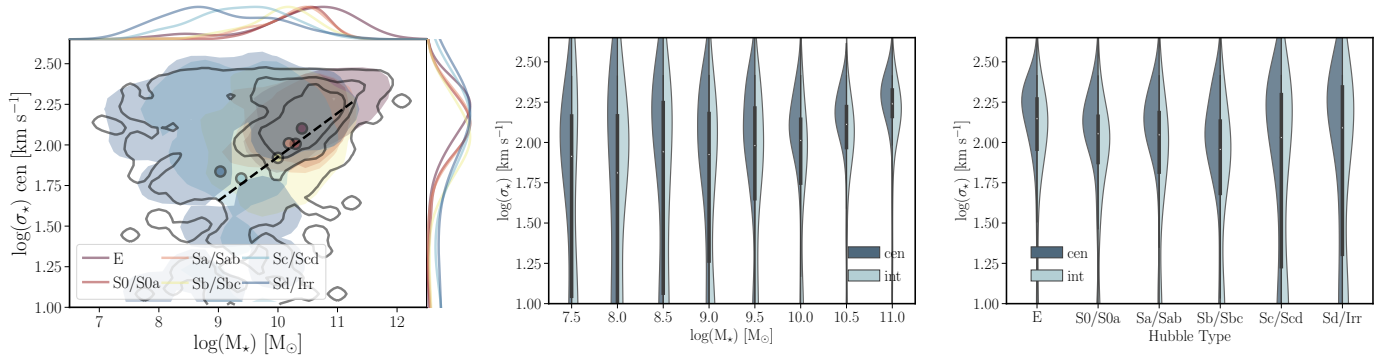


Figure 18. Distribution of σ_{\star} derived for the central aperture spectra as a function of the stellar mass (*left panel*), together with the violin plots comparing this parameter derived for the central (cen) and integrated (int) spectra as a function of the stellar mass (*middle panel*) and the morphology (*right panel*). We use the same nomenclature adopted in Fig. 14 for each panel. In addition, the dashed-black line in the left panel corresponds to the Faber-Jackson relation derived for the CALIFA sample (Aquino-Ortíz et al. 2018).

mass and the morphology (Fig. 18, central and right panel, respectively). All galaxies more massive than $M_{\star} > 10^{9.0} M_{\odot}$, and earlier than Sc (i.e., galaxies with a massive bulge), have a larger velocity dispersion in the central aperture than integrated galaxy-wide. However, for disk-dominated and/or low-mass galaxies there is no evident gradient velocity dispersion. A possible caveat in here is that in this later case the reported values are near the minimum σ_{\star} that we can reliably recover for the current dataset with our code. In any case, if there is some gradient it is much smoother than the one described for the more massive and earlier type galaxies.

5.2 Properties of the ionized gas

As indicated before, the analysis performed by `pyFIT3D` extracts the main properties of a set of defined emission lines that were described in Sec. 4.1. Table 5 lists the fluxes of the strongest emission lines for each galaxy in both apertures, with their corresponding errors. No mask have been applied to the data. Therefore, some reported fluxes may be negative or zero in this table. We advice the reader to apply the required masks based on the reported errors depending on the requirements of each particular exploration.

5.2.1 What ionizes the gas?

The segregation between the different ionization sources in galaxies is a topic of debate (e.g. Sánchez 2020; Sánchez et al. 2021a),

being particularly complicated when using aperture limited and/or integrated spectra, due to the inherent mixing between different ionizing sources (e.g. Mast et al. 2014; Davies et al. 2016; Lacerda et al. 2018). For the current exploration we adopt an heuristic approach, adopting the classification proposed by Sánchez et al. (2014) and Sánchez et al. (2018). This classification mixes two frequently used diagnostic diagrams: (i) the classical BPT diagram, proposed by (Baldwin et al. 1981), that compares the intensity of the [O III]/H β vs. [N II]/H α line ratios; and (ii) the WHAN diagram, proposed by (Cid Fernandes et al. 2010, hereafter CF10), that introduces the use of the EW(H α) to distinguish between different ionizing sources.

Figure 19 shows the distribution of galaxies across those two diagrams for both analyzed apertures. In the case of the BPT diagrams it is appreciated the classical sea-gulf distribution frequently described in the literature, that comprises (i) a well defined branch in the left-side of the diagram, tracing the usual location of classical H II regions (e.g. Osterbrock 1989), and (ii) a more extended and less defined cloud towards the right-side of the diagram. Despite of the general similarities between the distributions in this diagram for both the integrated and central apertures, there are also remarkable differences. For the integrated (central) spectra the left-side trend is much (less) clearly defined, comprising a larger (lower) number of galaxies, and the right-side cloud is more (less) diffuse, covering a more limited (extended) range towards the upper-right region of the diagram. This clearly indicates a change in the dominant ionizing source from the central to the outer regions in galaxies.

When segregating by morphology it is appreciated a somehow

Table 5. Emission line fluxes in units of 10^{-16} erg s $^{-1}$ cm $^{-2}$ estimated for the central and integrated spectra of all the galaxies.

cubename	aperture	[O II]3727	H β	[O III]5007	H α	[N II]6584	[S II]6717	[S II]6731
IC5376	int	399.4 \pm 114.8	113.3 \pm 17.0	60.9 \pm 9.1	531.2 \pm 79.7	227.0 \pm 34.0	108.6 \pm 16.3	72.1 \pm 10.8
"	cen	0.9 \pm 18.4	1.1 \pm 0.6	2.4 \pm 0.6	4.5 \pm 0.9	6.0 \pm 0.9	1.2 \pm 0.9	1.0 \pm 0.9
UGC00005	int	696.9 \pm 104.5	352.4 \pm 52.9	129.4 \pm 19.4	1527.2 \pm 229.1	657.5 \pm 98.6	369.2 \pm 55.4	264.8 \pm 39.7
"	cen	5.3 \pm 3.1	6.5 \pm 1.0	31.1 \pm 4.7	31.2 \pm 4.7	37.8 \pm 5.7	10.3 \pm 1.5	7.9 \pm 1.2
NGC7819	int	664.0 \pm 99.6	370.7 \pm 55.6	125.8 \pm 18.9	1379.3 \pm 206.9	475.2 \pm 71.3	259.7 \pm 39.0	177.0 \pm 26.6
"	cen	27.3 \pm 4.4	46.1 \pm 6.9	6.0 \pm 0.9	205.1 \pm 30.8	74.9 \pm 11.2	22.8 \pm 3.4	19.6 \pm 2.9
UGC00029	int	58.1 \pm 37.3	13.5 \pm 16.1	16.4 \pm 16.2	13.5 \pm 73.8	12.4 \pm 73.8	59.6 \pm 73.8	42.6 \pm 73.8
"	cen	0.0 \pm 3.1	0.0 \pm 0.6	0.0 \pm 0.6	1.5 \pm 3.3	4.0 \pm 3.3	4.4 \pm 3.3	1.8 \pm 3.3
IC1528	int	451.6 \pm 67.7	379.5 \pm 56.9	185.7 \pm 27.9	1504.6 \pm 225.7	534.0 \pm 80.1	333.5 \pm 50.0	238.9 \pm 35.8
"	cen	4.9 \pm 0.7	7.0 \pm 1.0	1.3 \pm 0.2	30.7 \pm 4.6	11.7 \pm 1.8	4.6 \pm 0.7	3.8 \pm 0.6
NGC7824	int	491.8 \pm 99.7	182.7 \pm 27.4	147.7 \pm 23.5	412.6 \pm 61.9	412.6 \pm 61.9	96.9 \pm 31.9	133.1 \pm 33.1
"	cen	-8.4 \pm 2.1	3.0 \pm 1.3	1.9 \pm 1.2	2.9 \pm 0.5	2.3 \pm 0.5	0.0 \pm 0.6	1.0 \pm 0.5
UGC00036	int	93.4 \pm 695.2	93.8 \pm 14.1	45.7 \pm 11.9	466.9 \pm 70.0	297.4 \pm 44.6	53.2 \pm 21.4	135.1 \pm 21.4
"	cen	14.1 \pm 53.3	5.8 \pm 0.9	4.6 \pm 0.9	39.0 \pm 5.8	26.1 \pm 3.9	7.5 \pm 1.4	6.7 \pm 1.3
NGC0001	int	503.6 \pm 75.5	454.5 \pm 68.2	114.4 \pm 17.2	2140.6 \pm 321.1	834.4 \pm 125.2	323.3 \pm 57.8	197.2 \pm 57.8
"	cen	3.6 \pm 1.7	16.3 \pm 2.4	4.6 \pm 0.9	78.6 \pm 11.8	33.1 \pm 5.0	8.2 \pm 1.5	5.3 \pm 1.5
NGC0023	int	2131.7 \pm 319.8	1585.1 \pm 237.8	666.2 \pm 99.9	7764.9 \pm 1164.7	3924.1 \pm 588.6	1506.4 \pm 226.0	1143.4 \pm 171.5
"	cen	59.4 \pm 8.9	113.3 \pm 17.0	39.8 \pm 6.0	548.2 \pm 82.2	324.4 \pm 48.7	97.1 \pm 14.6	80.4 \pm 12.1
NGC0036	int	475.6 \pm 99.3	367.0 \pm 55.0	144.0 \pm 21.6	1654.7 \pm 248.2	744.6 \pm 111.7	302.7 \pm 45.4	198.8 \pm 45.1
"	cen	2.3 \pm 2.1	1.1 \pm 0.6	3.1 \pm 0.6	5.9 \pm 1.2	13.2 \pm 2.0	2.9 \pm 1.2	2.0 \pm 1.2
UGC00139	int	934.6 \pm 140.2	352.4 \pm 52.9	220.0 \pm 33.0	807.4 \pm 121.1	236.8 \pm 35.5	165.8 \pm 26.2	109.4 \pm 25.9
"	cen	0.3 \pm 8.1	4.0 \pm 0.6	0.8 \pm 0.2	14.1 \pm 2.1	3.2 \pm 1.3	2.7 \pm 1.2	1.8 \pm 1.2
MCG-02-02-030	int	475.8 \pm 141.4	388.8 \pm 58.3	156.2 \pm 23.4	1290.7 \pm 193.6	605.2 \pm 90.8	281.6 \pm 56.8	200.5 \pm 56.1
"	cen	3.1 \pm 2.0	2.8 \pm 0.6	8.0 \pm 1.2	24.8 \pm 3.7	18.6 \pm 2.8	6.9 \pm 2.1	6.4 \pm 2.1

We present the values for just ten galaxies. The information for the remaining one is distributed electronically.

similar trend as the one observed when comparing the central and integrated apertures: later-type (early-type) galaxies are more frequently located in the left-side (right-side) branch of the distribution for both apertures. This trend is observed in both the average values and the whole distributions. Furthermore, the effect is modulated by the aperture with (i) a more clear segregation in the integrated aperture (a larger distinction) than for the central one, and (ii) a general shift to the right-side for all morphologies in the central aperture.

These results have been already presented in previous studies using similar data (e.g. [Lacerda et al. 2018](#); [Law et al. 2021](#); [Barrera-Ballesteros et al. 2022](#)), and discussed in recent reviews ([Sánchez 2020](#); [Sánchez et al. 2021a](#)). They clearly indicate that the dominant ionizing source changes from the inside-out and from earlier to later type morphologies. It is known that the left-side branch in the BPT diagram is the location occupied by classical H II regions (e.g. [Osterbrock 1989](#)), being usually assigned to ionization due to young massive OB-stars generated in recent SF events. Different demarcation lines have been proposed to limit the region populated by this kind of ionization ([Kauffmann et al. 2003b](#), ,K03 hereafter) and ([Kewley et al. 2001](#), ,K01 hereafter). The nature, actual meaning, and usability of both boundaries has been extensively discussed in the literature (e.g. [Sánchez et al. 2021a](#)). On the contrary, the right-side branch can be populated by ionization due to many different sources, all of them presenting a harder ionization than OB-stars: (i) active galactic nuclei (AGNs, e.g. [Osterbrock 1989](#)); (ii) shock ionization due to high- and low-speed gas winds ([Heckman et al. 1990](#); [Bland-Hawthorn 1995](#); [Dopita et al. 1996](#), e.g.); and ionization by hot old evolved stars (HOLMES [Flores-Fajardo et al. 2011](#)), beyond their post-AGB phase, that have lost their external envelop (e.g. [Binette et al. 1994](#)).

Different approaches have been proposed to distinguish among the ionization sources that populate the right-branch of the BPT

diagram, including the use of the velocity dispersion (e.g. [Law et al. 2015](#); [D'Agostino et al. 2019](#)), explore the shape of the ionized structures (e.g. [López-Cobá et al. 2020](#)) and/or distribution along the galactocentric distance (e.g. [Gomes et al. 2016](#)). Most of them required the use of the spatially resolved information, as recently reviewed by [Sánchez et al. \(2021a\)](#). However, for aperture limited and integrated spectra it is frequently adopted the relative strength of the ionized flux with respect to the underlying continuum, parametrized by the EW(H α). Based on the results by [Binette et al. \(1994\)](#) and [Stasińska et al. \(2008\)](#), [Cid Fernandes et al. \(2010\)](#) proposed the WHAN diagnostic diagram that compares the distribution of the EW(H α) as a function of the [N II]/H α ratio, to distinguish between SF, AGN and ionization found in retired galaxies (RG, those that are not forming stars anymore [Stasińska et al. 2008](#)), i.e., HOLMES/post-AGB ionization. It is important to note that low-intensity shock ionization (e.g. [Dopita et al. 1996](#)) and weak AGNs (e.g. [Ho et al. 1997](#)) could be also present in retired galaxies (and the center of other galaxies too). Both ionizing sources would be indistinguishable from the proposed mechanism associated to the presence of old/evolved stars using the adopted methodology. Their frequency is, however, uncertain: (i) ([López-Cobá et al. 2020](#)) found that only 12 out of \sim 260 early-type galaxies of their sample of 635 galaxies observed with MUSE present clear evidence of shock ionization, i.e., filamentary/extended ionized gas structures, with relatively high velocity dispersion and [N II]/H α values, and relatively low values of EW(H α); (ii) [Ho et al. \(1997\)](#) found that a non negligible subset of LINERs (\sim 20%) present broad H α emission, a clear evidence of the presence of an AGN. Considering both numbers together, we could establish that in about 25% of the early-type galaxies the observed LINER-like ionization could be assigned to an ionizing process different than HOLMES/post-AGBs. On the contrary all early-type galaxies present the required old-stellar populations to

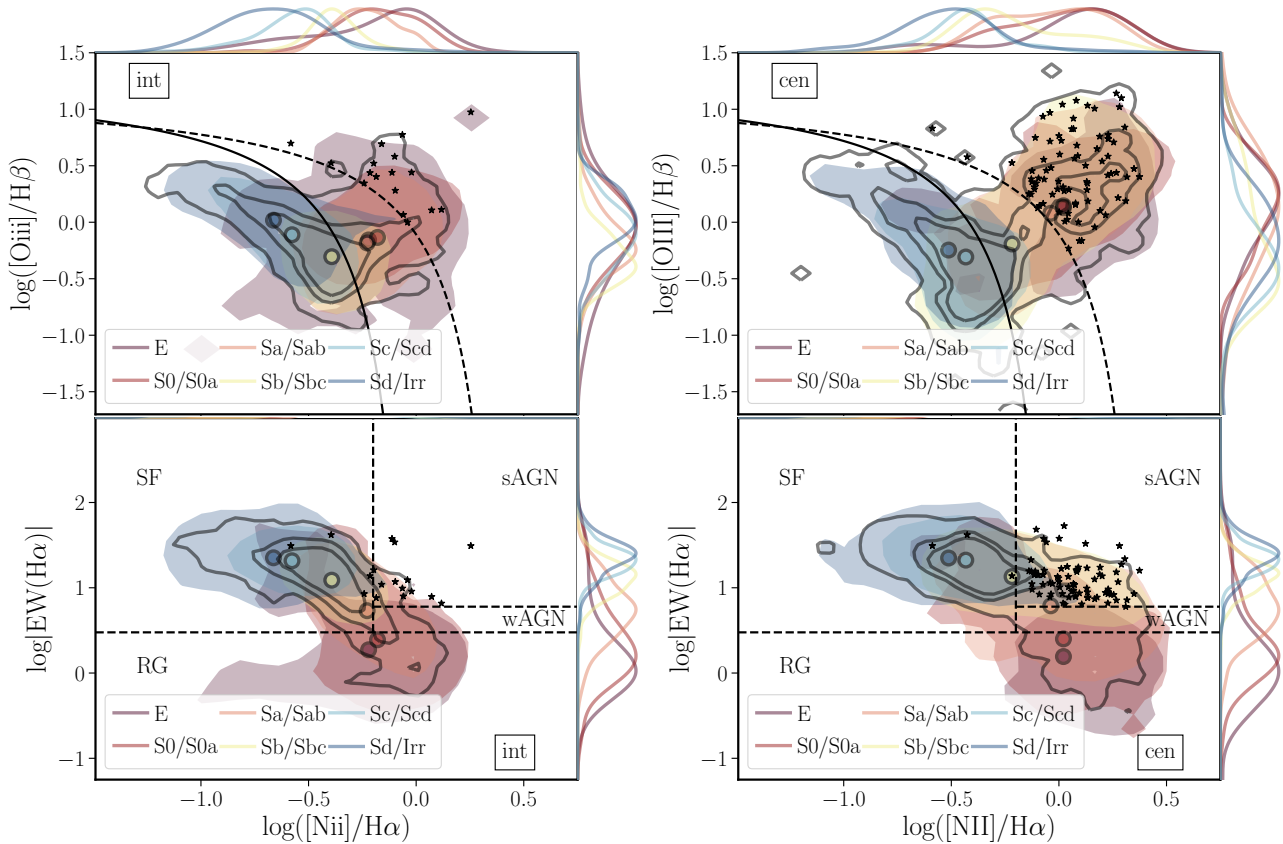


Figure 19. Distribution of galaxies across the BPT (top panels) and WHAN (bottom panels) based on the emission line properties derived from the integrated (left panels) and central (right panels) spectra. It is adopted the same nomenclature adopted in Fig. 14 for each panel. In addition, the solid and dashed lines in the BPT diagrams corresponds to the K03 and K01 demarcations lines, respectively. The dashed-lines in the WHAN diagram correspond to the boundaries defined by CF10 between different ionizing sources (as indicated in the legends). Finally, the location of galaxies candidate to host an AGNs, derived based on the central and integrated spectra, are indicated with a back star (thus, they are a different number of possible candidates).

produce this kind of ionization, that indeed is ubiquitous observed in the presence of old stars and ionized gas (e.g. Singh et al. 2013; Belfiore et al. 2017). Fig 19, bottom panels, shows the distribution of our galaxies in this diagram for both considered apertures. In the case of the integrated spectra we find a well defined anti-correlation between both parameters, with high (low) EW($H\alpha$) corresponding to low (high) $[N II]/H\alpha$ values. This trend is followed by the galaxies of different morphologies too, with later (earlier) type mostly found in the upper-left (bottom-right) regions of the diagram. As values of the $EW(H\alpha) < 3\text{\AA}$, are assigned to ionization by old stars low-intensity shocks and weak AGNs, this trend clearly indicate that a combination of those mechanisms produce the observed ionization in early-type galaxies (i.e, E/S0). On the contrary, the dominant ionization in late-type galaxies, those with a considerable amount of SF, is indeed compatible with massive young-stars.

A roughly similar trend is described by the central apertures. However, in this case, instead of a clear anti-correlation between the two parameters ($EW(H\alpha)$ and $[N II]/H\alpha$), there is less well-defined trend. The strongest difference is the presence of a bump in the region of high $EW(H\alpha)$ and high $[N II]/H\alpha$ that was assigned to strong AGN ionization by Cid Fernandes et al. (2010). When segregating by morphology, the negative trend described for the integrated spectra is appreciated, slightly shifted to higher values of the $[N II]/H\alpha$ ratio, and with the AGN-bump dominated mostly by early-spirals (Sa/Sab and Sb, in agreement with previous results Sánchez et al. 2018; Lacerda et al. 2020). This bump is coincident with the

Table 6. Distribution of the dominant ionizing sources

Ionizing source	integrated # gal.	integrated %	central # gal.	central %
NG	164	18	227	25
UN	21	2	82	9
SF	576	64	384	43
pAGB	107	12	85	9
wAGN	10	1	37	4
sAGN	17	2	80	9

Number of galaxies segregated by the dominant ionizing source for the integrated and central apertures: NG (no gas detected), UN (unknown ionizing source), SF (young massive OB-stars), pAGB (HOLMES/post-AGB old stars), wAGN (weak AGN-like ionization), and sAGN (strong AGN-like ionization).

cloud towards the upper-right region described for the same aperture in the BPT diagram. The obvious conclusion is that in the central aperture the possible contribution of an AGN or an AGN-like ionization could dominate or significantly pollute the observed ionization (e.g. Davies et al. 2016), without necessarily dominate the ionization galaxy-wide. This result highlights the importance of defining at which aperture it is classified the ionization of a galaxy, and demonstrates the importance of introducing the $EW(H\alpha)$ as an extra parameter to classify the ionization.

Based on all these results, following [Sánchez et al. \(2021a\)](#), we finally classified the dominant ionization in each aperture in the following way: (i) if the $H\alpha$ flux has a S/N below 3, it is considered that there is no ionized gas detected (NG); (ii) if $H\alpha$ is detected above this threshold, but the S/N of $H\beta$, $[N\text{ II}]$ or $[O\text{ III}]$ is below 1, then we consider that the source of the ionization is unknown (UN); finally, if the two detection thresholds are fulfilled, and (iii) the $EW(H\alpha)$ is below 3\AA , the ionization is classified as HOLMES/post-AGB (pAGB), irrespectively of its location in the BPT diagram. We should state clearly that, as indicated before, we cannot be 100% sure that the dominant ionizing source in these galaxies is actually related to the presence of old/hot evolved stars, as weak AGNs and low-intensity shocks may also contribute to the observed ionization somehow, or even dominate it ([Dopita et al. 1996](#); [Ho et al. 1997](#)); on the other hand (iv) if the $EW(H\alpha)$ is above 3\AA and the line ratios are below the K01 in the BPT diagram, the ionization is considered to be dominated by young massive stars (SF); finally, (v) if the $EW(H\alpha)$ is above 3\AA and the line ratios are above the K01 in the BPT diagram, the ionization is considered dominated by an AGN, segregating between a strong AGN (sAGN) when $EW(H\alpha) > 6\text{\AA}$, and a weak AGN (wAGN) when it is below this value. We should stress that this classification scheme does not distinguish between AGNs and shock ionization, and therefore when quoting AGN-ionization we refer to AGN-like ionization (i.e., an ionization not due to an stellar source).

Table 6 show the results of this classification. The first result to notice is the fraction of galaxies without any detected or unclassified ionized gas ($\sim 20\text{-}30\%$), in both apertures. This fraction is rather low. However, it is considerably larger than the one usually reported when using the spatial resolved IFS with a typical resolution of $\sim 1\text{ kpc}$ ($\sim 10\%$ or lower [Gomes et al. 2016](#); [Sánchez et al. 2018](#)). The reason behind this discrepancy is the dilution of the emission line signal when using large apertures. As a consequence, the number of galaxies with an ionization compatible with HOLMES/post-AGBs, i.e., the weakest one of the considered here, is very low compared to those previous studies too. This result highlights the advantage of using spatial resolved spectroscopy even when deriving integrated or global properties of galaxies.

The values in Tab. 6 agree with the distributions shown in Fig 19, for those galaxies with detected ionized gas: (i) the over-all dominating ionizing source is the presence of young massive OB stars, in particular for the integrated spectrum ($\sim 64\%$ of the galaxies); and (ii) the fraction of AGN-like ionization detected in the integrated spectra is much lower than the one found in central aperture ($\sim 3\%$ vs. $\sim 12\%$, as expected due to the dilution of the central ionizing source at larger apertures, e.g., [Davies et al. 2016](#); [Lacerda et al. 2018](#); [Albán & Wylezalek 2023](#)), being a small fraction in both cases. Figure 20 shows the distribution of the dominant ionizing source for the different morphological types. Most of the galaxies without a clear detection of ionized gas, neither in the integrated aperture nor in the central one, are early type objects (E and S0). In this kind of galaxies, when detected, the ionization is dominated by HOLMES/post-AGBs, as expected in retired galaxies ([Stasińska et al. 2008](#); [Cid Fernandes et al. 2010](#); [Singh et al. 2013](#)). As indicated before, based on the results using spatial resolved IFS, it is expected that a substantial fraction of the non-detections present ionization due to this source that it is diluted in the aperture limited spectra ([Sánchez 2020](#)). On the other hand, the ionization in the latest morphological types (Sc-Sd), is dominated by young-massive OB stars for both apertures, as expected in actively star-forming galaxies. They are the objects with the lowest fraction of non-detections too. Finally, AGN-like ionization, in particular in the central regions, is more frequently found in early-spirals (Sa and

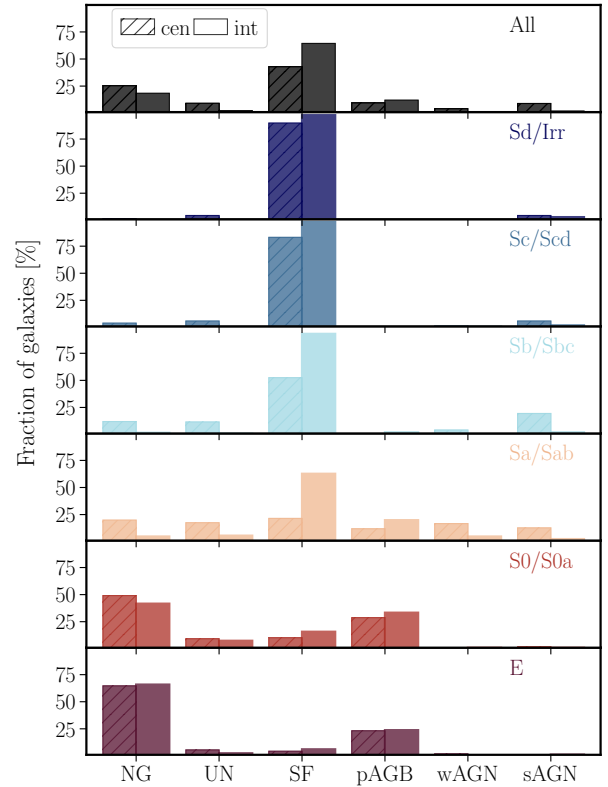


Figure 20. Distribution of the dominant ionizing sources for the different morphological types for both the central and integrated spectra, labelled as indicated in Tab. 6. As described in the text, the dominant ionizing source changes with morphology, with earlier (later) types presenting a larger fraction of (i) galaxies without (with) ionized gas and (i) post-AGB (star-formation) ionization.

Sb), although most of them are ionized by SF-related sources (in particular galaxy wide). Regarding the non-detections they present a fraction slightly larger than the latest morphological types, in particular for the central aperture, but significantly lower than that found in the earliest morphological types.

As a final remark, following [Sánchez et al. \(2018\)](#), we consider that a galaxy is clearly hosting an AGN is the dominant ionization corresponds to a strong AGN in the central aperture, irrespectively of which is the dominant ionization in the integrated spectrum¹⁰. On the other hand, we consider that a galaxy is actively forming stars if the dominant ionization is due to young-massive stars in any of both apertures. Therefore, a galaxy could belong to both categories at the same time.

5.2.2 Ionized gas vs. stellar dust attenuation

It is well known that the dust affects in a different way the —stellar continuum than the ionized gas (e.g. [Calzetti et al. 1997](#); [Wild et al. 2011](#)). There are many reason of why it is so, the most relevant ones are related to (i) the different way that dust affects UV radiation that produces the ionization, and it affects the dominant radiation in the stellar population (oldish stars), (ii) the effects of the scatter and redistribution of light in the line of sight and, maybe the most important (iii) the geometrical distribution of the dust grains with

¹⁰ Note that shock ionization may enter in this category, as indicated before

Table 7. Main physical properties derived from the emission line intensities.

cubename	Dominant Ionization		$A_{V,\text{gas}}$		$\log(\text{SFR})$ [$M_{\odot}\text{yr}^{-1}$]	12+ $\log(\text{O}/\text{H})$	$\log(M_{\text{gas}})$ [$M_{\odot}\text{yr}^{-1}$]
	int	cen	int [mag]	cen [mag]			
IC5376	SF	sAGN	1.55 ± 0.78	0.15 ± 0.08	-0.08 ± 0.01	8.54 ± 4.27	9.7 ± 4.85
UGC00005	SF	sAGN	1.3 ± 0.65	1.63 ± 0.82	0.64 ± 0.32	8.57 ± 4.28	10.17 ± 5.08
NGC7819	SF	SF	0.82 ± 0.41	1.39 ± 0.7	0.1 ± 0.05	8.53 ± 4.26	9.57 ± 4.78
UGC00029	NG	NG	0.15 ± 0.08	0.15 ± 0.08	-1.66 ± 2.18	nan \pm nan	7.07 ± 3.54
IC1528	SF	SF	1.02 ± 0.51	1.32 ± 0.66	-0.03 ± 0.0	8.52 ± 4.26	9.75 ± 4.88
NGC7824	pAGB	pAGB	0.15 ± 0.08	0.15 ± 0.08	-0.5 ± 0.03	nan \pm nan	6.99 ± 3.5
UGC00036	SF	SF	1.74 ± 1.22	2.7 ± 1.58	0.13 ± 0.06	8.61 ± 4.3	9.73 ± 4.86
NGC0001	SF	SF	1.56 ± 0.78	1.64 ± 0.82	0.44 ± 0.22	8.56 ± 4.28	9.44 ± 4.72
NGC0023	SF	SF	1.69 ± 0.84	1.65 ± 0.82	1.04 ± 0.52	8.58 ± 4.29	10.66 ± 5.33
NGC0036	SF	sAGN	1.43 ± 0.72	0.15 ± 0.08	0.54 ± 0.27	8.56 ± 4.28	10.29 ± 5.14
UGC00139	SF	SF	0.15 ± 0.08	0.63 ± 1.03	-0.62 ± 0.02	8.48 ± 4.24	7.19 ± 3.6
MCG-02-02-030	SF	sAGN	0.47 ± 0.65	3.54 ± 3.92	-0.35 ± 0.02	8.57 ± 4.28	8.43 ± 4.22

We present the values for just ten galaxies. The information for the remaining one is distributed electronically.

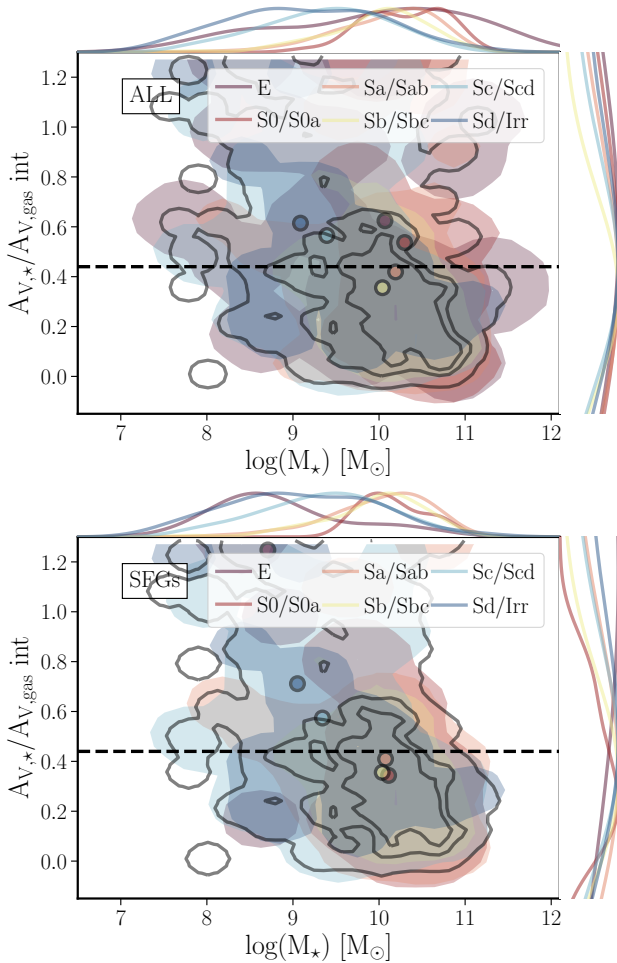


Figure 21. Distribution of the ratio between the dust attenuation derived from the fitting to the stellar component, $A_{V,*}$, and the estimated for the ionized gas, $A_{V,\text{gas}}$ for the integrated aperture, as a function of the stellar mass, for the full sample of galaxies (top panel), and the SFGs (bottom panel). The distributions segregated by morphology are shown in both panels too. We use the same nomenclature adopted in left panel of Fig. 14. The dashed line corresponds to the ratio relation between both quantities proposed by Calzetti (2001).

respect to both components (e.g. Calzetti 2001). The effect of the dust on the observed spectra is well reproduced by a simple screen model for the ionized gas, that comprises both absorption and scatter in the line-of-sight (the so-called extinction). However, the scenario is more complex for the average stellar population, in which the dust grains are embedded in the stars, and therefore the relative geometry and spatial distribution is relevant, including scatter light redirected into the line-of-sight, an interstellar medium of different column densities and optical depths, and an incomplete coverage of the dust for the average stellar population, i.e., a mixing effect of stars totally and partially obscured and/or not obscured at all (e.g. Salim & Narayanan 2020).

The net effect is that dust produces a smoother attenuation of the stellar spectra than the one expected from a pure screen model. Consequently, Calzetti et al. (1997) and Calzetti (2001) estimated that $A_{V,*} \sim 0.44 A_{V,\text{gas}}$, exploring a limited sample of star-forming galaxies (SFGs). More extensive explorations on larger samples reported a dependence of this ratio on different galaxy properties, in particular the specific SFR ($\text{sSFR} = \frac{\text{SFR}}{M_{\star}}$) and the inclination (e.g. Wild et al. 2011, using SDSS data). All these explorations are limited to SFGs in which $A_{V,\text{gas}}$ is more easily determined due to strength of the emission lines.

Figure 21 shows the distribution of the ratio between both dust attenuations, $A_{V,*}/A_{V,\text{gas}}$, as a function of M_{\star} for the sub-sample of galaxies for which we can estimate both quantities (420 objects, top-panel) and for those of which dominant ionization is compatible with SF (344 star-forming galaxies, SFGs, bottom-panel). First, we notice that the ratio between both dust attenuations covers a wide range of values, without no clear pattern with the stellar mass in the case of the full sample of galaxies. If any, there is a trend with the morphology: (i) the highest values are found in early-type galaxies (~ 0.6 , E/S0); (ii) the lowest ones in early-spirals (~ 0.2 - 0.3 , Sa-Sbc), and (iii) finally the values rise up again to a value near to the one reported by Calzetti (2001) for late-spirals (~ 0.4 , Sd/Irr). A more clear pattern with the stellar mass is observed if we limit the sample to just SFGs, with the ratio reaching the highest (lowest) values at low (high) masses. We attempt to explore the distributions reported by Wild et al. (2011), in particular the trend with the sSFR and the inclination, but we did not find clear patterns. The only galaxy parameters for which we find some trends are those that depend directly on the stellar mass, such as the oxygen abundance and the stellar metallicity.

One possible source of discrepancy between our result and the

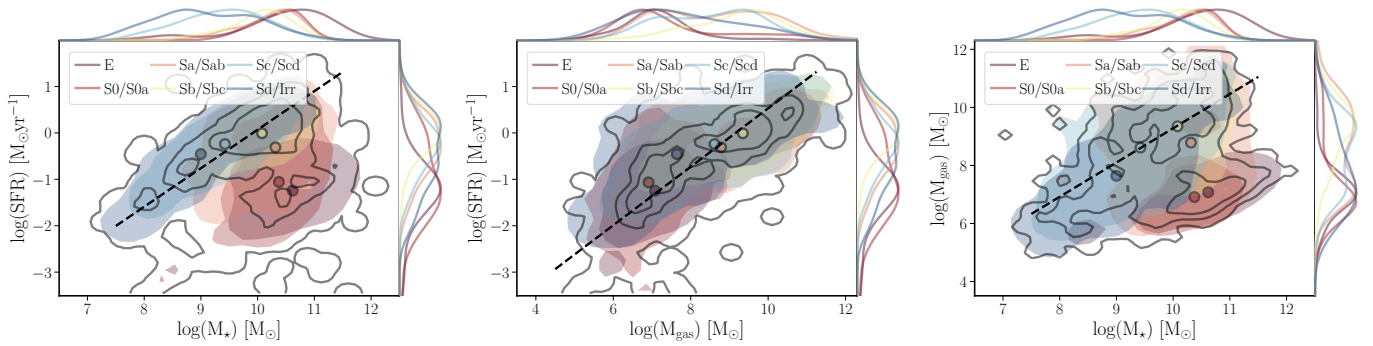


Figure 22. Distribution of (i) SFR as a function of M_* (left panel), (ii) SFR as a function of M_{gas} (central panel) and (iii) M_{gas} as a function of M_* (right panel) for the full sample of galaxies and segregated by morphology. We adopt the same nomenclature adopted in left panel of Fig. 14. The dashed-line in each panel corresponds to the extensive form of the SFMS, SK and MGMS relations for SFGs recently reported by Sánchez et al. (2022a), using the AMUSING++ compilation.

one presented in Wild et al. (2011) is the different aperture at which the dust attenuation was measured. As indicated before Wild et al. (2011) used the 3'' aperture spectra from the SDSS survey, while in here we are using the galaxy wide (IFU FoV limited) integrated spectra. Barrera-Ballesteros et al. (2022) already noticed a radial gradient in this dust ratio. For a better comparison we repeated the exploration using the dust attenuations estimated for the central aperture. Using these values we obtain similar average distributions, but with an even larger scatter in the observed distributions. Therefore, we cannot offer a satisfactory explanation for the described discrepancy so far, beside the differences in galaxy samples. The SDSS offers a several order of magnitudes larger sample than the one explored here. Maybe the patterns described by Wild et al. (2011) have a statistical nature and they only emerge for samples large enough to overcome the large dispersion introduced by individual objects in more limited samples as the studied here. We will try to address this issue in a dedicated study using the spatial resolved information provided by the current data, that could improve the quality of the derivation of the discussed parameters.

5.2.3 Star-formation rate scaling relations

The star-formation (SF) process in galaxies (and regions within them) generate three relations among the main involved parameters: (i) the rate at which star-formation happens, SFR, (ii) the accumulated stellar mass, M_* , and (iii) the ingredient from which stars are form, i.e., the molecular gas mass, M_{gas} . The relation between SFR and M_* , known as the Star-Formation Main Sequence, is well described by a linear relation between the logarithm of both parameters, with a slope ~ 1 and a standard deviation of ~ 0.25 dex (SFMS, e.g. Brinchmann et al. 2004; Renzini & Peng 2015). It has been observed at a wide range of redshifts, with a strong evolution towards larger values of SFR and lower values of M_* in earlier cosmological times (e.g. Speagle et al. 2014; Rodríguez-Puebla et al. 2016), tracing the cosmic evolution of the SFR rate (e.g. Sánchez et al. 2019a). The SFMS was first described as a relation between these two extensive quantities in galaxies. More recently it has been described as a relation between the surface densities of both quantities, Σ_{SFR} and Σ_* (i.e., two extensive quantities), being fulfilled at very different scales in galaxies, from galaxy wide to ~ 1 kpc scales (Sánchez 2020; Cano-Díaz et al. 2016; Pan et al. 2018; Sánchez et al. 2021b).

On the contrary, the relation between the SFR and M_{gas} was first described as an intensive relation between the star-formation and the molecular gas surface densities (Σ_{mol}): Kennicutt (1998) shown that

the logarithm of both quantities follows a linear relation with a slope ~ 1.4 , in agreement with the expectations by Schmidt (1968). Like in the case of the SFMS, this relation, known as the Schmidt-Kennicutt (SK) law, is fulfilled at for a wide range of galaxy scales (Wong & Blitz 2002; Sánchez et al. 2021b, 2022a). Although there is less agreement on its actual slope, being more near to one in the studies at a kpc-scale (e.g. Lin et al. 2019; Sánchez et al. 2021b), in all cases is described as a tight relation, with a scatter of ~ 0.2 dex (e.g. Bigiel et al. 2008; Leroy et al. 2013).

Finally, a third relation, known as the Molecular Gas Main Sequence (MGMS), has been described between M_{gas} and M_* (e.g. Saintonge et al. 2016; Calette et al. 2018). It follows a similar tight distribution in the log-log plane of both parameters with a slope near to one. This relation, like the other two, has a intensive correspondence that it is fulfilled in a wide range of physical scales (Lin et al. 2020; Sánchez et al. 2021a,b, 2022a). The three relations are though to be strongly inter-connected, and nowadays it is considered that the self-regulation of the star-formation activity due the feedback produced by stellar winds is most probably behind them (e.g. Ostriker et al. 2010; Sun et al. 2020; Barrera-Ballesteros et al. 2021b).

The three relations are fulfilled for actively star-forming galaxies, SFGs (and star-forming areas in galaxies), while galaxies in which the SF is halted (either quenched or aged Corcho-Caballero et al. 2023) clearly deviate from them. Retired galaxies (and regions within them), i.e., those where the star-formation activity has been halted, are found well below the SFMS, being the distance to this relation (ΔSFMS) a gauge of the quenching/halting stage of those galaxies (regions) (e.g. Colombo et al. 2020; Bluck et al. 2019, 2020). The comparison between this distance and the offset with respect to the other two relations is used to determine which is the dominant process that drives the halting of the SF: (i) the lack of molecular gas (in ΔSFMS correlates with ΔMGMS) or (ii) a decline in the star-formation efficiency (if it correlates with ΔSK) (e.g. Ellison et al. 2020b; Colombo et al. 2020). The universality or not of those relations is a question of debate, being described considerable variations galaxy to galaxy (e.g. Ellison et al. 2020b), and deviations with the morphological type (e.g. González Delgado et al. 2016; Catalán-Torrecilla et al. 2017; Cano-Díaz et al. 2019; Méndez-Abreu et al. 2019).

Figure 22 shows the distributions across the SFR- M_* , SFR- M_{gas} and M_{gas} - M_* diagrams derived for the integrated spectra of our analyzed sample. The distributions are shown for all galaxies and segregated by morphology. For comparison purposes we included one of the most recent derivations of the three relations described be-

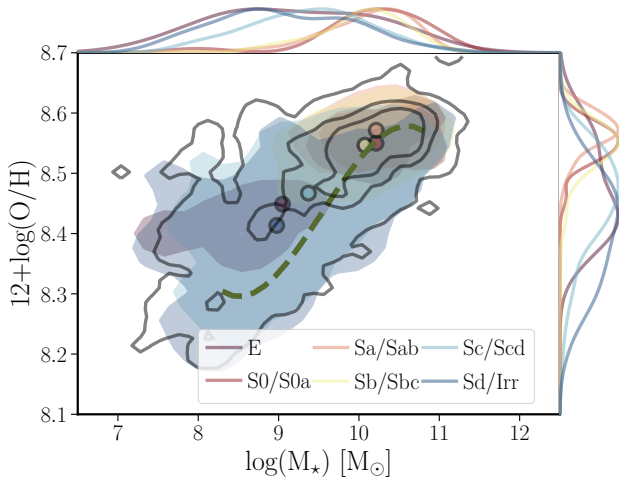


Figure 23. Distribution of oxygen abundance, $12+\log(\text{O}/\text{H})$, as a function of the stellar mass derived for the integrated aperture. We use the same nomenclature adopted in left panel of Fig. 14. The green dashed-line corresponds to the MZR reported by Sánchez et al. (2019b) using the oxygen abundance measured at the effective radius for the SAMI survey dataset.

fore (SFMS, SK and MGMS relations), published by Sánchez et al. (2022a). In the three diagrams these relations trace regions with clear high density of galaxies. However, in the case of the SFR- M_* and $M_{\text{gas}}-M_*$ diagrams the distribution is bimodal, with late-type galaxies (Sb-Sd) tracing the SFMS and MGMS relations, early-type galaxies (E/S0) well below both relations (by 2 dex in average), and early-spirals (Sa/Sab) located within both density peaks, slightly below both relations. On the contrary, the SFR- M_{gas} does not present a clear bimodal distribution. All galaxies, irrespectively of its morphology seems to be located around the reported SK-law.

Based on these distributions we confirm that halting/quenching of the SF strongly depends on the morphology, in agreement with many previous explorations (e.g. Blanton et al. 2017; Catalán-Torrecilla et al. 2017, and references therein). Indeed, it is known that SF activity happens in the disk of galaxies, being absent of bulges (e.g. Méndez-Abreu et al. 2019). The fact that halting of SF is related with the presence of bulges (and bulge dominated galaxies), agree with the scenario in which this process happens from the inside-out in the bulk population of galaxies (e.g. González Delgado et al. 2016; Ellison et al. 2018). Whether this is connected with the presence of an AGN or other mechanisms that may suppress the SF in the presence of a bulge is still a question of debate (e.g. Sánchez et al. 2018; Bluck et al. 2019; Kalinova et al. 2022). Irrespectively of which is the actual mechanism, the described distributions confirm the results suggesting that a lack of molecular gas is a necessary process to halt the SF. Retired galaxies, those below the SFMS more than 1 dex, present a deficit of molecular gas of a similar amount with respect to the MGMS. In other words, their molecular gas fraction is considerably lower than the one found for SFGs. On the contrary, they do not present a similar offset with respect to the SK-law. As this relation traced the location of nearly constant star-formation efficiency ($\text{SFE} = \frac{\text{SFR}}{M_{\text{gas}}}$), our results suggest that the halting of SF, galaxy wide, is not driven by a severe decline in the SFE. In this regards we agree with recent results that uses more direct estimations of the molecular gas based on CO observations (e.g. Colombo et al. 2020; Ellison et al. 2020a), although the relevance of the SFE in the modulation of the SF process is still under debate (e.g. Lin et al. 2019; Ellison et al. 2020b; Sánchez et al. 2021b)

5.2.4 Mass-metallicity relation

One of the main products of the stellar evolution is the generation of metals (i.e., elements heavier than helium). Those metals can be expelled during the life-time of stars within the stellar winds, but primarily are distributed to the ISM in the final stages of the stellar evolution (e.g. Yates et al. 2013). The main distributors of metals are super-novae, with the vast majority of iron-peak elements being produced in SN-Ia, the result of the collapse of binary systems. On the contrary α -elements are primarily the result of core-collapse supernovae, the end-phase of the evolution of very massive stars (e.g. Matteucci 1992; Woosley & Weaver 1995; Kobayashi et al. 2020). The connection between the production of α -elements and the star-formation process induces a direct relation between the abundance of those elements in the ISM and the stellar mass, known as the mass-metallicity relation (MZR, e.g. Pilyugin et al. 2007). This relation was known for decades as a relation of oxygen abundance with galaxy luminosity (e.g. Vila-Costas & Edmunds 1992). However, it was not described and explored in detail until large spectroscopic surveys of galaxies were available (e.g. SDSS York et al. 2000b). Tremonti et al. (2004) demonstrates that the MZR is a tight relation, with a dispersion of ~ 0.1 dex (~ 0.06 dex in the most recent explorations, e.g. Alvarez-Hurtado et al. 2022), that expands through several orders of magnitude in stellar mass (from $10^7 M_{\odot}$ to $10^{13} M_{\odot}$). The MZR rises from low M_* values following an almost linear shape down to $M_* < 10^{9.5} M_{\odot}$, bending afterwards and reaching a plateau at a maximum oxygen abundance value (e.g. Maiolino & Mannucci 2019, and references therein). This shape clearly departs from the expectations from a pure close-box model, with the asymptotic abundance being lower than the pure expectations from the maximum yield (e.g. Pilyugin et al. 2007). Different mechanisms have been proposed to modulate the shape of the MZR, mostly related with the infall of pristine (or lower metallicity) gas into the galaxy, outflows of metal rich gas, and the differential star-formation histories between galaxies of different final stellar masses (e.g. Sánchez Almeida et al. 2014; Zhu et al. 2017; Sánchez 2020; Maiolino & Mannucci 2019).

Figure 23 shows the distribution of oxygen abundances, derived from the integrated spectra, as a function of the stellar masses for the SFGs in our sample (the only ones for which we have a reliable estimation of the oxygen abundance). In general the distribution follows the expected shape for the MZR, with a monotonic increase from low towards high masses. No evident deviation from the global trend is found when we explore the distributions segregated by morphology, beside the mass range covered by each morphological type within the SFGs subsample. Beside that, the global distribution present some differences with the reported trend described for the MZR, at least with the archetypal one (Tremonti et al. 2004). First, we do not appreciate a clear plateau or asymptotic oxygen abundance at high M_* . Second, the scatter of the distribution seems to be larger at low stellar masses than at high ones. We should note that indeed both differences have been noticed in previous explorations of the MZR using IFS data similar to the ones included in this study (Barrera-Ballesteros et al. 2017; Sánchez et al. 2017, 2019b; Cresci et al. 2019; Alvarez-Hurtado et al. 2022). The lack of plateau at high-mass is most probably due to the poor statistics (low number) of galaxies in this regime, being more evident when the data are binned and the average oxygen abundance is estimated in different intervals of stellar masses (e.g. Alvarez-Hurtado et al. 2022). On the other hand, the larger scatter at lower stellar masses is usually attributed to the fact that SDSS spectroscopic measurements are restricted to the central areas of the galaxies, implying an aperture

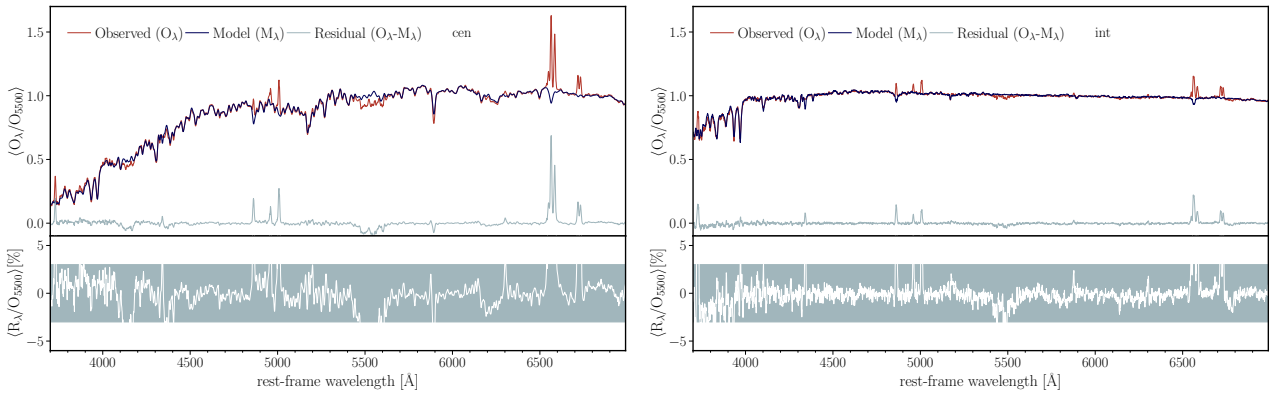


Figure 24. Statistics of the residual spectra. Top panels shows the mean normalized spectrum extracted from the central $1.5''$ aperture (left panels) and integrated across the entire FoV (regions with $S/N > 3$, right panels), for the 895 galaxies in the final sample, normalized at $\sim 5500\text{\AA}$. In addition we include the average of the individual stellar population models generated by `pyFIT3D`, and the corresponding residuals. Bottom panels show a zoom of these residual spectra, in percentage, with a shaded rectangle encompassing the $\pm 3\%$ area.

effect on those data. When using IFS data, and in particular when measuring the oxygen abundance at a particular characteristic radius (e.g., the effective radius) most studies describe a similar increase in the scatter (as indicated before).

An additional difference with previous published results is that the MZR described by our integrated apertures is shallower than the one reported using spatial resolved spectroscopic data (e.g. [Barrera-Ballesteros et al. 2017](#); [Cresci et al. 2019](#); [Sánchez et al. 2019b](#); [Alvarez-Hurtado et al. 2022](#)). To illustrate this effect we include in Fig. 23 the average relation derived for the O3N2 and N2 calibrators using the IFS from the SAMI survey ([Croom et al. 2012](#)), applying a global shift in the stellar masses to take into account the aperture effects due to the limited FoV of the SAMI IFU ([Sánchez et al. 2019b](#)). Despite of this shift there is a general offset, that increases from high to low masses. We observe this pattern irrespectively of the adopted parametrization for the MZR for the considered calibrator from the different publications listed above (some of them using CALIFA data too). We select this particular one since [Sánchez et al. \(2019b\)](#) reported a flattening in the distribution at low stellar masses, what could corresponds to a shallower rise of the MZR in this regime. However, even in this case, the offset is evident.

As indicated before there is a fundamental difference in the way we estimate the oxygen abundance for each galaxy in this exploration and the way it was derived in the quoted explorations using IFS: in here we first derive the integrated spectrum, and then we estimate the line fluxes from which we finally estimate the oxygen abundance (e.g. [Sánchez et al. 2022b](#), , for quoting an example). On the previously quoted articles the spatial resolved spectra are analyzed individually, deriving the flux intensities spatially resolved. Then, after selecting the individual spaxels which ionization is compatible with young-massive OB stars, the spatial distribution of the oxygen abundance is derived. Finally, the value at the effective radius is obtained, being considered the representative oxygen abundance of the bulk galaxy. The reported difference indicate that the oxygen abundance derived from the integrated spectra is representative of the bulk distribution only at a first order. Indeed, it is known that the dilution and the pollution by other ionizing sources alter the line ratios and the final estimated oxygen abundances (e.g. [Mast et al. 2014](#); [Davies et al. 2016](#); [Lacerda et al. 2018](#); [Vale Asari et al. 2019](#)), however, to our knowledge this is the first time that a differential bias depending on the stellar mass range is reported. We will investigate this effect in detail in future explorations replicating

the analysis that derive the oxygen abundance at the effective radius using the improved data reduction, and expanding the comparison using different abundance calibrators.

5.3 Statistics of the residual spectra

The residual spectra, once subtracted the best fitted stellar population model to each individual spectrum, contains valuable information of the quality of the data and the accuracy of the data reduction (e.g. [Walcher et al. 2015](#); [García-Benito et al. 2015](#); [Sánchez et al. 2016b](#)). Imperfections in the sky-subtraction, problems in the blue-to-red spectrophotometric, and even defects in the wavelength calibration are easily identify when exploring these residual spectra. Following those studies we perform two different analysis to explore the information included in the residual spectra. First, we derive the average residual, in order to enhance all the possible systematic effects/issues. Second, we the individual residual spectra at the spectral pixel level, to evaluate its compatibility with the error estimated by the reduction procedure. Despite of its benefits to identify all these possible defects and to characterize the quality of the spectra, we must remind that this kind of analysis has inherent limitations related to the accuracy on how stellar population models match real galaxy spectra ([Cid Fernandes et al. 2014](#)). These limitations should be considering when exploring the results of this analysis.

To obtain the average residual we first shift each observed, stellar population model and residual spectrum (as shown in Fig. 12) to a common rest-frame making use of the redshift (systemic velocity) obtained by the fitting procedure. This shift involves an inevitable interpolation and re-sampling of the spectra. Once all spectra are in the common rest-frame, we obtain the average spectrum for each component (original, model and residual), for both aperture datasets (central and integrated). We treat them separately as they correspond to data with two different levels of S/N , and therefore its separate evaluation would allow to gauge better the potential impact of any systematic effect.

Figure 24 shows the resulting average spectrum for each component at each aperture, normalized at $\sim 5500\text{\AA}$. As expected there is an evident difference in S/N between the two average observed spectra, ~ 100 for the central aperture and ~ 300 for the integrated one, reflected in the range of values of the residuals in the bottom panels. In the case of the integrated spectrum the residuals present almost no pattern or substructures along the entire wavelength range shown

in this figure. Beside the location of the strongest emission lines, the residual is restricted to a 1-2% band, with only two clear deviations: (i) below 3900Å, where there is a systematic turn towards values around $\sim -3-4\%$, and (ii) at $\sim 5500\text{Å}$, showing a clear mismatch between the average observed spectrum and the model, with the former showing a systematic dip. On the other hand, in the central spectrum the residuals present stronger patterns and substructures, despite the evident decrease in signal-to-noise. Although the turn-down at short wavelengths ($<3900\text{Å}$) in the residual spectrum is not appreciated, the dip at $\sim 5500\text{Å}$ is stronger and more clearly defined. Beside that, there is a second clear dip observed at $\sim 5100\text{Å}$ and a possible one at $\sim 6200\text{Å}$.

The origin of all these patterns can be explained by a combination of different reasons. The deviations at the blue end are most probably due to (i) the difficulty to provide with an accurate spectrophotometric calibration at the covered wavelength range, (ii) small but noticeable errors in the estimation of the atmospheric dust estimation, and (iii) imperfections in the subtraction of the night-sky spectrum, that is in general bluer than most galaxies integrated (and central) spectra. In addition, there are clear miss-matches between the co-added observed spectrum and the corresponding co-added model at certain spectral features. The most clear one corresponds to NaD ($\sim 5893\text{Å}$), although there are others like TiO2 ($\lambda 6230\text{Å}$) that are also appreciated, in particular in the spectrum corresponding to the central regions. There is a combination of reasons for those miss-matches: (i) a contribution of the ISM to the absorption features (e.g., NaD), (ii) dependence of the absorption features in properties not considering when modelling the SSPs (e.g. IMF or $[\alpha/\text{Fe}]$ changes), (iii) intrinsic imperfections in the stellar libraries used to generate the SSP and the overall stellar synthesis modelling itself. We should note that despite of those effects the deviation is of the order of 1-2%, when ignoring the particular miss-matches discussed before. The broad dips at well defined wavelength regimes are all associated with the location of strong night-sky and light pollution emission lines at the observatory (Sánchez et al. 2007). Those strong lines usually produce residuals in the spectra after subtraction (see the well defined residual at 5577Å in the observed spectrum shown in Fig. 12). The blue-shift introduced in the individual spectrum to rearrange all them into a common rest-frame to produce the described average spectrum naturally generates a broad feature. The fact that this feature is negative indicates that somehow there is a systematic over-subtraction of the strong night-sky and light-pollution emission lines, of the order of a $\sim 2-3\%$. In any case, those wavelength should be masked in any spectroscopic analysis of the data, and therefore, they have a limited effect in the quality of any science result.

5.4 Characterization of the noise

Figure 25 shows the histogram of the individual residuals at each spectral pixel for all the central aperture spectra of all the galaxies in our sample, once removed the best fitted model, relative to the error value estimated by the reduction procedure at the same spectral pixel. In the case of a perfect estimation of the pixel-wide error and a perfect modelling of the stellar population (that, as we discussed before is not the case) this distribution should follow a perfect Gaussian distribution with a $\sigma = 1$. We include this expected distribution for comparison purposes, in particular as most of the users would adopt a Poisson distribution for most of their calculations. The distribution of residuals follows a well defined symmetrical shape, centred in the zero value, indicating that it is not dominated by any strong systematic deviation, in agreement with the results from the analysis of Fig. 24. Its shape is clearly sharper/peaky than the one

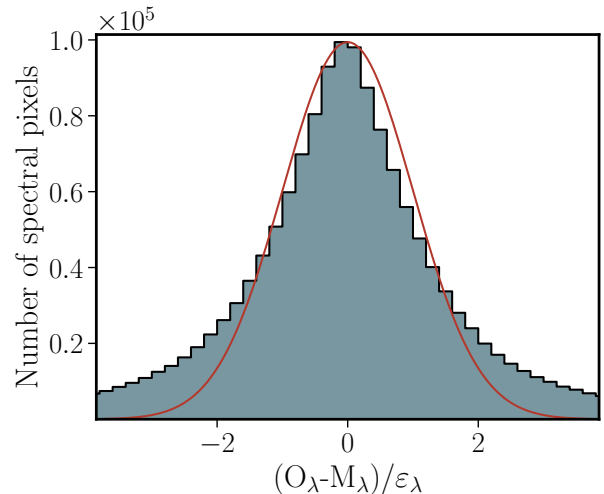


Figure 25. Histogram of the reduced residuals, $(O_\lambda - M_\lambda)/\epsilon_\lambda$, where O_λ and M_λ corresponds to the observed and model spectra for the central aperture of each good quality datacube which average value is shown in Fig. 24, and ϵ_λ is the error estimated by the reduction procedure. A total of ~ 1.5 million spectral pixels are included in the figure. The red line shows a Gaussian function scaled to the peak of the histogram with a width of one

traced by a Gaussian distribution, and present wider wings. Indeed a Power spectrum would represent better the observed distribution than a Gaussian function. This indicates that in some spectral pixels the residuals are slightly smaller than the estimated noise, and in other ones they are slightly larger. This is somehow expected, due to the statistical nature of the current comparison: the residuals are, in the best case, a realization of the errors, if the errors are perfectly estimated and all residuals are the result of a pure stochastic fluctuation driven by photon (white) noise. Furthermore, in the presence of systematic effects the residuals should be considerable larger, in absolute value, what may explain the wider tails with respect to the expected distribution. Indeed, as indicated in the previous section, the adopted stellar spectra modelling introduce several systematic residuals that are not accounted by a pure Poisson statistics. Despite of those details this comparison shows that statistically speaking the estimated errors are representative (i.e., of the same order) of the observed residuals.

Once determined how representative is the error reported by the data reduction of the real one, it is important to illustrate how to propagate it when co-adding spectra. Any image reconstruction algorithm that combines dithered exposures with an original aperture (e.g., fibers) larger than the final selected sampling pixel inevitable generates a noise covariance between adjacent pixels. This needs to be taken into account for a correct error propagation when combining/spatial-binning spectra to increase the signal-to-noise, what it is required in many cases when analyzing IFS data (e.g. Cappellari & Copin 2003). Some data reduction procedures provide with the spatial covariance of the individual datasets to address this issue (e.g. Sharp et al. 2015). In the different versions of the data reductions of the CALIFA data we adopted a simpler and a more practical approach to take into account the noise correlation, by providing the noise correction factor introduced by the spatial covariance $\beta(N)$. This parameter is the ratio between the error estimated on the combined spectrum and the one derived analytically by propagating the individual errors of each spectra. By construction β depends on the number of co-added spectra (N). To estimate this parameter

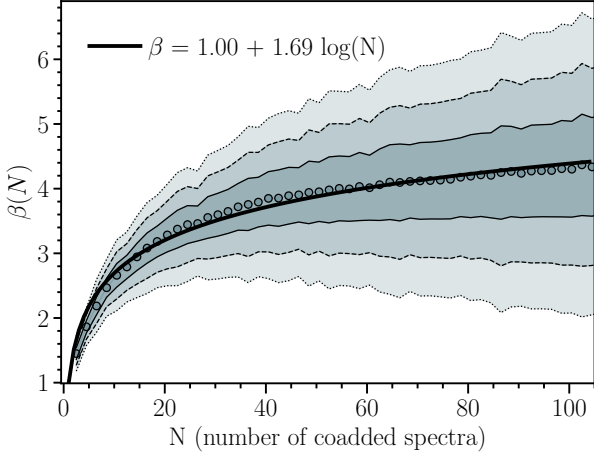


Figure 26. Correction factor to the noise introduced by the spatial covariance, $\beta(N)$, as a function of the number of co-added adjacent spaxels for the new reduced dataset for a typical target with $S/N > 20$. Shaded regions indicate the 1σ , 2σ and 3σ width areas around the average value, traced by the grey solid circles. The solid-line shows the best fitted model, following logarithmic parametrization, as shown in the legend.

we randomly generate a set of circular apertures of different sizes (and number of encircled spaxels) and extract the corresponding co-added spectra for the final reduced set of datacubes. We select those spectra with a minimum $S/N > 20$, iterating the procedure until we reach a total of ~ 1 million spectra. Then, for each aperture, we estimate (i) the error empirically as the standard deviation obtained from the detrended spectra within the $5590\text{--}5710\text{\AA}$ range in the rest frame, and (ii) the expected error, in the absence of co-variance, derived by propagating the individual errors in each spectra within the considered aperture, using the same exact procedure. The ratio between both parameters provides the β parameter for the corresponding spectrum.

Figure 26 shows the distribution of the resulting ~ 1 million estimations of $\beta(N)$ as a function of the number of co-added spaxels/spectra (N). Like in the case of previous data-reductions, this distribution is well parametrized by a logarithmic function:

$$\beta(N) = 1 + \alpha \log(N) \quad (7)$$

with a slope $\alpha = 1.69$. This value is considerable larger than the reported in previous data-releases (e.g. [García-Benito et al. 2015](#); [Sánchez et al. 2016b](#)). The reason behind that is the finally selected spaxel size ($0.5''$), half of the one adopted in previous data-reductions. As already indicated, the new adopted cube reconstruction algorithm (Sec. 2.2.6), improves the spatial resolution, what forces us to select a smaller spaxel scale (for a proper sampling of the final PSF). However, it cannot decrease the level of covariance, that for smaller spaxels is larger as the original fiber size has not changed. In other words, the same number of adjacent binned/co-added spectra corresponds to an smaller aperture (in arcsec) in the current dataset than in the previous ones. Therefore, they correspond to spaxels covered by a lower number of originally independent spectra (i.e., different fibers).

We should stress that this derivation of the effect of the covariance in the error propagation is completely empirical and does not require the use of the errors provided by data reduction. Thus this correction is valid even in the case that the original errors are not well represented by a Poisson distribution (see discussion on

Fig. 25 above), as it accounts for the covariance between adjacent spaxels. A detail description on how to use this correction in a practical way when co-coadding spectra was already included in the articles presenting the second public data-release of the CALIFA survey ([García-Benito et al. 2015](#)). We refer the reader to that manuscript avoiding a repetition of its content.

6 SUMMARY AND CONCLUSIONS

Along this article we have described a new procedure to reconstruct the datacubes from dithered fiber-feed IFS observations that improves the final spatial resolution, being now limited by (1) the distance between adjacent (dithered) fibers and (2) the input/natural seeing. We apply this procedure to the extended CALIFA dataset, a compilation of ~ 1000 galaxy observations in the nearby universe ($z \sim 0.015$) using the low-resolution setup adopted along that survey. This provides us with a remastered version of the datacubes that we distribute to the community. From this compilation we select a subset of good quality observations, based on a detailed quality examination, comprising a galaxy sample which main selection criteria is that its diameter (roughly) match with the FoV of the PPAK instrument. We characterized the main properties of this sample of 895 galaxies, providing with the location, redshift, morphological type, a sub-set of the photometric properties. We demonstrate that it is possible to obtain a rough but reliable volume correction for this sample, based on the equivalent volume accessible due to the diameter selection. The information regarding this galaxy sample, including the volume correction, is distributed too.

We extract two spectra for each galaxy, one covering the central regions and another one covering the full FoV of the IFU, to demonstrate the quality and usability of the new data. We perform a spectral fitting on each individual spectrum decoupling the contribution of the stellar populations and ionized gas, and deriving a set of central and integrated properties for both components. Among them we estimate, for the stellar populations, the average ages, metallicities, and mass-to-light ratios, together with the dust attenuation affecting them and the velocity dispersion. For the ionized gas, we estimate the flux intensities of the strongest emission lines within the wavelength range of the dataset. From them we explore the dominant source of the ionization, the dust attenuation affecting the ionized gas, the star-formation rate and the oxygen abundance. Using all this dataset we present the main patterns and distributions of the different parameters and physical properties as a function of the stellar mass and the morphology of the considered galaxies. When suitable we compare the behaviour for the inner regions with those obtain galaxy wide, tracing possible radial trends within galaxies. Once more, all these parameters and dataproducts have been distributed within the current manuscript.

We compare our results with previous ones extracted from the literature, both using photometric, single aperture and spatial resolved IFS data. In general we find a considerable agreement with previous results. A coherent picture emerges, in which (i) the stellar population content in galaxies, traced by the average ages and metallicities, (ii) the star-formation stage, (iii) the gas content, (iv) its metallicity, and (v) the dominant ionizing source strongly depend on the final stellar mass, morphology and location within each galaxy (primarily the galactocentric distance). These results agree with those of the most recent studies on the topic (e.g. [Blanton et al. 2017](#); [Kewley et al. 2019](#); [Maiolino & Mannucci 2019](#); [Sánchez 2020](#), and references therein).

In a forthcoming article we will present the analysis of the spa-

tial resolved data distributed here, following [Sánchez et al. \(2022b\)](#), making a particular effort in the exploitation of its improved spatial resolution.

ACKNOWLEDGEMENTS

We acknowledge the comments and suggestions by the anonymous referee that has helped to improve this manuscript.

We want to thank Prof. M. Blanton, who motivated us to improve the datacube reconstruction algorithm with a series of presentations and discussions on the topic.

S.F.S. thanks the PAPIIT-DGAPA AG100622 project. J.K.B.B. and S.F.S. acknowledge support from the CONACYT grant CF19-39578. R.G.B. acknowledges financial support from the grants CEX2021-001131-S funded by MCIN/AEI/10.13039/501100011033, SEV-2017-0709, and to PID2019-109067-GB100. L.G. acknowledges financial support from the Spanish Ministerio de Ciencia e Innovación (MCIN), the Agencia Estatal de Investigación (AEI) 10.13039/501100011033, and the European Social Fund (ESF) "Investing in your future" under the 2019 Ramón y Cajal program RYC2019-027683-I and the PID2020-115253GA-I00 HOSTFLOWS project, from Centro Superior de Investigaciones Científicas (CSIC) under the PIE project 20215AT016, and the program Unidad de Excelencia María de Maeztu CEX2020-001058-M.

This study uses data provided by the Calar Alto Legacy Integral Field Area (CALIFA) survey (<http://califa.caha.es/>). Based on observations collected at the Centro Astronómico Hispano Alemán (CAHA) at Calar Alto, operated jointly by the Max-Planck-Institut für Astronomie and the Instituto de Astrofísica de Andalucía (CSIC).

The Pan-STARRS1 Surveys (PS1) and the PS1 public science archive have been made possible through contributions by the Institute for Astronomy, the University of Hawaii, the Pan-STARRS Project Office, the Max-Planck Society and its participating institutes, the Max Planck Institute for Astronomy, Heidelberg and the Max Planck Institute for Extraterrestrial Physics, Garching, The Johns Hopkins University, Durham University, the University of Edinburgh, the Queen's University Belfast, the Harvard-Smithsonian Center for Astrophysics, the Las Cumbres Observatory Global Telescope Network Incorporated, the National Central University of Taiwan, the Space Telescope Science Institute, the National Aeronautics and Space Administration under Grant No. NNX08AR22G issued through the Planetary Science Division of the NASA Science Mission Directorate, the National Science Foundation Grant No. AST-1238877, the University of Maryland, Eotvos Lorand University (ELTE), the Los Alamos National Laboratory, and the Gordon and Betty Moore Foundation.

This research made use of Astropy,¹¹ a community-developed core Python package for Astronomy ([Astropy Collaboration et al. 2013, 2018](#)).

¹¹ <http://www.astropy.org>

DATA AVAILABILITY

The raw and reduced version of the data explored along this article are accessible through the Calar Alto Observatory Archive¹² and the eCALIFA DR webpage, accessible through the CALIFA webpage¹³. As part of this data release we distribute:

- The datacubes reduced using version 2.3 of the data reduction for all the originally compiled observations using the V500 setup: <http://ifs.astroscu.unam.mx/CALIFA/V500/v2.3/reduced/>
- The datacubes corresponding to the final sample of galaxies described in Sec. 3, once masked the possible companion objects and foreground field stars http://ifs.astroscu.unam.mx/CALIFA/V500/v2.3/reduced_masked/
- A fitsfile table including all the galaxy properties explored and discussed along this article, comprising the parameters included in Tables 2, 3, 4, 5 and 7: <http://ifs.astroscu.unam.mx/CALIFA/V500/v2.2/reduced/>
- The datacubes reduced using the previous version of the data reduction (ver. 2.2 [Sánchez et al. 2022b](#)), for the complete compiled observations: <http://ifs.astroscu.unam.mx/CALIFA/V500/v2.2/reduced/>

REFERENCES

- Abdurro'uf et al., 2021, arXiv e-prints, p. [arXiv:2112.02026](https://arxiv.org/abs/2112.02026)
- Albán M., Wylezalek D., 2023, arXiv e-prints, p. [arXiv:2302.08519](https://arxiv.org/abs/2302.08519)
- Alvarez-Hurtado P., Barrera-Ballesteros J. K., Sánchez S. F., Colombo D., López-Sánchez A. R., Aquino-Ortíz E., 2022, arXiv e-prints, p. [arXiv:2202.11651](https://arxiv.org/abs/2202.11651)
- Aquino-Ortíz E., et al., 2018, *MNRAS*, **479**, 2133
- Asari N. V., Cid Fernandes R., Stasińska G., Torres-Papaqui J. P., Mateus A., Sodré L., Schoenell W., Gomes J. M., 2007, *MNRAS*, **381**, 263
- Astropy Collaboration et al., 2013, *A&A*, **558**, A33
- Astropy Collaboration et al., 2018, *aj*, **156**, 123
- Bacon R., et al., 2010, in SPIE Conf. Series., doi:[10.1117/12.856027](https://doi.org/10.1117/12.856027)
- Baldwin J. A., Phillips M. M., Terlevich R., 1981, *PASP*, **93**, 5
- Barrera-Ballesteros J. K., Sánchez S. F., Heckman T., Blanc G. A., The MaNGA Team 2017, *ApJ*, **844**, 80
- Barrera-Ballesteros J. K., et al., 2020, *MNRAS*, **492**, 2651
- Barrera-Ballesteros J. K., et al., 2021a, arXiv e-prints, p. [arXiv:2101.02711](https://arxiv.org/abs/2101.02711)
- Barrera-Ballesteros J. K., et al., 2021b, arXiv e-prints, p. [arXiv:2101.04683](https://arxiv.org/abs/2101.04683)
- Barrera-Ballesteros J. K., et al., 2022, arXiv e-prints, p. [arXiv:2206.07058](https://arxiv.org/abs/2206.07058)
- Belfiore F., et al., 2017, *MNRAS*, **466**, 2570
- Belfiore F., et al., 2022, *A&A*, **659**, A26
- Bell E. F., de Jong R. S., 2000, *MNRAS*, **312**, 497
- Bell E. F., McIntosh D. H., Katz N., Weinberg M. D., 2003, *ApJS*, **149**, 289
- Bigiel F., Leroy A., Walter F., Brinks E., de Blok W. J. G., Madore B., Thornley M. D., 2008, *AJ*, **136**, 2846
- Binette L., Magris C. G., Stasińska G., Bruzual A. G., 1994, *A&A*, **292**, 13
- Bland-Hawthorn J., 1995, *Publ. Astron. Soc. Australia*, **12**, 190
- Blanton M. R., Moustakas J., 2009, *ARA&A*, **47**, 159
- Blanton M. R., et al., 2017, *AJ*, **154**, 28
- Bluck A. F. L., Maiolino R., Sanchez S., Ellison S. L., Thorp M. D., Piotrowska J. M., Teimoorinia H., Bundy K. A., 2019, arXiv e-prints, p. [arXiv:1911.08857](https://arxiv.org/abs/1911.08857)
- Bluck A. F. L., et al., 2020, *MNRAS*, **499**, 230
- Bolatto A. D., et al., 2017, *ApJ*, **846**, 159

¹² <http://www.caha.es/science-mainmenu-95/public-archives>

¹³ official: <http://califa.caha.es/>, mirror:http://ifs.astroscu.unam.mx/CALIFA_WEB/public_html/

- Bresolin F., 2017, in Knapen J. H., Lee J. C., Gil de Paz A., eds, *As-trophysics and Space Science Library Vol. 434, Outskirts of Galaxies*. p. 145 ([arXiv:1612.05278](https://arxiv.org/abs/1612.05278)), doi:10.1007/978-3-319-56570-5_5
- Brinchmann J., Charlot S., White S. D. M., Tremonti C., Kauffmann G., Heckman T., Brinchmann J., 2004, *MNRAS*, **351**, 1151
- Brinchmann J., Charlot S., Kauffmann G., Heckman T., White S. D. M., Tremonti C., 2013, *MNRAS*, **432**, 2112
- Bruzual G., Charlot S., 2003, *Mon. Not. R. Astron. Soc.*, **344**, 1000
- Bundy K., et al., 2015, *ApJ*, **798**, 7
- Calette A. R., Avila-Reese V., Rodríguez-Puebla A., Hernández-Toledo H., Papastergis E., 2018, *Rev. Mex. Astron. Astrofis.*, **54**, 443
- Calzetti D., 2001, *PASP*, **113**, 1449
- Calzetti D., Meurer G. R., Bohlin R. C., Garnett D. R., Kinney A. L., Leitherer C., Storch-Bergmann T., 1997, *AJ*, **114**, 1834
- Camps-Fariña A., Sanchez S. F., Lacerda E. A. D., Carigi L., García-Benito R., Mast D., Galbany L., 2021, *MNRAS*, **504**, 3478
- Camps-Fariña A., et al., 2022, arXiv e-prints, p. [arXiv:2203.01159](https://arxiv.org/abs/2203.01159)
- Cano-Díaz M., et al., 2016, *ApJ*, **821**, L26
- Cano-Díaz M., Ávila-Reese V., Sánchez S. F., Hernández-Toledo H. M., Rodríguez-Puebla A., Boquien M., Ibarra-Medel H., 2019, *MNRAS*, **488**, 3929
- Cappellari M., 2016, *ARA&A*, **54**, 597
- Cappellari M., Copin Y., 2003, *MNRAS*, **342**, 345
- Cardelli J. A., Clayton G. C., Mathis J. S., 1989a, *ApJ*, **345**, 245
- Cardelli J. A., Clayton G. C., Mathis J. S., 1989b, *ApJ*, **345**, 245
- Carigi L., Peimbert M., Peimbert A., 2019, *ApJ*, **873**, 107
- Catalán-Torrecilla C., et al., 2017, *ApJ*, **848**, 87
- Chambers K. C., et al., 2016, arXiv e-prints, p. [arXiv:1612.05560](https://arxiv.org/abs/1612.05560)
- Chung H., Park C., Park Y.-S., 2021, *ApJS*, **257**, 66
- Cid Fernandes R., Stasińska G., Schlickmann M. S., Mateus A., Vale Asari N., Schoenell W., Sodré L., 2010, *MNRAS*, **403**, 1036
- Cid Fernandes R., et al., 2014, *A&A*, **561**, A130
- Colombo D., et al., 2020, arXiv e-prints, p. [arXiv:2009.08383](https://arxiv.org/abs/2009.08383)
- Corcho-Caballero P., Ascasisbar Y., Sánchez S. F., López-Sánchez Á. R., 2023, *MNRAS*, **520**, 193
- Cortese L., et al., 2014, *ApJ*, **795**, L37
- Courteau S., et al., 2014, *Reviews of Modern Physics*, **86**, 47
- Cresci G., Mannucci F., Curti M., 2019, *A&A*, **627**, A42
- Croom S. M., et al., 2012, *MNRAS*, **421**, 872
- D'Agostino J. J., et al., 2019, *MNRAS*, **487**, 4153
- Davies R. L., et al., 2016, *MNRAS*, **462**, 1616
- Dopita M. A., Koratkar A. P., Evans I. N., Allen M., Bicknell G. V., Sutherland R. S., Hawley J. F., Sadler E., 1996, in Eracleous M., Koratkar A., Leitherer C., Ho L., eds, *Astronomical Society of the Pacific Conference Series Vol. 103, The Physics of Liners in View of Recent Observations*. p. 44
- Driver S. P., et al., 2009, *Astronomy and Geophysics*, **50**, 5.12
- Ellison S. L., Sánchez S. F., Ibarra-Medel H., Antonio B., Mendel J. T., Barrera-Ballesteros J., 2018, *MNRAS*, **474**, 2039
- Ellison S. L., Lin L., Thorp M. D., Pan H.-A., Sánchez S. F., Bluck A. F. L., Belfiore F., 2020a, *MNRAS*,
- Ellison S. L., et al., 2020b, *MNRAS*, **493**, L39
- Emsellem E., et al., 2022, *A&A*, **659**, A191
- Espinosa-Ponce C., Sánchez S. F., Morisset C., Barrera-Ballesteros J. K., Galbany L., García-Benito R., Lacerda E. A. D., Mast D., 2020, *MNRAS*, **494**, 1622
- Espinosa-Ponce C., Sánchez S. F., Morisset C., Barrera-Ballesteros J. K., Galbany L., García-Benito R., Lacerda E. A. D., Mast D., 2022, *MNRAS*,
- Faber S., 1977, in Larson B. M. T., R. B., ed., *The Evolution of Galaxies and Stellar Populations*. p. 157
- Faber S. M., Jackson R. E., 1976, *ApJ*, **204**, 668
- Flewelling H. A., et al., 2020, *ApJS*, **251**, 7
- Flores-Fajardo N., Morisset C., Stasińska G., Binette L., 2011, *MNRAS*, **415**, 2182
- Fruchter A. S., Hook R. N., 2002, *PASP*, **114**, 144
- Fukugita M., et al., 2007, *AJ*, **134**, 579
- Gaia Collaboration et al., 2016, *A&A*, **595**, A1
- Gaia Collaboration et al., 2021, *A&A*, **649**, A1
- Galbany L., et al., 2018, *ApJ*, **855**, 107
- Gallazzi A., Bell E. F., 2009, *ApJS*, **185**, 253
- Gallazzi A., Charlot S., Brinchmann J., White S. D. M., Tremonti C. A., 2005, *MNRAS*, **362**, 41
- Gallazzi A., Charlot S., Brinchmann J., White S. D. M., 2006, *MNRAS*, **370**, 1106
- García-Benito R., et al., 2015, *A&A*, **576**, A135
- García-Benito R., et al., 2017, *A&A*, **608**, A27
- García-Benito R., González Delgado R. M., Pérez E., Cid Fernandes R., Sánchez S. F., de Amorim A. L., 2019, *A&A*, **621**, A120
- George K., et al., 2019, *MNRAS*, **487**, 3102
- Goddard D., et al., 2017, *MNRAS*, **466**, 4731
- Gomes J. M., et al., 2016, *A&A*, **588**, A68
- González Delgado R. M., Pérez E., Cid Fernandes R., et al. 2014a, *A&A*, **562**, A47
- González Delgado R. M., et al., 2014b, *ApJ*, **791**, L16
- González Delgado R. M., et al., 2015, *A&A*, **581**, A103
- González Delgado R. M., et al., 2016, *A&A*, **590**, A44
- Grandmont F., Drissen L., Mandar J., Thibault S., Baril M., 2012, in McLean I. S., Ramsay S. K., Takami H., eds, *Society of Photo-Optical Instrumentation Engineers (SPIE) Conference Series Vol. 8446, Ground-based and Airborne Instrumentation for Astronomy IV*. p. 84460U, doi:10.1117/12.926782
- Green A. W., et al., 2018, *MNRAS*, **475**, 716
- Gunn J. E., et al., 1998, *AJ*, **116**, 3040
- Heckman T. M., Armus L., Miley G. K., 1990, *ApJS*, **74**, 833
- Ho L. C., Filippenko A. V., Sargent W. L. W., 1997, *ApJ*, **487**, 568
- Husemann B., et al., 2013, *A&A*, **549**, A87
- Ibarra-Medel H. J., et al., 2016, *MNRAS*, **463**, 2799
- Ibarra-Medel H. J., Avila-Reese V., Sánchez S. F., González-Samaniego A., Rodríguez-Puebla A., 2019, *MNRAS*, **483**, 4525
- Into T., Portinari L., 2013, *MNRAS*, **430**, 2715
- Kalinova V., et al., 2022, *A&A*, **665**, A90
- Kauffmann G., et al., 2003a, *MNRAS*, **341**, 33
- Kauffmann G., et al., 2003b, *MNRAS*, **346**, 1055
- Kelz A., et al., 2006, *PASP*, **118**, 129
- Kennicutt Jr. R. C., 1998, *ApJ*, **498**, 541
- Kennicutt Jr. R. C., Keel W. C., Blaha C. A., 1989, *AJ*, **97**, 1022
- Kewley L. J., Dopita M. A., Sutherland R. S., Heisler C. A., Trevena J., 2001, *ApJ*, **556**, 121
- Kewley L. J., Nicholls D. C., Sutherland R. S., 2019, *Annual Review of Astronomy and Astrophysics*, **57**, 511
- Kobayashi C., Karakas A. I., Lugaro M., 2020, *ApJ*, **900**, 179
- Lacerda E. A. D., et al., 2018, *MNRAS*, **474**, 3727
- Lacerda E. A. D., Sánchez S. F., Cid Fernandes R., López-Cobá C., Espinosa-Ponce C., Galbany L., 2020, *MNRAS*, **492**, 3073
- Lacerda E. A. D., Sánchez S. F., Mejía-Narváez A., Camps-Fariña A., Espinosa-Ponce C., Barrera-Ballesteros J. K., Ibarra-Medel H., Lugo-Aranda A. Z., 2022, arXiv e-prints, p. [arXiv:2202.08027](https://arxiv.org/abs/2202.08027)
- Larson R. B., 1976, *MNRAS*, **176**, 31
- Law D. R., et al., 2015, *AJ*, **150**, 19
- Law D. R., et al., 2021, arXiv e-prints, p. [arXiv:2112.11281](https://arxiv.org/abs/2112.11281)
- Leroy A. K., et al., 2013, *AJ*, **146**, 19
- Lin L., et al., 2019, arXiv e-prints, p. [arXiv:1909.11243](https://arxiv.org/abs/1909.11243)
- Lin L., et al., 2020, arXiv e-prints, p. [arXiv:2010.01751](https://arxiv.org/abs/2010.01751)
- Liu D., Blanton M. R., Law D. R., 2020, *AJ*, **159**, 22
- López-Cobá C., et al., 2020, arXiv e-prints, p. [arXiv:2002.09328](https://arxiv.org/abs/2002.09328)
- López-Sánchez Á. R., Dopita M. A., Kewley L. J., Zahid H. J., Nicholls D. C., Scharwächter J., 2012, *MNRAS*, **426**, 2630
- Maiolino R., Mannucci F., 2019, *A&ARv*, **27**, 3
- Marino R. A., et al., 2013, *A&A*, **559**, A114
- Mármol-Queralto E., et al., 2011, *A&A*, **534**, A8
- Mast D., et al., 2014, *A&A*, **561**, A129
- Matteucci F., 1992, *Mem. Soc. Astron. Italiana*, **63**, 301
- Mejía-Narváez A., Sánchez S. F., Lacerda E. A. D., Carigi L., Galbany L., Husemann B., García-Benito R., 2020, *MNRAS*, **499**, 4838

- Méndez-Abreu J., Sánchez S. F., de Lorenzo-Cáceres A., 2019, *MNRAS*, **488**, L80
- Osterbrock D. E., 1989, *Astrophysics of gaseous nebulae and active galactic nuclei*. University Science Books
- Ostriker E. C., McKee C. F., Leroy A. K., 2010, *ApJ*, **721**, 975
- Pan H.-A., et al., 2018, *ApJ*, **854**, 159
- Pan H.-A., et al., 2022, *ApJ*, **927**, 9
- Panther B., Heavens A. F., Jimenez R., 2003, *MNRAS*, **343**, 1145
- Peebles P. J. E., 1969, *ApJ*, **155**, 393
- Peimbert M., Peimbert A., 2006, in *Revista Mexicana de Astronomía y Astrofísica Conference Series*. p. 163
- Peletier R. F., Davies R. L., Illingworth G. D., Davis L. E., Cawson M., 1990, *AJ*, **100**, 1091
- Pérez-González P. G., Trujillo I., Barro G., Gallego J., Zamorano J., Conselice C. J., 2008, *ApJ*, **687**, 50
- Pérez E., et al., 2013, *ApJ*, **764**, L1
- Pessa I., et al., 2022, *A&A*, **663**, A1
- Pilyugin L. S., Thuan T. X., Vílchez J. M., 2007, *MNRAS*, **376**, 353
- Poggianti B. M., et al., 2017, *ApJ*, **844**, 48
- Renzini A., Peng Y.-j., 2015, *ApJ*, **801**, L29
- Richardson W. H., 1972, *J. Opt. Soc. Am.*, **62**, 55
- Rodríguez-Puebla A., Primack J. R., Behroozi P., Faber S. M., 2016, *MNRAS*, **455**, 2592
- Roediger J. C., Courteau S., 2015, *MNRAS*, **452**, 3209
- Rosales-Ortega F. F., Díaz A. I., Kennicutt R. C., Sánchez S. F., 2011, *MNRAS*, **415**, 2439
- Rosales-Ortega F. F., Sánchez S. F., Iglesias-Páramo J., Díaz A. I., Vílchez J. M., Bland-Hawthorn J., Husemann B., Mast D., 2012, *ApJ*, **756**, L31
- Roth M. M., et al., 2005, *PASP*, **117**, 620
- Rousseau-Nepton L., Robert C., Martin R. P., Drissen L., Martin T., 2018, *MNRAS*, **477**
- Saintonge A., et al., 2016, *MNRAS*, **462**, 1749
- Salim S., Narayanan D., 2020, *ARA&A*, **58**, 529
- Salpeter E. E., 1955, *ApJ*, **121**, 161
- Sánchez S. F., 2006, *Astronomische Nachrichten*, **327**, 850
- Sánchez S. F., 2020, *ARA&A*, **58**, 99
- Sánchez Almeida J., Elmegreen B. G., Muñoz-Tuñón C., Elmegreen D. M., 2014, *A&ARv*, **22**, 71
- Sánchez S. F., Aceituno J., Thiele U., Pérez-Ramírez D., Alves J., 2007, *PASP*, **119**, 1186
- Sánchez S. F., Thiele U., Aceituno J., Cristobal D., Perea J., Alves J., 2008, *PASP*, **120**, 1244
- Sánchez S. F., et al., 2012, *A&A*, **538**, A8
- Sánchez S. F., et al., 2014, *A&A*, **563**, A49
- Sánchez S. F., et al., 2016a, *Rev. Mex. Astron. Astrofis.*, **52**, 21
- Sánchez S. F., et al., 2016b, *A&A*, **594**, A36
- Sánchez S. F., et al., 2017, *MNRAS*, **469**, 2121
- Sánchez S. F., et al., 2018, *Rev. Mex. Astron. Astrofis.*, **54**, 217
- Sánchez S. F., et al., 2019a, *MNRAS*, **482**, 1557
- Sánchez S. F., et al., 2019b, *MNRAS*, **484**, 3042
- Sánchez S. F., Walcher C. J., Lopez-Cobá C., Barrera-Ballesteros J. K., Mejía-Narváez A., Espinosa-Ponce C., Camps-Fariña A., 2021a, *Rev. Mex. Astron. Astrofis.*, **57**, 3
- Sánchez S. F., et al., 2021b, *MNRAS*, **503**, 1615
- Sánchez S. F., Gómez Medina D. C., Barrera-Ballesteros J. K., Galbany L., Bolatto A., Wong T., 2022a, *arXiv e-prints*, p. [arXiv:2212.03738](https://arxiv.org/abs/2212.03738)
- Sánchez S. F., et al., 2022b, *ApJS*, **262**, 36
- Santini P., et al., 2014, *A&A*, **562**, A30
- Sarmiento R., Huertas-Company M., Knapen J. H., Ibarra-Medel H., Pillepich A., Sánchez S. F., Boecker A., 2022, *arXiv e-prints*, p. [arXiv:2211.11790](https://arxiv.org/abs/2211.11790)
- Schmidt M., 1968, *ApJ*, **151**, 393
- Shannon C. E., 1948, *The Bell System Technical Journal*, **27**, 379
- Sharp R., et al., 2015, *MNRAS*, **446**, 1551
- Shepard D., 1968, *Proceedings of the 1968 ACM National Conference*, **1**, 517
- Singh R., et al., 2013, *A&A*, **558**, A43
- Speagle J. S., Steinhardt C. L., Capak P. L., Silverman J. D., 2014, *ApJS*, **214**, 15
- Springel V., et al., 2018, *MNRAS*, **475**, 676
- Stasińska G., et al., 2008, *MNRAS*, **391**, L29
- Stubbs C. W., Doherty P., Cramer C., Narayan G., Brown Y. J., Lykke K. R., Woodward J. T., Tonry J. L., 2010, *ApJS*, **191**, 376
- Sun J., et al., 2020, *ApJ*, **901**, L8
- Taylor E. N., et al., 2011, *MNRAS*, **418**, 1587
- Tremonti C. A., et al., 2004, *ApJ*, **613**, 898
- Tully R. B., Fisher J. R., 1977, *A&A*, **54**, 661
- Ueta T., Otsuka M., 2021, *PASP*, **133**, 093002
- Vale Asari N., Couto G. S., Cid Fernandes R., Stasińska G., de Amorim A. L., Ruschel-Dutra D., Werle A., Florido T. Z., 2019, *MNRAS*, **489**, 4721
- Vila-Costas M. B., Edmunds M. G., 1992, *MNRAS*, **259**, 121
- Vulcani B., et al., 2019, *MNRAS*, **488**, 1597
- Walcher C. J., et al., 2014, *A&A*, **569**, A1
- Walcher C. J., Coelho P. R. T., Gallazzi A., Bruzual G., Charlot S., Chiappini C., 2015, *A&A*, **582**, A46
- Weiner B. J., et al., 2006, *ApJ*, **653**, 1049
- Wild V., Charlot S., Brinchmann J., Heckman T., Vince O., Pacifici C., Chevallard J., 2011, *MNRAS*, **417**, 1760
- Wong T., Blitz L., 2002, *ApJ*, **569**, 157
- Woosley S. E., Weaver T. A., 1995, *ApJS*, **101**, 181
- Yan R., et al., 2016, *AJ*, **151**, 8
- Yan R., et al., 2019, *ApJ*, **883**, 175
- Yates R. M., Henriques B., Thomas P. A., Kauffmann G., Johansson J., White S. D. M., 2013, *MNRAS*, **435**, 3500
- York D. G., et al., 2000a, *AJ*, **120**, 1579
- York D. G., Adelman J., Anderson Jr. J. E., Anderson S. F., et al. 2000b, *AJ*, **120**, 1579
- Zhu G. B., Barrera-Ballesteros J. K., Heckman T. M., Zakamska N. L., Sánchez S. F., Yan R., Brinkmann J., 2017, *MNRAS*, **468**, 4494
- Zhu L., et al., 2018, *Nature Astronomy*, **2**, 233
- Zibetti S., Charlot S., Rix H., 2009, *MNRAS*, **400**, 1181
- de Jong R. S., van der Kruit P. C., 1994, *A&AS*, **106**, 451